

UNIVERSITY OF KENT

STAR FORMATION

**The Evolutionary Tracks for Low to
High Mass Star Formation through
Variable Accretion Models**

Author:

DAVID HASTIE

Supervisor:

Professor M. D. SMITH

Thesis for Masters of Science

in the

Centre of Astrophysics and Planetary Science
School of Physical Sciences

UNIVERSITY OF KENT

Abstract

Centre of Astrophysics and Planetary Science

School of Physical Sciences

Masters of Science

The Evolutionary Tracks for Low to High Mass Star Formation through Variable Accretion Models

by DAVID HASTIE

Embedded star formation is largely obscured from even the most modern of telescopes therefore computational modelling is used to provide some of the essential information required to fully understand the intrinsic star forming processes. In this thesis, evolutionary models are calculated for protostars and their environments using the hydrodynamic code STELLAR to describe the growing star itself. The code is modified with constant and variable accretion models with the inclusion of episodic bursts to produce stars of final masses of $1 - 100M_{\odot}$. Luminosity, radius, temperature and mass parameters are tracked throughout the stellar evolution to find potential signature features of each accretion model.

Indications as to why all accretion methods are supported by observation are found and methods of distinguishing between them are suggested. Recent ATLASGAL observations are used to investigate the appropriate methods of statistical comparison between observational and theoretical data. Progress is made toward successful comparisons of theoretical and observational data, with suggestions for clump L/M distribution data analysed using an initial mass function holding the greatest potential for direct comparisons between the two.

Acknowledgements

I am exceptionally grateful to Prof. Michael Smith, for providing excellent support, guidance and insight throughout this project.

I'd also like to thank the University of Kent for providing research facilities and materials required.

Thank you to H. Yorke for providing the modified STELLAR code and R. Kuiper for giving advice of its application.

A much needed thank you to my family and friends for support and encouragement.

Lastly I'd like to thank Charlotte, without whom this project would have been finished much sooner.

Contents

Title Page	i
Abstract	iii
Acknowledgements	v
1 Introduction	1
1.1 Star formation history	3
2 Method Theory	11
2.1 Jeans Criterion	11
2.1.1 Fragmentation	13
2.2 Stellar Equilibrium	15
2.3 Mass Conservation	17
2.4 Upper Mass Limit	17
2.5 Pressure	19
2.5.1 Pressure Integral	20
2.5.2 Ideal Gas Pressure	22
2.5.3 Radiation Pressure	24
2.5.4 Degeneracy Pressure	25
2.6 Equilibrium	28
2.7 Luminosity	29
2.8 Energy Transport Mechanisms	30
2.9 Stellar Equations	32
2.10 Boundary Conditions	32
2.11 The Model	34
2.12 Pre Main Sequence Phases	36
2.12.1 Adiabatic Accretion	37
2.12.2 Swelling	37
2.12.3 Kelvin-Helmholtz Contraction	38

2.12.4 Main Sequence Transition	38
3 Method	41
3.1 Accretion	41
3.1.1 Constant	43
3.1.2 Accelerated	43
3.1.3 Exponential	44
3.1.4 Power Law	45
3.1.5 Accretion Bursts	45
3.1.6 Input File	46
3.2 Evolutionary Tracks	52
3.2.1 Mass Radius	52
3.2.2 Theoretical Hertzsprung Russell Track	52
3.2.3 Mass Luminosity	52
4 Results	55
4.0.1 Notes	56
4.1 Mass Radius	56
4.2 Theoretical Hertzsprung Russell	63
4.2.1 Constant Accretion	63
4.2.2 Accelerated Accretion	65
4.2.3 Exponential Accretion	67
4.2.4 Power Law Accretion	69
4.3 Mass Luminosity	71
4.3.1 Constant Accretion	72
4.3.2 Accelerated Accretion	73
4.3.3 Exponential Accretion	74
4.3.4 Power Law Accretion	75
4.3.5 Clump Luminosity Clump Mass Distribution	75
4.3.6 Smooth Accretion results	76
Constant Accretion	77
Accelerated Accretion	81
Exponential Accretion	85
Power Law Accretion	89
4.4 Episodic Accretion Bursts	93

4.4.1	Mass radius	94
	Constant Accretion	95
	Accelerated Model	96
	Exponential Model	97
	Power Law Model	98
4.4.2	Episodal theoretical H-R	99
4.4.3	Constant Accretion	99
4.4.4	Accelerated Accretion	100
4.4.5	Exponential Accretion	101
4.4.6	Power Law Accretion	102
4.4.7	Mass luminosity	104
	Constant Accretion	104
	Accelerated Accretion	105
	Exponential Accretion	106
4.4.8	PowerLaw Accretion	107
4.4.9	Luminosity-to-Mass Ratio Distribution	107
	Constant	108
	Accelerated	111
	Exponential	114
	Power Law	117
5	Discussion	121
5.1	Hydrodynamic code	122
5.2	General	123
5.3	The Mass Radius tracks	124
5.4	Hertzsprung Russell Tracks	126
5.5	Clump Luminosity Mass Relation	128
5.5.1	Smooth - Burst Comparison	135
5.5.2	Clusters, Multiplicity and SFE	135
5.5.3	IMF Adjusted Clump Luminosity	136
5.6	Episodic Bursts	138
5.7	Early Accretion Cut Off	139
5.8	Molecular cloud influence	140
5.9	Other comparative works	141

6 Conclusion	143
6.1 Summary of Findings	143
6.2 Future work	144
6.3 End	146
A Appendix	147

List of Figures

1.1	The modern understanding of the convective and radiative structures contained within stars. The low mass stars are fully convective which would comply with Emden's work. The greater masses have more complex systems involving both convective and radiative sectors. (Sun.org, 2016)	5
1.2	A collection of images of the Crab Nebula (NGC 1952) highlighting differences found in the different wavebands. The left column, from top to bottom, contains radio, visible and x-ray wavelengths. The right column, from top to bottom, contains infrared, ultraviolet and gamma ray wavelengths. Infrared spectra shows the cooler star forming regions whilst ultra violet show intense heat of Main Sequence stars. Note the radio image is a combination of two different radio wavebands combined.	
	Credit to; NRAO (2016b), NRAO (2016a), NASA/JPL-Caltech/R. Gehrz (University of Minnesota) (2016), NASA, ESA, J. Hester and A. Loll (Arizona State University) (2016), NASA/Swift/E. Hoversten, PSU (2016), NASA/CXC/SAO/F.Seward et al (2016), NASA/DOE/Fermi LAT/R. Buehler (2016)	8
1.3	A false colour image of β Pictoris in the infrared band. The bright regions on opposite sides of the centroid show the remnants of an accretion disk around a young star. It is likely that the remaining disk will go on to form planets. Credit to Jean-Luc Beuzit, et al. Grenoble Observatory, European Southern Observatory (2016)	9

2.1	A heat map view of gas densities across the x-z plane of a 3D simulation (Kuiper et al., 2011). The image comes from the model at 10kyr and $120M_{\odot}$ protostellar core. The protostellar region of high density can be seen at centered at the bottom of the figure.	19
2.2	A diagram showing the scenario of a 'first principles' gas in a cylinder.	21
2.3	The grid setup of the STELLAR as shown in Bodenheimer et al. (2006), the variables of density, nuclear energy, opacity and, total energy ($\rho, E_{nuc}, \kappa, \epsilon$ respectively) are all found as functions of the variables shown at the top of the grid. M_r is the lagrangian co-ordinate, with pressure, radius, temperature and, luminosity being the four dependent variables (P, r, T, L , respectively).	35
2.4	The evolutionary track for radius as a function of stellar mass, as found by the code used in Smith (2014). The figure shows an extreme example of the pre main sequence phases using a star with a final mass of $300M_{\odot}$. Labels on the figure, 1, 2, 3 and, 4 indicate the adiabatic accretion, swelling, KH contraction and main sequence transition phases, respectively. . . .	37
3.1	The four different modelled accretion rates plotted as a function time for a star of $10M_{\odot}$	42
4.1	The radius tracks for protostars of final mass, $100M_{\odot}$. All four accretion methods are coloured accordingly as found in the legend.	58
4.2	The radius tracks for protostars of final mass, $50M_{\odot}$. All four accretion methods are coloured accordingly as found in the legend.	59
4.3	The radius tracks for protostars of final mass, $25M_{\odot}$	59
4.4	The radius tracks for protostars of final mass, $10M_{\odot}$	60
4.5	The radius tracks for protostars of final mass, $8M_{\odot}$	60
4.6	The radius tracks for protostars of final mass, $6M_{\odot}$	61
4.7	The radius tracks for protostars of final mass, $5M_{\odot}$	61

4.8	The radius tracks for protostars of final mass, $1M_{\odot}$	62
4.9	The H-R track for a star of $100M_{\odot}$ final mass using the cold constant accretion method. The dashed line represents the total luminosity and the solid coloured line represents the core luminosity.	63
4.10	The H-R track for a star of $10M_{\odot}$ final mass using the cold constant accretion method. The dashed line represents the total luminosity and the solid coloured line represents the core luminosity.	64
4.11	The H-R track for a star of $1M_{\odot}$ final mass using the cold constant accretion method. The dashed line represents the total luminosity and the solid coloured line represents the core luminosity.	64
4.12	The H-R track for a star of $100M_{\odot}$ final mass using the cold accelerated accretion method. The dashed line represents the total luminosity and the solid coloured line represents the core luminosity.	65
4.13	The H-R track for a star of $10M_{\odot}$ final mass using the cold accelerated accretion method. The dashed line represents the total luminosity and the solid coloured line represents the core luminosity.	66
4.14	The H-R track for a star of $1M_{\odot}$ final mass using the cold accelerated accretion method. The dashed line represents the total luminosity and the solid coloured line represents the core luminosity.	66
4.15	The H-R track for a star of $100M_{\odot}$ final mass using the cold exponential accretion method. The dashed line represents the total luminosity and the solid coloured line represents the core luminosity.	67
4.16	The H-R track for a star of $10M_{\odot}$ final mass using the cold exponential accretion method. The dashed line represents the total luminosity and the solid coloured line represents the core luminosity.	68

4.17 The H-R track for a star of $1M_{\odot}$ final mass using the cold exponential accretion method. The dashed line represents the total luminosity and the solid coloured line represents the core luminosity.	68
4.18 The H-R track for a star of $100M_{\odot}$ final mass using the cold power law accretion method. The dashed line represents the total luminosity and the solid coloured line represents the core luminosity.	69
4.19 The H-R track for a star of $10M_{\odot}$ final mass using the cold power law accretion method. The dashed line represents the total luminosity and the solid coloured line represents the core luminosity.	70
4.20 The H-R track for a star of $1M_{\odot}$ final mass using the cold power law accretion method. The dashed line represents the total luminosity and the solid coloured line represents the core luminosity.	70
4.21 The Mass Luminosity tracks using the cold constant accretion method. The final masses of the stars associated with tracks from left to right, $1M_{\odot}, 5M_{\odot}, 10M_{\odot}, 25M_{\odot}, 100M_{\odot}$. .	72
4.22 The Mass Luminosity tracks using the cold accelerated accretion method. The final masses of the stars associated with tracks from left to right, $1M_{\odot}, 5M_{\odot}, 10M_{\odot}, 25M_{\odot}, 100M_{\odot}$.	73
4.23 The Mass Luminosity tracks using the cold exponential accretion method. The final masses of the stars associated with tracks from left to right, $1M_{\odot}, 5M_{\odot}, 10M_{\odot}, 25M_{\odot}, 100M_{\odot}$.	74
4.24 The tracks for clump luminosity as a function of clump mass using the cold power law accretion method. The final masses of the stars associated with tracks from left to right, $1M_{\odot}, 5M_{\odot}, 10M_{\odot}, 25M_{\odot}, 100M_{\odot}$	75
4.25 Constant Distribution Results	77

4.25 The ATLASGAL distributions for MMB YSO and HII object types for the left, central and right column respectively. The dashed lines on plots A,B,C,D,E,F,G,H,I,J,K represent star of final masses 1, 2, 4, 5, 6, 8, 10, 15, 20, 25 and, $100M_{\odot}$ respectively, using the constant accretion method.	80
4.26 Accelerated Distribution Results	81
4.26 The ATLASGAL distributions for MMB YSO and HII object types for the left, central and right column respectively. The dashed lines on plots A,B,C,D,E,F,G,H,I,J,K represent star of final masses 1, 2, 4, 5, 6, 8, 10, 15, 20, 25 and, $100M_{\odot}$ respectively, through the accelerated accretion.	84
4.27 Exponential Distribution Results	85
4.27 The ATLASGAL distributions for MMB YSO and HII object types for the left, central and right column respectively. The dashed lines on plots A,B,C,D,E,F,G,H,I,J,K represent star of final masses 1, 2, 4, 5, 6, 8, 10, 15, 20, 25 and, $100M_{\odot}$ respectively, through the exponential accretion method.	88
4.28 Power Law Distribution Results	89
4.28 The ATLASGAL distributions for MMB YSO and HII object types for the left, central and right column respectively. The dashed lines on plots A,B,C,D,E,F,G,H,I,J,K represent star of final masses 1, 2, 4, 5, 6, 8, 10, 15, 20, 25 and, $100M_{\odot}$ respectively, through the power law accretion method.	92
4.29 The accelerated accretion rate over time for both the smooth and burst accretion models. The final mass achieved is shown in the lower graph.	93
4.30 The radius as function of mass tracks for cold constant accretion with episodic bursts. The tracks stars of final masses $1M_{\odot}$, $5M_{\odot}$, $10M_{\odot}$ and, $20M_{\odot}$ respectively.	95
4.31 The radius as function of mass tracks for cold constant accretion with episodic bursts. The tracks of final masses $2M_{\odot}$, $4M_{\odot}$, $6M_{\odot}$ and, $8M_{\odot}$ respectively.	95

4.32 The radius as function of mass tracks for cold accelerated accretion with episodic bursts. The tracks represent stars of final masses $15M_{\odot}$, $10M_{\odot}$, $5M_{\odot}$ and, $1M_{\odot}$ respectively.	96
4.33 The radius as function of mass tracks for cold accelerated accretion with episodic bursts. The tracks represent stars of final masses $8M_{\odot}$, $6M_{\odot}$, $4M_{\odot}$ and, $2M_{\odot}$ respectively.	96
4.34 The radius as function of mass tracks for cold exponential accretion with episodic bursts. The tracks represent stars of final masses $20M_{\odot}$, $10M_{\odot}$, $5M_{\odot}$ and, $1M_{\odot}$ respectively.	97
4.35 The radius as function of mass tracks for cold exponential accretion with episodic bursts. The tracks represent stars of final masses $8M_{\odot}$, $6M_{\odot}$, $4M_{\odot}$ and, $2M_{\odot}$ respectively.	97
4.36 The radius as function of mass tracks for cold exponential accretion with episodic bursts. The tracks represent stars of final masses $20M_{\odot}$, $10M_{\odot}$, $5M_{\odot}$ and, $1M_{\odot}$ respectively.	98
4.37 The radius as function of mass tracks for cold exponential accretion with episodic bursts. The tracks represent stars of final masses $8M_{\odot}$, $6M_{\odot}$, $4M_{\odot}$ and, $2M_{\odot}$ respectively.	98
4.38 The H-R track for a star of $10M_{\odot}$ final mass using the cold constant accretion method with bursts. The dashed line represents the total luminosity and the solid coloured line represents the core luminosity.	99
4.39 The H-R track for a star of $1M_{\odot}$ final mass using the cold constant accretion method including bursts. The dashed line represents the total luminosity and the solid coloured line represents the core luminosity.	100
4.40 The H-R track for a star of $10M_{\odot}$ final mass using the cold accelerated accretion method including bursts. The dashed line represents the total luminosity and the solid coloured line represents the core luminosity.	100
4.41 The H-R track for a star of $1M_{\odot}$ final mass using the cold accelerated accretion method including bursts. The dashed line represents the total luminosity and the solid coloured line represents the core luminosity.	101

4.42 The H-R track for a star of $10M_{\odot}$ final mass using the cold exponential accretion method.	101
4.43 The H-R track for a star of $1M_{\odot}$ final mass using the cold exponential accretion method including bursts. The dashed line represents the total luminosity and the solid coloured line represents the core luminosity.	102
4.44 The H-R track for a star of $10M_{\odot}$ final mass using the cold power law accretion method including bursts. The dashed line represents the total luminosity and the solid coloured line represents the core luminosity.	102
4.45 The H-R track for a star of $1M_{\odot}$ final mass using the cold power law accretion method.	103
4.46 The Mass Luminosity tracks using the cold constant accretion method. The final masses of the stars associated with tracks from left to right, $1M_{\odot}, 5M_{\odot}, 10M_{\odot}, 20M_{\odot}$	104
4.47 The Mass Luminosity tracks using the cold accelerated accretion method. The final masses of the stars associated with tracks from left to right, $1M_{\odot}, 5M_{\odot}, 10M_{\odot}, \S$	105
4.48 The Mass Luminosity tracks using the cold exponential accretion method. The final masses of the stars associated with tracks from left to right, $1M_{\odot}, 5M_{\odot}, 10M_{\odot}, 20M_{\odot}$	106
4.49 The tracks for clump luminosity as a function of clump mass using the cold power law accretion method. The final masses of the stars associated with tracks from left to right, $1M_{\odot}, 5M_{\odot}, 10M_{\odot}, 20M_{\odot}$	107
4.50 All Constant Burst Distribution Results	108
4.50 The ATLASGAL distributions for MMB YSO and HII object types for the left, central and right column respectively. The dashed lines on plots A,B,C,D,E,F,G,H,I represent star of final masses 1, 2, 4, 5, 6, 8, 10, 15 and, $20M_{\odot}$ respectively, using the constant accretion method including episodic bursts.	110
4.51 All Accelerated Burst Distribution Results	111

4.51 The ATLASGAL distributions for MMB YSO and HII object types for the left, central and right column respectively. The dashed lines on plots A,B,C,D,E,F,G,H represent star of final masses 1,2,4,5,6,8,10 and $15M_{\odot}$ respectively, using the accelerated accretion method including episodic bursts.	113
4.52 All Exponential Burst Distribution Results	114
4.52 The ATLASGAL distributions for MMB YSO and HII object types for the left, central and right column respectively. The dashed lines on plots A,B,C,D,E,F,G,H,I represent star of final masses 1, 2, 4, 5, 6, 8, 10, 15 and, $20M_{\odot}$ respectively, using the exponential accretion method including episodic bursts.	116
4.53 All Power law distribution results	117
4.53 The ATLASGAL distributions for MMB YSO and HII object types for the left, central and right column respectively. The dashed lines on plots A,B,C,D,E,F,G,H,I represent star of final masses 1, 2, 4, 5, 6, 8, 10, 15 and, $20M_{\odot}$ respectively, using the power law accretion method including episodic bursts. .	119
5.1 The four different models and the accumulated mass as a function of time. From top to bottom, the plots show the results of stars of final masses $100M_{\odot}$, $10M_{\odot}$ and, $1M_{\odot}$ respectively	123
5.2 The maximum peak radius achieved for each of the smooth accretion models at each modelled mass. Note the accelerated model $100M_{\odot}$ result is obscured by the constant accretion data point.	125
5.3 Urquhart et al. (2014) ATLASGAL observational data. Luminosity and mass are given in solar units.	130
5.4 Frequency distribution of luminosity mass ratios from Urquhart et al. (2014) ATLASGAL data. L-M ratio is in solar units. . .	131
5.5 Normalised frequency distribution of L/M ratios from Urquhart et al. (2014) ATLASGAL data. Each object type was normalised against itself only.	132

5.6 The four smooth accretion models binned clump luminosity - clump mass data has been adjusted using the initial mass function from Kroupa (2001). The grey solid line is the binned ATLASGAL data Urquhart et al. (2014). Both sets of data are normalised.	137
5.7 This figure is taken from Calvet et al. (2000). The accretion versus time graph displays potential ideas on the evolution of disk accretion and the different phases that occur. Early infall burst accretion, moving to a more irregular 'noisy' disk accretion.	139
5.8 An ideal scenario depicting the growth of a sphere of influence by a protostellar core in a cylindrical filament. The black dot serves as a central point for a protostar. The red lines represent the sphere of influence, with dashed line as sphere at a future time. d is the diameter of cylinder, Δr is the change in radius, ΔL is the change in length.	140

List of Tables

4.1	A comparative table of final radii and final mass achieved using the respective accretion method. The masses highlighted here are a selection of relevant data points to the graphs featured.	57
4.2	The data table of final mass and peak radius achieved using the respective accretion method. The masses highlighted here are a selection of relevant data points to the graphs featured. Full data available in the digital appendix.	57
4.3	The data table of final mass and the final radius using the respective accretion method including episodic bursts. Note that the accelerated accretion method could not run to completion for final masses greater than $16M_{\odot}$.	94
4.4	The data table of final mass and peak radius achieved using the respective accretion method. Note that the accelerated accretion method could not run to completion for final masses greater than $16M_{\odot}$.	94
5.1	Table of clump masses and calculated fixed luminosities from the associated smooth accretion star models.	129
5.2	Table of clump masses and calculated fixed luminosities from the associated burst accretion star models.	130
5.3	Part one of tabled ATLASGAL observation data and key values found and used with the Kolmogorov Smirnov test.	133
5.4	Part two of tabled evaluated ATLASGAL data. The K-S test on this data is found with an α value of 0.05. A positive K-S score indicates that the difference between the data bins and a binned normal distribution function is less than the D_{crit} value, indicating a good fit.	133

A.1 Two Sample KS test results of MMB data. Tested using AT-LASGAL MMB object data against final mass stars of 1, 2, 4, 5, 6 and $8 M_{\odot}$.	148
A.2 Two Sample KS test results of MMB data. Tested using AT-LASGAL MMB object data against final mass stars of 10, 15, 20, 25 and $100 M_{\odot}$.	149
A.3 Two Sample KS test results of YSO data. Tested using AT-LASGAL YSO object data against final mass stars of 1, 2, 4, 5, 6 and $8 M_{\odot}$.	150
A.4 Two Sample KS test results of YSO data. Tested using AT-LASGAL YSO object data against final mass stars of 10, 15, 20, 25 and $100 M_{\odot}$.	151
A.5 Two Sample KS test results of HII data. Tested using ATLAS-GAL HII object data against final mass stars of 1, 2, 4, 5, 6 and $8 M_{\odot}$.	152
A.6 Two Sample KS test results of HII data. Tested using ATLAS-GAL HII object data against final mass stars of 10, 15, 20, 25 and $100 M_{\odot}$.	153

List of Abbreviations

ATLASGAL	APEX Telescope Large Area Survey of the Galaxy
GMC	Giant Molecular Cloud
HII	Hydrogen ₂
IMF	Initial Mass Function
ISM	InterStellar Medium
K-H	Kelvin Helmholtz
MMB	Methanol Multi Beam
MSS	Main Sequence Star
SOI	Sphere Of Influence
YSO	Young Stellar Object
ZAMS	Zero Age Main Sequence

Physical Constants

Speed of Light	$c_0 = 2.997\,924\,58 \times 10^{10} \text{ cm s}^{-1}$ (exact)
Solar Mass	$M_\odot = 1.989 \times 10^{33} \text{ g}$
Solar Radius	$R_\odot = 6.963 \times 10^{10} \text{ cm}$
Solar Luminosity	$L_\odot = 3.828 \times 10^{33} \text{ erg/s}$
Atomic Mass Unit	$\text{u} = 1.661 \times 10^{-24} \text{ g}$
Electron Mass	$m_e = 9.109 \times 10^{-28} \text{ g}$
Hydrogen Mass	$m_H = 1.6737 \times 10^{-24} \text{ g}$
Boltzmann Constant	$k = 1.381 \times 10^{-16} \text{ erg/K}$
Planck's Constant	$h = 6.626 \times 10^{-27} \text{ cm}^2 \text{ g s}^{-1}$
Reduced Planck's Constant	$\hbar = 1.0546 \times 10^{-27} \text{ cm}^2 \text{ g s}^{-1}$
Gravitational Constant	$G = 6.674 \times 10^{-8} \text{ cm}^3 \text{ g}^{-1} \text{ s}^2$
Pi	$\pi = 3.14159265359$

List of Symbols

Symbol	Represented	Unit
U	Gravitational Potential Energy	J
K	Kinetic Energy	J
M or m	Mass	g
R	Radius	cm
T	Temperature	Kelvin
A	Area	cm ²
P	Pressure	Newton/cm ²
P	Power	erg/s
V	Volume	cm ³
L	Luminosity	erg
F	Force	Newton
t	Time	s
μ	Average Molecular Weight	Dimensionless Number
ρ	Density	g cm ⁻³
v	Velocity	cm s ⁻¹
v	Frequency	Hz
κ	Opacity	Dimensionless Number
a	Acceleration	cm s ⁻¹
J	Impulse	Newton
p	Momentum	g cm s ⁻¹

Dedicated to Scientific Progression

Chapter 1

Introduction

Stars are the most fundamental objects in the Universe, they provide hosts for planetary systems and other celestial objects. The energy they provide is the driving force to many natural phenomena including life. Massive stars provide the highly energetic radiation that drives the turbulence in clouds aiding low mass star formation. Low mass stars form in large numbers locking up the majority of mass in their local cluster. The evolutionary star formation processes are relatively well understood however there is notable debate surrounding the early embedded stages. Observing the formation process is difficult due to the embedded nature of protostars, and the long time scale over which it occurs. New observations like those from the Herschel Space Observatory are improving the ability of imaging objects in optically thick clouds, however other methods are still required to achieve a complete understanding. A numerical model that is able to map stellar evolution from protostar to Main Sequence for all star masses is the next logical step for better understanding the processes and consequences involved with star formation. We aim to do this by modelling the evolutionary tracks for a range of star masses via variable accretion models. The fundamental basis for star formation is the gravitational collapse of a giant molecular cloud to form a protostellar core which further accumulates mass from the same cloud to eventually reach Main Sequence. There are many complexities involved in the process including radiation feedback and fragmentation.

Stellar astrophysics is a well documented field with many people working towards a general goal to better understand our place in the Universe. As such, star formation holds a central position in astrophysical research.

There are various fundamentals that are used as the basis of this thesis. A brief selection of which are listed here.

- Gravitational collapse of molecular clouds to form a protostellar core (Jeans, 1902).
- Protostellar core growth via circumstellar disk accretion due to conservation of angular momentum, 1.3. As a consequence, flow inversion due to radiation is avoided (Krumholz et al., 2009).
- Radiative feedback and magnetic fields have long range, in the order of 10^3 AUs, influence of star formation in the cloud (Krumholz et al., 2006).
- The equations that govern the internal evolution of protostellar cores (Hansen et al., 2004).

There remains a lot to be worked out and ideas that need further developing. This research will aim to provide insight into some of the more problematic ideas.

- Star formation occurs in thick molecular clouds blocking or hindering observation. As such, methods of implicitly drawing conclusions must be used.
- The accretion rate is still largely debated.
- Spherically symmetric accretion is largely disregarded, but the constant accretion rate it uses is still used widely in stellar modelling.
- Stars $> 10M_{\odot}$ are thought to accrue mass well into the Main Sequence, but their ability to do this is not understood.
- It is unknown if the stellar accretion method of low mass stars is applicable to high mass stars' formation.
- There has been evidence for the inclusion of episodic accretion bursts with recent works showing large fractions of mass being accumulated in a few hundred years (Hartmann & Kenyon, 1996). The effects and importance of which have not been fully developed.

- It is uncertain if accretion rates conform to one model throughout the entire evolution, or if there is a progressive change over the cycle. Recent works have postulated an accelerated accretion rate for high mass stars (Davies et al., 2011). The accretion rates for low mass stars are unsure as models have shown to be within error of each other (Offner & McKee, 2011).

We aim to address some of these problems through the use of a complete core evolution hydrodynamic code. Adjusting key variables and compiling the results to produce the evolutionary tracks for each model. We aim to be able to use the tracks and other data as guide to what is happening in the early embedded formation stages. We track the data of mass, luminosity and, temperatures throughout the entire evolution to then plot the model tracks. We then aim to compare the luminosity-mass (L/M) function to recent observational data from Urquhart et al. (2014). By the end of this thesis, we aim to have determined the effectiveness of the modelling approach to solve a variety of astrophysical problems, if the accretion models we used are viable and if the data produced can be used in aiding analysis of observations.

1.1 Star formation history

Star formation has been a point of serious debate in astrophysics for nearly two centuries, with many different opinions of the processes involved. In the 1800's, the laws of thermodynamics were applied to the idea of infalling material to provide the energy of the Sun. Lord Kelvin and Hermann von Helmholtz proposed that the Sun's energy was sourced from the pool of matter shrinking as it cooled (Helmholtz, 1856). They also realised the age of the Sun could be estimated by comparing the gravitational potential energy to the luminosity. As such the Kelvin-Helmholtz timescale (Eq. 2.112) was conceived, an equation that still holds great importance and an understanding of it is required later in our work.

The Kelvin idea for the energy source of the Sun would not be refuted successfully for fifty years due to limited knowledge in other related fields, namely atomic physics. With the progress made in understanding the atomic

structure it became known that under extreme gravitational conditions the electro-weak force could be overcome to combine atomic nuclei, resulting in a massive release of energy, this idea was gradually accepted as the prevailing theory, with further evidence from Aston (1920). It was apparent that this energy was essential "life support" for stars by providing the energy to maintain high internal pressures to prevent star collapse.

The material state of stars had long been assumed as a liquid, but in 1870 Homer Lane made the first calculations of stellar structure with the star being composed of a gas (Lane, 1870). His work aimed to determine surface temperature densities and pressure, and Whilst not completely successful, it was the first observed result of when stars lose energy the subsequent contraction would lead to an increase in temperature, not a decrease.

The early 1900's led to the first use of a polytropic model, where the pressure is dependent upon density. Robert Emden built upon previous work of a fully convective spherically symmetric perfect gas by including the idea of a pressure density relation which would later become known as the Lane-Emden equation. Using the established equations of hydrostatic equilibrium and mass conservation (Eq. 2.23 and Eq. 2.25), a derivation for the density dependence upon the radius of star could be found. This relation was dependent upon the polytropic index, a function that is derived from the bulk modulus.

In 1916, the idea of radiation pressure playing a crucial role in the stellar equilibrium became a viable theory. Arthur Eddington revisited the idea of radiation pressure as the major balancing force within stars and established many other principles associated. Eddington proposed that the temperature gradient through the star is determined by the distribution of energy sources within the star and the stellar opacity, which was evaluated mostly by electron scattering. Eddington established an upper limit of luminosity, at which point the radiation pressure would exceed the gravitational force resulting in rapid loss of stellar material. Eddington was working alongside Francis Aston when, in 1920 he published a paper on highly accurate mass measurements of isotopes Aston (1920). Aston found the individual masses of hydrogen atoms were greater than when combined into a helium atom, the deficit of mass was related to energy by the speed of light squared. This

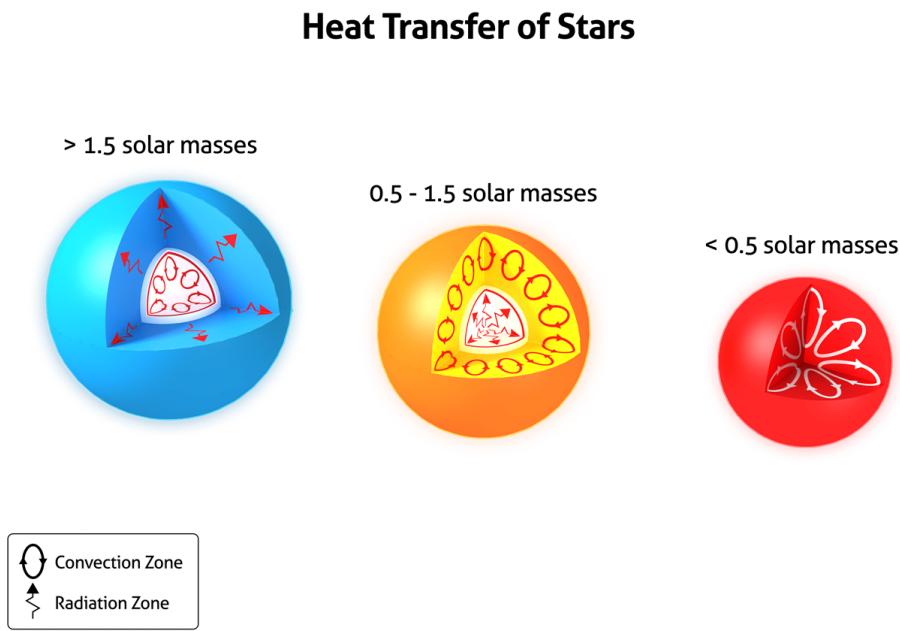


FIGURE 1.1: The modern understanding of the convective and radiative structures contained within stars. The low mass stars are fully convective which would comply with Emden's work. The greater masses have more complex systems involving both convective and radiative sectors.
(Sun.org, 2016)

revolutionary finding allowed Eddington to reach the conclusion that the energy source within a star came from the combining of hydrogen into helium (Eddington, 1920).

From the 1930's through to the 1950's further development in atomic and quantum physics would give way to new, more complete, understanding of Main Sequence evolution, including the proton-proton cycle and, the carbon-nitrogen-oxygen cycle. Both fusion cycles are crucial for comprehensive evolutionary models.

Subrahmanyan Chandrasekhar and Eddington both individually worked upon post Main Sequence astrophysics and extremely dense stars. Observation of a star in a binary system, now known as 40 Eridani, had shown a spectral type of a very hot white star, but with a relatively low luminosity, this was the first discovery of a white dwarf star. Eddington stated that the observed density of the white dwarf was completely plausible. Chandrasekhar would eventually go on to derive the upper limit of white dwarf mass which could be stable due to electron degeneracy pressure countering

gravity (Chandrasekhar, 1931).

By this point in time the majority of the Main Sequence cycle, from birth to death, was known but not understood. The 1950's gave way to electromagnetic astronomy, Radio, X-ray, Gamma ray, ultra-violet and infrared telescopes had advanced technologically enough to become viable for astrophysical observations. This progression opened up the Universe, allowing deeper and further study than ever before. Star forming regions of dark molecular clouds were now accessible and soon became known as the nurseries of which stars are born. Previously never seen before star clusters were now observed deep within their local cloud.

Long term evolution of star formation calculations were labourious and largely impractical before the advent of computers. Mentioned by Martin Schwarzschild (Schwartzchild, 1962);

"A person can perform more than twenty integration steps per day...so that for a typical single integration of, say, forty steps, less than two days is needed."

The 1960's would give astrophysicists access to the computation power needed to run simulations and reduce the need for laborious calculations. Conversion from mathematical integrations to computational compatible methods were required. During this time period Louis G. Henyey produced an automatic solution finder for stellar evolution equations, now known as the Henyey method (Bodenheimer et al., 2006), a numerical method that is used within the main code of this thesis.

Modern simulation and modelling approaches to star formation are still crucial to astrophysical understanding. Protostars are naturally much colder than their Main Sequence counterpart and are still embedded within their molecular cloud which hides signature evidence of the star. The time spent in the protostellar and pre-Main Sequence are very short in comparison to the full life cycle so, observationally they appear fewer in number. Even with modern space telescopes, finding and defining protostars is still very difficult. Modelling can help by converting principle mechanisms and materials into a simulated environment in which we can 'watch' unhindered. Modelling also has the advantage that the entire process is mapped from beginning to end, giving a visualisation of the full cycle not just a snapshot

as is found with observation.

In chapter 2, a quantitative evaluation is given of the accepted principle physics which is used in astrophysics and this thesis. Here however, we summarise the process for introductory purposes.

Giant molecular clouds contain thousands to several million solar masses of material, which is balanced in an equilibrium of gas pressure, kinetic energy and gravity. An isolated system could exist almost perpetually. However, radiative losses will reduce the energy contained within over time, combined with turbulent winds the equilibrium is destabilised and collapse occurs. This is referred to as triggered formation. The mass requirement for star formation is known as the Jeans mass.

A collapsing region will continue towards a protostellar stage if the gravitational potential energy is successfully displaced through radiative losses. A central region will become the protostellar core when its opacity increases to a point where its internal energy cannot be removed. Further collapse of outer gaseous regions only increase the core temperature through shocks. On reaching around $2000K$ hydrogen molecules will begin to dissociate. Infalling matter will coalesce into a circumstellar disk through which matter will accrete onto the star. This disk allows for bipolar outflows in which the energy can be dissipated, this reduces the radiation pressure on the disk and angular momentum of the disk, allowing for accretion to continue.

Once the temperature has increased sufficiently, deuterium fusion begins. This process maintains internal core temperatures and allows the continuation of mass accretion before the hydrogen burning stages can begin, at which point the star would be considered Main Sequence. Beyond this is the post Main Sequence phase and the end-of-life paths that will be taken depending upon star mass, these stages are beyond the aims of this paper which just focuses on protostellar to Main Sequence.

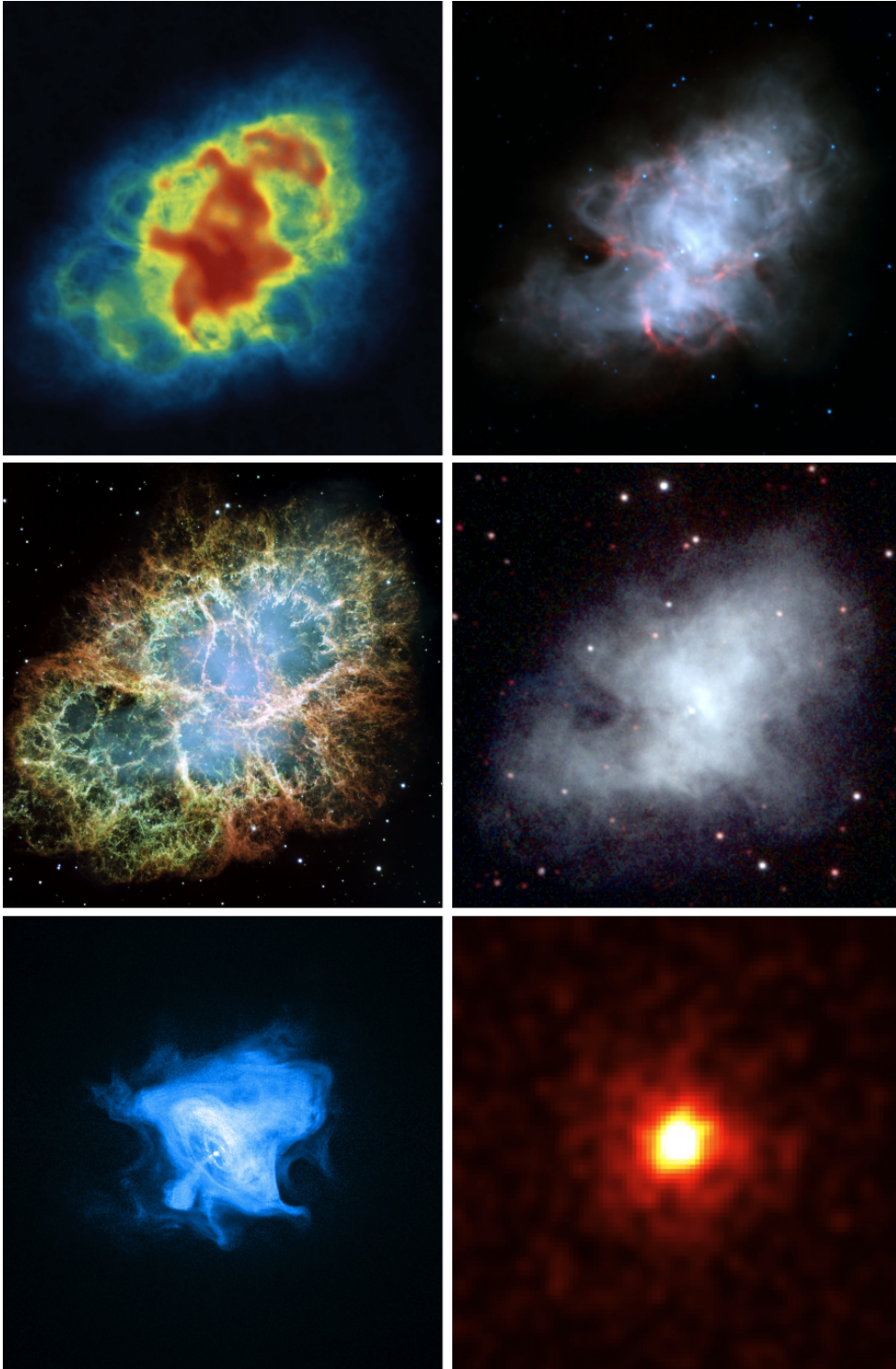


FIGURE 1.2: A collection of images of the Crab Nebula (NGC 1952) highlight differences found in the different wavebands. The left column, from top to bottom, contains radio, visible and x-ray wavelengths. The right column, from top to bottom, contains infrared, ultraviolet and gamma ray wavelengths. Infrared spectra shows the cooler star forming regions whilst ultra violet show intense heat of Main Sequence stars. Note the radio image is a combination of two different radio wavebands combined. Credit to; NRAO (2016b), NRAO (2016a), NASA/JPL-Caltech/R. Gehrz (University of Minnesota) (2016), NASA, ESA, J. Hester and A. Loll (Arizona State University) (2016), NASA/Swift/E. Hoversten, PSU (2016), NASA/CXC/SAO/F.Seward et al (2016), NASA/DOE/Fermi LAT/R. Buehler (2016)

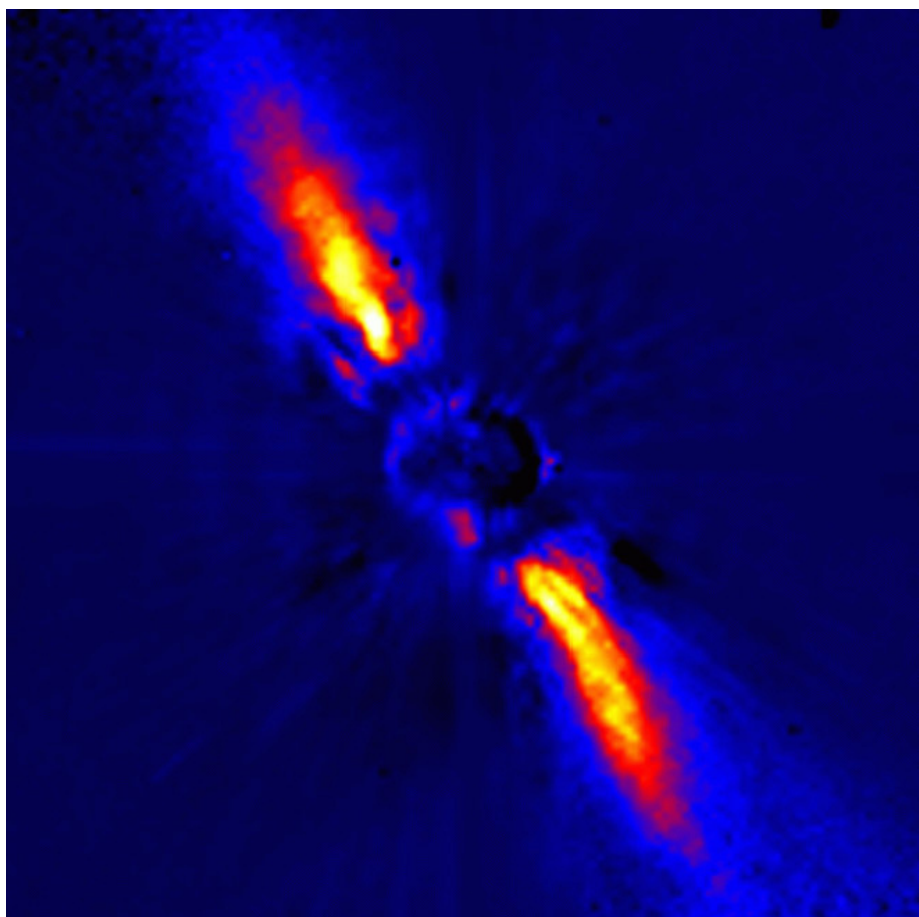


FIGURE 1.3: A false colour image of β Pictoris in the infrared band. The bright regions on opposite sides of the centroid show the remnants of an accretion disk around a young star. It is likely that the remaining disk will go on to form planets. Credit to Jean-Luc Beuzit, et al. Grenoble Observatory, European Southern Observatory (2016)

Chapter 2

Method Theory

This section will lead through the majority of background knowledge required to understand the early pre-main sequence evolution of stars and the hydrodynamic code used in this thesis. Starting with the well understood theoretical physics and evolutionary mechanics, then moving to how this translates into a computational simulation. (Note: All symbols and constants are defined with their units in the symbols and constants lists before the introduction.)

2.1 Jeans Criterion

The first stage to star formation requires a molecular cloud, a region of diffuse gas and dust (typically 100-300 molecules per cm^3), with enough mass where a star can begin to form. The criteria required for collapse into a proto-star is defined by the Jeans Mass. Assuming a spherical cloud, a portion of the cloud can be determined to collapse if the local gravitational force is greater than the pressure from within. Assuming a spherical cloud of uniform density, the gravitational potential energy of the cloud can be approximated as

$$U \sim -\frac{3}{5} \frac{GM_c^2}{R_c} \quad (2.1)$$

Where M_c and R_c are the mass and radius of the cloud, respectively. From virial theorem, a gravitationally balanced system can be shown as stable when

$$2K + U = 0 \quad (2.2)$$

where K is kinetic energy. A cloud's internal kinetic energy can be approximated as

$$K = \frac{3}{2} N k T \quad (2.3)$$

Where N is the number of particles, which we can also define using

$$N = \frac{M_c}{\mu m_H} \quad (2.4)$$

Where μ is the average molecular weight. From 2.2 we can see that gravitational collapse will occur when $2K < |U|$, and then substituting what we just defined

$$3 \frac{M_c k T}{\mu m_H} < \frac{3}{5} \frac{G M_c^2}{R_c} \quad (2.5)$$

We can define the radius of a cloud assuming initial density of ρ_0 , to replace the mass of the system.

$$R_c = \left(\frac{3 M_c}{4 \pi \rho_0} \right)^{1/3} \quad (2.6)$$

Now we can substitute this into 2.5 to find the Jeans mass.

$$M_J \simeq \left(\frac{5 k T}{G \mu m_H} \right)^{3/2} \left(\frac{3}{4 \pi \rho_0} \right)^{1/2} \quad (2.7)$$

It should be noted, this derivation works under the assumption that the entirety of the cloud is collapsing and that the thermal energy is the dominant source of outward pressure. If, however, the spherical section of mass is embedded within a GMC it will be subject to an external pressure which will reduce the mass required. Known as the Bonner-Ebert mass it is given as

$$M_{BE} = \frac{c_{BE} v_T^4}{\rho_0^{1/2} G^{3/2}} \quad (2.8)$$

Where

$$v_T = \sqrt{k T / \mu m_H} \quad (2.9)$$

is the speed of sound in the isothermal material. c_{BE} is a dimensionless constant of $\simeq 1.18$

We can also use the definitions of timescales to determine if a cloud will collapse or expand. The time scale of expansion driven by radiation

$$t_s \simeq \frac{R}{c_s} \propto \frac{R\rho^{\frac{1}{2}}}{P^{\frac{1}{2}}} \propto m^{\frac{1}{3}}\rho^{-\frac{1}{3}}T^{-\frac{1}{2}} \quad (2.10)$$

Where R is radius of the cloud. c_s is the speed of sound in the material. ρ is the density of the cloud. T is the temperature. P is pressure and m is mass.

The timescale of free fall collapse is given as:

$$t_{ff} \simeq \left(\frac{Gm}{r^3} \right)^{-\frac{1}{2}} \propto (G\rho)^{-\frac{1}{2}} \quad (2.11)$$

Where G is the gravitational constant.

As such a star can be shown to collapse if $t_{ff} \ll t_s$.

More recent work has shown that the Jeans criteria, whilst classically correct, is not the main mechanism of collapse. GMCs do not exist in a calm motionless state, energy input from local clusters will cause turbulent motion within the clouds. The turbulence will cause confined dense regions which then exceed the Jeans criteria. So whilst the Jeans criteria is applicable to some extent, the turbulence induced changes happen on timescales much shorter than if the cloud were only subject to the free fall collapse. As such, it is much more likely that turbulence is the initial cause of collapse which is then taken over by gravity.

2.1.1 Fragmentation

Once a cloud has exceeded the Jeans criteria and has begun to collapse, a process of fragmentation takes place. Fragmentation is problematic in understanding massive star formation. It would follow that a massive star forms from a cloud in which its mass is many times the final mass of the star. However, as a molecular cloud collapses its density increases, which leads to portions of the cloud exceeding the Jeans criteria, the cloud then begins to fragment into multiple collapsing regions. The size of these fragmenting regions can be found by:

$$\frac{d^2r}{dt^2} = \frac{Gm(r)}{r^2} - \frac{1}{\rho} \frac{\partial \rho}{\partial r} = \frac{-Gm}{r^2} - 4\pi r^2 \frac{\partial \rho}{\partial m} \quad (2.12)$$

(The derivation of 2.12 can be found in SOURCE HERE as it is long and non-essential to this work.)

The process of fragmentation will continue until either radiation feedback increases the temperature, and thus internal pressure, enough to prevent collapse. The other method of fragmentation suppression is through magnetic field interactions.

The optical depth of a material is defined as the ratio between the incident and emitted radiation power through the material. The more optically thick a material is, the greater attenuation of radiative power through it is. The point where radiation can not travel through the material without being absorbed is the definition of being optically thick. Initial isothermal cloud collapse results in the internal temperature increasing. When the cloud is optically thin, this energy can escape as radiation allowing the cloud to cool and keep collapsing. As the density increases, the cloud becomes optically thick and this radiation can not escape. The optical depth is defined by the absorption of photons travelling through a medium:

$$\tau_\lambda = \int_0^s \kappa_\lambda \rho ds \quad (2.13)$$

Where s is the length travelled through a medium by a photon, κ_λ is the absorption coefficient of the material for a specific wavelength and rho is the density of the material. We define a material as optically thick when a photon is absorbed and emitted many times, such that $\tau_\lambda \gg 1$.

When the cloud is optically thick, the radiation is mostly contained, thus increasing the internal gas pressure. This counters the gravitational force preventing further collapse. This process, known as radiation feedback, works best in the central regions of a collapsing molecular cloud up to $\simeq 1000 AU$. Discussed later, is how stars form through a circumstellar disc which the cloud will feed into rather than directly onto the protostar. Due to the Jeans mass requirement being dependent on $T^{3/2}$, even a moderate increase in temperature increases the mass requirement by factors of $\simeq 10$ thus slowing or stopping fragmentation.

Magnetic fields work in two ways to prevent fragmentation. Firstly, a

collapsing cloud needs to preserve angular momentum, doing so by rotating faster around the centroid as it moves closer to that point. However, with the presence of magnetic field lines threaded throughout the cloud, the faster rotation in the inner rings, cause the field lines to become twisted. This twisted field generates a tension force, moving angular momentum from inner regions to the outer. Commonly known as magnetic braking, the result aids the collapse process drastically. The second effect of magnetic fields is similar to radiative feedback, in that the mass of the cloud must overcome magnetic flux pressure. Whilst many regions in clouds have a supercritical mass able to overcome the magnetic flux, it still provides a preventative force which is shown in simulations to prevent fragmentation by factors of ≈ 2 , (Krumholz, 2014).

There are complications in the fragmentation stages, notably starvation. Fragmentation starvation is a common outcome (Girichidis et al., 2011) in hydrodynamic simulations where stars can not accumulate enough material to reach higher masses, however this was not explored in this thesis.

2.2 Stellar Equilibrium

The equilibrium of a star is reached when gravitational force is balanced by the internal pressure. We can use these balanced equations at all stages of the stars life, from protostar to main sequence, to determine its current state. The gravitational force upon a small mass located at distance r from centre of spherically symmetric sphere:

$$F_{Grav} = \frac{-GM_r\Delta m}{r^2} \quad (2.14)$$

Where M_r is the interior mass, inside a sphere of radius r . Pressure being:

$$P \equiv \frac{F}{A} \quad (2.15)$$

Where F is force, and A is area. If we consider first a cylindrical system of; length r , mass dm and, circular face of area A , at distance from a star. The

differential of force across the cylinder is

$$dF_{Pres} = -AdP \quad (2.16)$$

By using Newton's second law, we can now define the total force present with change in radius over time.

$$dm\ddot{r} = F_g + dF_{Pres} = -\frac{GM_r dm}{r^2} - AdP \quad (2.17)$$

Replacing the differential mass element with density.

$$dm = \rho A dr \quad (2.18)$$

Substituting into 2.17 and dividing by the volume.

$$\rho\ddot{r} = -\frac{GM_r\rho}{r^2} - \frac{dP}{dr} \quad (2.19)$$

This is the time dependent relation of the described scenario, substituting for spherical geometry we get

$$\ddot{r} = -\frac{Gm}{r^2} - \frac{\partial P}{\partial r} \frac{1}{\rho} \quad (2.20)$$

and considering the relation

$$dr = \frac{dm}{4\pi r^2 \rho} \quad (2.21)$$

we can get the spherical time dependent relation of forces over the sphere.

$$\ddot{r} = -\frac{Gm}{r^2} - 4\pi r^2 \frac{\partial P}{\partial m} \quad (2.22)$$

Once the star is in a state of equilibrium, i.e. no longer time dependent we can finally see the forces balanced using

$$\frac{dP}{dm} = -\frac{Gm}{4\pi r^4} \quad (2.23)$$

It must be noted that there must exist a pressure gradient throughout the sphere or protostar to counter gravity.

2.3 Mass Conservation

Considering a spherically symmetric star with a thin shell of mass dM_r and thickness dr , located at distance r . The mass of the shell can be approximated to be

$$dM = \rho(4\pi r^2 dr) \quad (2.24)$$

and as such we can derive the mass conservation equation.

$$\frac{dM_r}{dr} = 4\pi r^2 \rho \quad (2.25)$$

This mass conservation shows the density of material decreases with distance from the stellar centre.

2.4 Upper Mass Limit

There are several problems that outline a hard limit to the mass a star can reach through accretion, these problems include stellar winds and ionisation feedback, we will focus on two of the more directly influential problems to our model. The first being fragmentation, already discussed, and the second being radiation feedback. The radiation problem arises from the equilibrium of mass-to-radiation pressure, and that at some point the internal energy, and therefore radiation pressure, will be greater than the gravitational force. We can find this limit by equating the inward acceleration of gravity (Eq. 2.14) and the outward force of luminosity, defined as

$$F_{rad} = \frac{\kappa L}{4\pi r^2 c} \quad (2.26)$$

where κ is the opacity constant. Gravitational acceleration can be shown as dominant only if

$$\frac{L}{M} < \frac{4\pi Gc}{\kappa} = 2500 \left(\frac{\kappa}{5cm^2g^{-1}} \right)^{-1} \frac{L_\odot}{M_\odot} \quad (2.27)$$

From observations we know that proto stars exceeding $\sim 20M_\odot$ have luminosities greater than $2500L_\odot$. As such, it would stand that a protostar exceeding $20M_\odot$ would generate radiation pressure great enough to blow

away and starve itself of all further mass (Klassen et al., 2016). The first understanding to how stars continue to accrete mass lies in the assumption about spherical nature and uniform radiation from the protostar's surface on to the surrounding cloud. An upper mass limit of $\sim 40M_{\odot}$ is found in spherically symmetric simulation (Hosokawa & Omukai 2009). We know from observation that this $\sim 40M_{\odot}$ upper limit is not found in reality, and that stars much more massive are able to form. A different mechanism of formation must exist.

We know that molecular clouds hold a non-zero angular momentum value as such, when matter falls inwards toward the protostellar core the angular momentum is conserved, and thus results in the accreting matter to form into a flattened accretion disk along the axis of net angular momentum. This also allows for 'beamed' radiation to be emitted from opposing polar regions, perpendicular to the flattened disc. Thus, the polar radiation force over a significant solid angle will far exceed the gravitational force, creating radiation driven cavities. The resulting bipolar radiation reduces the pressure on the accretion disc thus, the gravitational force along the disk axis is then great enough to overcome radiation pressure and continues accreting mass onto the protostar. New simulations such as figure 2.1 show strong agreement with this idea (Krumholz et al. (2009), Kuiper et al. (2011)).

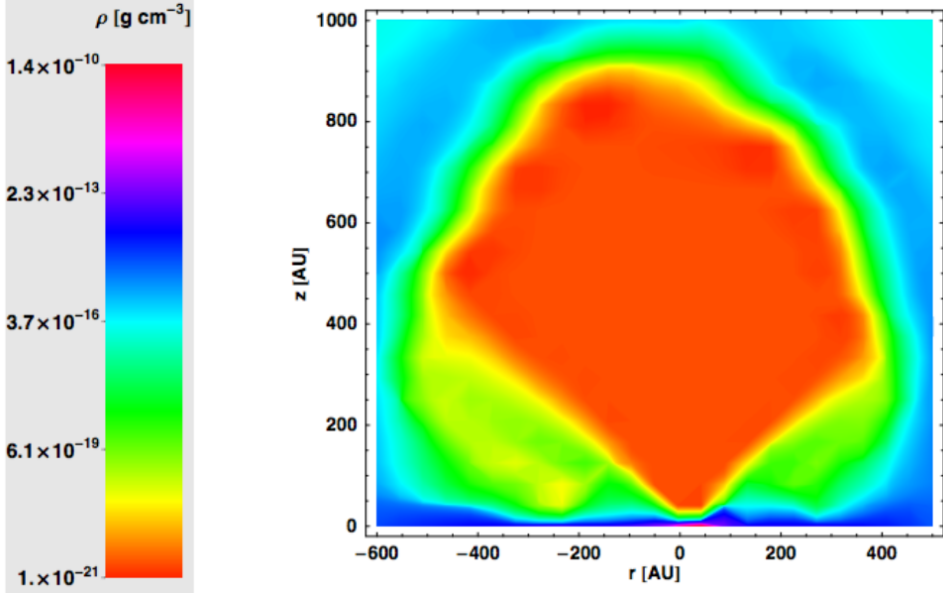


FIGURE 2.1: A heat map view of gas densities across the x-z plane of a 3D simulation (Kuiper et al., 2011). The image comes from the model at 10kyr and $120M_{\odot}$ protostellar core. The protostellar region of high density can be seen at centered at the bottom of the figure.

2.5 Pressure

To fully understand the equations 2.23 and 2.25, we must determine the pressure of the cloud system as an equation of state. The total pressure within a star comes from several sources, including radiation, gas pressure and degeneracy pressure, the derivations of which will be outlined below.

Derivations using methods from Carroll & Ostlie (2006)

The ideal gas law is an equation of state which will be used to help determine the other pressure relations involved in the star system.

$$PV = NkT \quad (2.28)$$

where k is the Boltzmann constant and N is number of particles in the system. It must be noted that the ideal gas law assumes the particles as hard spheres, i.e, monoatomic helium. However, the molecular clouds can consist of many molecular compounds which are diatomic (Hydrogen, H_2 , Carbon Mon-oxide, CO) or polyatomic (Ammonia, NH_3). Internal temperatures therefore must consider the internal energies of the molecules. The internal energies are related by the degrees of freedom within the molecule

and must be considered in calculating the total energy of a gas.

$$U = \frac{f}{2}nRT \quad (2.29)$$

Where U is the internal energy of a molecule, f is the number of degrees of freedom of the molecule, n is the number of moles, R is the ideal gas constant and T is the temperature.

2.5.1 Pressure Integral

Taking a cylinder of length Δx and cross sectional area A , containing a gas of point like particles all of mass m , figure 2.2. The gas is assumed to behave like an ideal gas, i.e. interacts via perfectly elastic collisions, the distance between particles is much greater than the particle size and the particles are hard spheres (mon-atomic). The gas incident to the walls of the container will change momentum entirely along the normal axis. Using Newtons second and third law

$$f = ma = \frac{dp}{dt} \quad J = \int_{\Delta t} f dt = \Delta p \quad (2.30)$$

Where J is impulse. From our scenario we can determine that the impulse imparted on the wall is the negative of the change in momentum experienced by the particle.

$$f \Delta t = -\Delta p = 2p_x \hat{i} \quad (2.31)$$

The gas will travel twice the length of the container before hitting the wall again. The time between these intervals is then defined

$$\Delta t = 2 \frac{2x}{v_x} \quad (2.32)$$

Where v_x is the velocity along the x axis. The speed scalar of the particle will remain constant due to the perfect elastic collisions. The average force exerted by a particle is then given

$$f = \frac{2p_x}{\Delta t} = \frac{p_x v_x}{\Delta x} \quad (2.33)$$

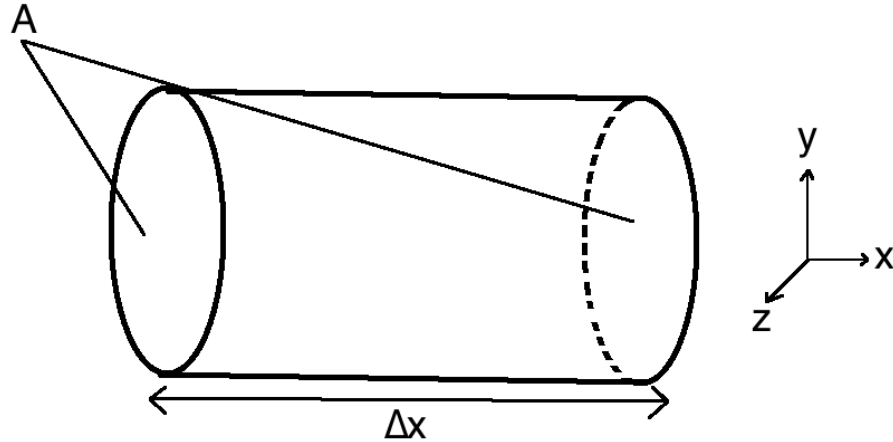


FIGURE 2.2: A diagram showing the scenario of a 'first principles' gas in a cylinder.

Given the velocity vector is

$$v^2 = v_x^2 + v_y^2 + v_z^2 \quad (2.34)$$

and for a system containing a large number of particles it can be assumed

$$\bar{v}_x^2 = \bar{v}_y^2 = \bar{v}_z^2 = \frac{v^2}{3} \quad (2.35)$$

As such the average force per particle is

$$f(p) = \frac{1}{3} \frac{pv}{\Delta x} \quad (2.36)$$

The particles in the cylinder will have a range of momenta between p and $p + dp$ and we can then define the number of particles with this momenta as $N_p dp$. Then the total number of particles in the box is given

$$N = \int_0^\infty N_p dp \quad (2.37)$$

with the total force of these particles given

$$dF(p) = f(p)N_p dp = \frac{1}{3} \frac{N_p}{\Delta x} p v d p \quad (2.38)$$

Integrating over all momentum

$$F = \frac{1}{3} \int_0^\infty \frac{N_p}{\Delta x} p v dp \quad (2.39)$$

Noting that the volume of the cylinder is the area of the cross section multiplied by the length, $\Delta V = A\Delta x$.

$$n_p dp \equiv \frac{N_p}{\Delta V} dp \quad (2.40)$$

so the pressure exerted on the wall of the cylinder is

$$P = \frac{1}{3} \int_0^\infty n_p p v dp \quad (2.41)$$

We have arrived at the pressure relation to the number density of particles in the system. This equation will work for massless and massive particles. Going further, we will evaluate the equation for an ideal gas in terms of the average molecular weight.

2.5.2 Ideal Gas Pressure

In the case where the gas is non-relativistic we can equate momentum to mass multiplied by velocity, $p = mv$. Which we can substitute into equation 2.41

$$P = \frac{1}{3} \int_0^\infty m n_v v^2 dv \quad (2.42)$$

Where $n_v dv$ has replaced $n_p dp$ and now represents the number of particles in the gas with speeds between v and $v + dv$. In an ideal gas we can use the Maxwell-Boltzmann velocity distribution as the function $n_v dv$.

$$n_v dv = n \left(\frac{m}{2\pi kT} \right)^{\frac{3}{2}} e^{-mv^2/2kT} 4\pi v^2 dv \quad (2.43)$$

where $n = \int_0^\infty n_v dv$. When equation 2.43 is substituted back into the pressure integral equation 2.41 and after simplification we get

$$P_g = nkT \quad (2.44)$$

the number of particles can be replaced by taking the density of the gas and dividing by the average mass of particles in the system.

$$P_g = \frac{\rho kT}{\bar{m}} \quad (2.45)$$

Where \bar{m} is average mass of the particles in the gas. We can now define this mean molecular weight average in terms of hydrogen atom masses.

$$\mu = \frac{\bar{m}}{m_H} \quad (2.46)$$

which we can now use to define the ideal gas pressure relation in terms of molecular weights.

$$P_g = \frac{\rho kT}{\bar{m}} \quad (2.47)$$

To go further and simplify the definition of the equation, we can define the average molecular weight in relation to hydrogen masses.

$$\mu \equiv \frac{\bar{m}}{m_H} \quad (2.48)$$

where m_H is mass of a hydrogen atom. As such

$$P_g = \frac{\rho kT}{\mu m_H} \quad (2.49)$$

we have now arrived at the final relation of gas pressure to average molecular weight. This average molecular weight is more complex for star systems as the gases contain a large mix of elements all in various ionisation states. The ionisation plays a part as the free electron gas must also be considered. The two final equations for average molecular weight of a neutral and a fully ionised gas can be stated respectively as

$$\frac{1}{\mu_n} \simeq X + \frac{1}{4}Y + \left\langle \frac{1}{A} \right\rangle_n Z \quad (2.50)$$

and

$$\frac{1}{\mu_i} \simeq 2X + \frac{3}{4}Y + \left\langle \frac{1+z}{A} \right\rangle_i Z \quad (2.51)$$

where X is the fraction of Hydrogen, Y is the fraction of Helium, and Z is the fraction of heavier elements. $\left\langle \frac{1}{A} \right\rangle_n$ is the averaged weight of the

heavier elements. For young stars the typical values of X, Y and Z are $\approx 0.70, 0.28, 0.02$ respectively, which correspond to values of, $\mu_n = 1.30$ and $\mu_i = 0.62$.

2.5.3 Radiation Pressure

Emitted radiation will generate a pressure due to the momentum imparted by photons in absorption or reflections. The momentum of a photon is defined as:

$$p_\gamma = \frac{hv}{c} \quad (2.52)$$

Where h is the Planck constant, v is the frequency of the photon, c is the speed of light. Going back to the fundamental pressure integral equation 2.41, we can substitute the photon value of momentum, noting the interchangeable relation that $n_p dp = n_v dv$.

$$P_{rad} = \frac{1}{3} \int_0^\infty h v n_v dv \quad (2.53)$$

We can go further by noting that $n v d v$ is the number density of photons with frequencies in the range from v to $v + dv$. Multiplying by the energy of each photon over that frequency range, we get energy density.

$$P_{rad} = \frac{1}{3} \int_0^\infty u_v dv \quad (2.54)$$

If we then substitute the energy density, $u_v dv$, for the Planck blackbody radiation distribution and integrating we get

$$P_{rad} = \frac{1}{3} a T^4 \quad (2.55)$$

where the radiation constant $a \simeq 7.566 \times 10^{-16} J m^{-3} K^{-4}$. This is our final expression of pressure driven by radiation from a blackbody of $T > 0K$. A true black-body can not really exist as objects will not perfectly absorb and emit radiation, thus Eq.2.55 requires a multiplicative factor of the emissivity of the object.

$$P_{rad} = \frac{1}{3} a \epsilon_\lambda T^4 \quad (2.56)$$

Where ϵ_λ is the emissivity factor at a specific wavelength as emissivity of a material is rarely a normal distribution across all wavelengths. Thus, summing the power across many wavelengths would give a better value of total power in real observations.

2.5.4 Degeneracy Pressure

So far the pressures defined have been described using classical physics, however we must account for the quantum mechanical contributions within the system. It can be seen from Eq. 2.28, that as $T \rightarrow 0, V \rightarrow 0$. We know however that particles will have to occupy a non-zero volume even if temperature is ~ 0 . As such, at a point where the gas particles occupy a small volume with low energies (corresponding to the low temperatures), they will break the Pauli exclusion principle. To avoid this the particles must hold a higher momentum than classical physics would dictate.

The maximum energy of an electron in a completely degenerate gas at $T = 0K$, is given by the Fermi energy, ϵ_F . This maximum energy is determined by a 3d wave-in-a-box scenario and using the de Broglie wavelength momentum relation. Assuming a box of length L on each side contains an electron represented by a standing wave function. The wavelength of the electrons can be stated as

$$\lambda_x = \frac{2L}{N_x} \quad \lambda_y = \frac{2L}{N_y} \quad \lambda_z = \frac{2L}{N_z} \quad (2.57)$$

Where $N_{x/y/z}$ is the integer quantum number associated with the respective axis dimension. Using the de Broglie relation we can define these wavelengths as momenta

$$p_x = \frac{hN_x}{2L}, \quad p_y = \frac{hN_y}{2L}, \quad p_z = \frac{hN_z}{2L} \quad (2.58)$$

So the total energy of a particle is written

$$\epsilon = \frac{p^2}{2m} \quad (2.59)$$

where $p^2 = p_x^2 + p_y^2 + p_z^2$ and, as such, the total energy in this model is

$$\epsilon = \frac{\hbar^2}{8mL^2} (N_x^2 + N_y^2 + N_z^2) = \frac{\hbar^2 N^2}{8mL^2} \quad (2.60)$$

Each electron holds an intrinsic spin value of $\pm 1/2$ and as such the total of unique quantum numbers N_x, N_y, N_z , is equal to two times the total number of electrons in the gas. Assuming a large enough sample of electron, which a protostar system would have, the space occupied would be out to a radius of $N = \sqrt{N_x^2 + N_y^2 + N_z^2}$ for positive N -space values. This evaluates the total number of electrons within a given space.

$$n_e = 2\left(\frac{1}{8}\right)\left(\frac{4}{3}\pi N^3\right) \quad (2.61)$$

Rewriting in terms of N

$$N = \left(\frac{3n_e}{\pi}\right)^{\frac{1}{3}} \quad (2.62)$$

Substituting into equation 2.60 we can determine the Fermi energy.

$$\epsilon_F = \frac{\hbar^2}{2m_e} (3\pi^2 n_e)^{\frac{2}{3}} \quad (2.63)$$

where m_e is the mass of an electron and n_e is the number of electrons within the volume of the system, $n_e = N_e/L^3$. Now, with the definition of Fermi energy we can use it to determine the degeneracy pressure. We make the assumption that the condition for degeneracy has been met, which is stated as

$$\frac{T}{\rho^{2/3}} < \mathcal{D} \quad (2.64)$$

where

$$\mathcal{D} = \frac{2\epsilon_F}{3k\pi^2} \quad (2.65)$$

With degeneracy being greater for smaller values of $T/\rho^{2/3}$. To find the pressure due to degeneracy we must combine the Pauli exclusion principle and the Heisenberg uncertainty principle. Using equation 2.41, and making the assumption that momentum of each electron is equal, it becomes

$$P \approx \frac{1}{3} n_e p v \quad (2.66)$$

with n_e being electron number density. In a completely degenerate gas the separation between electrons is $\sim n_e^{-1/3}$, as such the uncertainty of position cannot be larger than their physical separation, so $\Delta x \approx n_e^{-1/3}$. So now we can calculate the momentum in one axis as

$$p_x \approx \Delta p_x \approx \frac{\hbar}{\Delta x} \approx \hbar n_e^{1/3} \quad (2.67)$$

We can also assume that momentum in each of the three axes is equally likely and therefore we can assume the same value. From equipartition theorem we can say that

$$p^2 = p_x^2 + p_y^2 + p_z^2 = 3p_x^2, \quad p = \sqrt{3}p_x \quad (2.68)$$

We can now define the momentum using the number density of electrons that are fully ionised.

$$p \approx \sqrt{3}\hbar n_e^{1/3} \quad (2.69)$$

For non-relativistic speeds we know $v = \frac{p}{m_e}$, and as such

$$v \approx \frac{\sqrt{3}\hbar}{m_e} n_e^{1/3} \quad (2.70)$$

As such we can now substitute equations 2.70 and 2.67 into the new pressure integral, equation 2.66, resulting in the degeneracy pressure.

$$P = \frac{(3\pi^2)^{2/3}}{5} \frac{\hbar}{m_e} n_e^{5/3} \quad (2.71)$$

and then, by evaluating the electron number density in terms of the ratio between protons and nucleons in the system, we can find the degeneracy pressure for our protostar.

$$P = \frac{(3\pi^2)^{2/3}}{5} \frac{\hbar}{m_e} \left[\left(\frac{Z}{A} \right) \frac{\rho}{m_H} \right]^{5/3} \quad (2.72)$$

The electron degeneracy pressure during early stages of the star formation contributes a small, but not insignificant portion of total pressure. If we take a typical density of an early protostar 10^{23} cm^{-3} with average number of electrons per molecule as 1.9 (70% H, 30% He), using Eq.2.72 we get

$$P \approx 1.24 \times 10^{-17} \text{ kg m}^{-1} \text{ s}^{-2}.$$

It must be noted that this is the non-relativistic case, the relativistic case again has a greater effect in later stages of the stars life where energy is much higher. It must also be noted that the neutron degeneracy pressure and the Chandrasekhar limit are not considered, as it only becomes significant in the after the main sequence of a star, when the main fusion cycle's fuel has been consumed, a stage far beyond the early tracks we are researching.

2.6 Equilibrium

The Virial theorem is used to determine the relation between gravitational and internal energy.

$$V \frac{dP}{dm} = -\frac{1}{3} \frac{Gm}{r} \quad (2.73)$$

$$VdP = d(PV) - PdV = d(PV) - \frac{P}{\rho} dm = -\frac{1}{3} \frac{Gmdm}{r} \quad (2.74)$$

$$\int_{\text{centre}}^{\text{surface}} d(PV) = 0 \quad (2.75)$$

$V=0$ at the centre and $P(M)=0$ at the surface.

$$-3 \int_0^M \frac{P}{\rho} dm = - \int_0^M \frac{Gmdm}{r} = \Omega \quad (2.76)$$

Where Ω is the total gravitational potential energy. Using this theorem, and applying it to an ideal gas with particles of mass m_g , the temperature relation to the total internal energy.

$$P = \left(\frac{\rho}{m_g} \right) kT \quad (2.77)$$

The total internal energy at this phase of the stellar cycle is just the total kinetic energy of the particles.

$$U = \frac{3}{2} \frac{kT}{m_g} = \frac{3}{2} \frac{P}{\rho} \quad (2.78)$$

Substituting Eq. 2.78 and Eq. 2.76.

$$U = -\frac{\Omega}{2} \quad (2.79)$$

and also

$$U = \int_0^M \frac{3}{2} \frac{kT}{m_g} dm = \frac{3}{2} \frac{k}{m_g} \int_0^M T dm = \frac{3}{2} \frac{k\bar{T}M}{m_g} \quad (2.80)$$

Where \bar{T} is the average temperature, being defined as

$$\bar{T} = \frac{1}{M} \int_0^M T dm \quad (2.81)$$

As such, the average temperature is related to the gravitational potential energy by

$$\bar{T} = \frac{2m_g U}{3kM} = -\frac{m_g \Omega}{3kM} \quad (2.82)$$

A star's gravitational energy can be written as $\Omega = -\alpha GM^2/R$ where α is a constant of how the mass is distributed in the star. As such from Eq. 2.25 gives

$$\bar{T} = \frac{\alpha m_g GM}{3kR} \quad (2.83)$$

Fundamentally stars heat up as they contract, and cool as they expand. Rewriting Eq. 2.83, with the radius as the function of average density, $\bar{\rho} = 3M/4\pi R^3$, to give

$$\bar{T} = \frac{\alpha}{3} \frac{m_g G}{k} \left(\frac{4\pi}{3} \right)^{1/3} M^{2/3} \bar{\rho}^{-1/3} \quad (2.84)$$

2.7 Luminosity

The luminosity of the star is determined by considering the energy generated by stellar material. If we consider an infinitesimal mass the defined contribution to luminosity is

$$dL = \epsilon dm \quad (2.85)$$

where ϵ is the total energy contribution per second per kilogram of mass, $\epsilon = \epsilon_{gravity} + \epsilon_{nuclear}$. The early evolution energy contribution is all gravity until deuterium burning begins. For a spherically symmetric star the mass

of a thin shell of thickness dr is

$$dr = dM_r = \rho dV = 4\pi r^2 \rho dr \quad (2.86)$$

dividing by the thickness of the shell, the luminosity is given as a differential

$$\frac{dL_r}{dr} = 4\pi r^2 \rho \epsilon \quad (2.87)$$

This gives the luminosity due to all mass within the interior of the shell that has radius r . We can also determine luminosity from temperature using the Stephan-Boltzmann law

$$L = 4\pi\sigma T^4 \quad (2.88)$$

Where σ is the Stephan-Boltzmann constant. P is the total power emitted from an object over its surface given it emits like a black-body. Assuming spherical geometry we can relate the luminosity to this power by

$$L = 4\pi R^2 \sigma T^4 \quad (2.89)$$

As such the luminosity can be determined from the temperature of the star. The luminosity of a protostar is hard to evaluate in reality, due to the molecular cloud surrounding the star being optically thick, blocking the majority of radiation escaping. The luminosity of a star has complications in evaluating as the radiation is absorbed by its surrounding cloud. However, this radiation is emitted eventually but at longer wavelengths, as such the bolometric luminosity will be the same but the distribution of wavelengths will be shifted toward the lower end.

2.8 Energy Transport Mechanisms

The three standard energy transport mechanisms, radiation convection and conduction are all present in stars. The impact of radiation and conduction is dependent on the mean free path of photons, $10^{-2}m$, and particles $10^{-10}m$, respectively. As such the conductive transport mechanism is many orders of magnitude slower than radiation and thus, mostly insignificant to

the total energy movement. Both radiation and convective mechanisms will be outlined here.

Radiation transfers energy from gravitation and nuclear reactions via photons. The photons are emitted, absorbed and re-emitted in almost random directions. This radiation travel is clearly conditional to the opacity of the material. If we consider a radiation pressure gradient

$$\frac{dP_{rad}}{dr} = -\frac{\bar{\kappa}\rho}{c}\mathcal{F} \quad (2.90)$$

Where $\bar{\kappa}$ is the average opacity of the material. \mathcal{F} is total radiative flux through the material. We can also describe the radiation pressure as

$$\frac{dP_{rad}}{dr} = \frac{4}{3}aT^3\frac{dT}{dr} \quad (2.91)$$

equating the two

$$\frac{dT}{dr} = \frac{-3\bar{\kappa}\rho}{4acT^3}\mathcal{F} \quad (2.92)$$

substituting the force due to radiation with the luminosity relation

$$\mathcal{F} = \frac{L_r}{4\pi r^2} \quad (2.93)$$

The result for radiation transport is

$$\frac{dT}{dr} = -\frac{3}{4ac}\frac{\bar{\kappa}\rho}{T^3}\frac{L_r}{4\pi r^2} \quad (2.94)$$

The convection of matter is due to the more energetic buoyant mass moving towards the surface of the star and the cooler mass sinking to the centre. We can describe the rising mass as an adiabatically moving bubble which, after travelling a distance, will then give up its energy to the surroundings by dissolving into it. We can describe this bubble first by differentiating the ideal gas equation 2.49

$$\frac{dP}{dr} = -\frac{P}{\mu}\frac{d\mu}{dr} + \frac{P}{\rho}\frac{d\rho}{dr} + \frac{P}{T}\frac{dT}{dr} \quad (2.95)$$

Using the relation of $V \equiv 1/\rho$, the adiabatic relation between pressure and density is

$$P = K\rho^\gamma \quad (2.96)$$

differentiating with respect to the radial distance

$$\frac{dP}{dr} = \gamma \frac{P}{\rho} \frac{d\rho}{dr} \quad (2.97)$$

If we assume that μ is a constant, then eqs. 2.95 and 2.97 can be combined to give the adiabatic temperature gradient.

$$\left. \frac{dT}{dr} \right|_{ad} = - \left(1 - \frac{1}{\gamma} \right) \frac{\mu m_H}{k} \frac{GM_r}{r^2} \quad (2.98)$$

2.9 Stellar Equations

We have now derived the principle mechanisms and the associated equations that describe stellar evolution. These methods can be used throughout the entire evolution from cloud, through to main sequence, to end-of-life. These equations cannot be solved analytically and need adjustment for numerical modelling. By replacing differentials with difference equations, this places numerical limits to the equations allowing them to be evaluated completely. In most numerical simulations, these limits would be implemented by incremental radial distances allowing evaluation of pressure, temperature, luminosity, and mass across these spherical shells. However the model in this research has similar principles but uses grid based limits, as will be outlined later.

2.10 Boundary Conditions

At the centre of stars, where $M_r = 0$ and where $L_r = 0$, singularities will develop when using the equations previously defined. As such, the usual solution is to expand a first order taylor series with the boundary condition at a small value of M_r near the centre, where

$$r = \left(\frac{3}{4\pi\rho_c} \right)^{1/3} M_r^{1/3} \quad (2.99)$$

$$P = P_c - \frac{1}{2} \left(\frac{4\pi}{3} \right)^{1/3} G \rho_c^{4/3} M_r^{2/3} \quad (2.100)$$

$$L_r = \left(E_{nuc} - \frac{d\epsilon}{dt} - P \frac{dV}{dt} \right)_c M_r \quad (2.101)$$

$$T = T_c - \frac{1}{2} \left(\frac{4\pi}{3} \right)^{1/3} G \left(\frac{\rho_c^{4/3}}{P_c} \cdot \nabla_c \cdot T_c \cdot M_r^{2/3} \right) \quad (2.102)$$

The temperature gradient is set dependent upon if the layer is radiative or convective (figure 1.1). The Luminosity Mass function goes to a constant but must be evaluated off centre. Density, temperature and pressure are all calculated.

Using 2.89 the boundary condition for the surface of the star can be determined. Where in this case the luminosity would be the value from the surface and R is the radius to the surface. If we assume a fixed gravitational acceleration, the atmospheric hydrostatic equilibrium can be found

$$\frac{dP}{dr} = - \frac{GM_r\rho}{r^2} = -g\rho \quad (2.103)$$

with the optical depth being defined $d\tau = -\kappa_R \rho dr$ and assuming $M = M_r$ in the atmosphere

$$\frac{dP}{dr} = \frac{g}{\kappa_R} \frac{d\tau}{dr} \quad (2.104)$$

By integrating between the limits of τ being small at the surface inwards to a value of 2/3 (Carroll B.W., 1996), obtained from the Eddington approximation, to define the photosphere as

$$\kappa_{ph} P_{ph} = \frac{2}{3} g \quad (2.105)$$

As such the end equation is an approximation for the two boundary conditions of the surface of the star. More detailed models of the atmospheric composition are desired to be able to make better comparisons with observation. The hydrogen and helium elements tend to have different levels of ionisation, dependent on their location within the star. Inner layer hydrogen and helium is mostly fully ionised, whereas outer layers have only partial ionisation.

2.11 The Model

We use the provided program, STELLAR, that comes alongside the textbook of Bodenheimer et al. (2006) with some adaptations. The STELLAR package is a hydrodynamic adaptive grid code that solves the stellar structure via the Henyey method.

The Henyey method solves implicitly, and simultaneously, the outlined equations at time, $t^{n+1} = t^n + \Delta t$, where n is an integer of the current time step. This has the requirement for a initial resolved function at t^n . As with other interpolation techniques, once resolved the found values are used to update the model variables including the composition χ , which will then be used in the next iterative step. STELLAR used a grid of mesh points, J , with $j = 1$ and $j = J$ as the centre of the star and surface of the star respectively (figure 2.3). The surface also has defined $M_j = 0$, where $M_j = M$ where M is total mass. Incremental masses, $dM_j = M_j - M_{j-1}$ must be stored to avoid the subtraction of nearly equal quantities between grid points. The code will adapt the grid mesh to increase or decrease the numbers of mesh points for regions of rapid change, this is set up so the difference between M_j and M_{j+1} is no more than 3 – 4%. As a star develops, the pressure difference between the centre and the surface will increase greatly, as such the number of zones will need to be increased as t increases. The three principle equations previously outlined, Eq. 2.21, Eq. 2.23, Eq. 2.101 and the diffusion approximation for all types of energy transport

$$\frac{dT}{dM_r} = -\frac{GM_r T}{4\pi r^4 P} \nabla \quad (2.106)$$

The radius r_j and the luminosity L_r are defined on the edges of the grid points, M_j . The pressure, density and temperature P_j, ρ_j, T_j are all defined as halfway between grid points such that the mass co-ordinate for them is $M_{j-1/2}$. As such the equations used in the code are redefined as

$$P_{j+1} - P_j + \frac{(M_{j+1/2} - M_{j-1/2})GM_j}{4\pi r_j^4} = 0 \quad (2.107)$$

$$r_j^3 - r_{j-1}^3 - (M_j - M_{j-1}) \cdot \frac{3}{4\pi \rho_j} = 0 \quad (2.108)$$

$$L_j - L_{j-1} - (M_j - M_{j-1}) \left[E_{nuc,j} - \frac{c_{P,j}(T_j - T_j^n)}{\Delta t} + \frac{\delta}{\rho_j} \frac{(P_j - P_j^n)}{\Delta t} \right] = 0 \quad (2.109)$$

$$T_{j+1} - T_j + \frac{(M_{j+1/2} - M_{j-1/2})GM_j}{4\pi r_j^4} \frac{B_{j+1} + B_j}{2} = 0 \quad (2.110)$$

Where $B = T_j \nabla_j / P_j$.

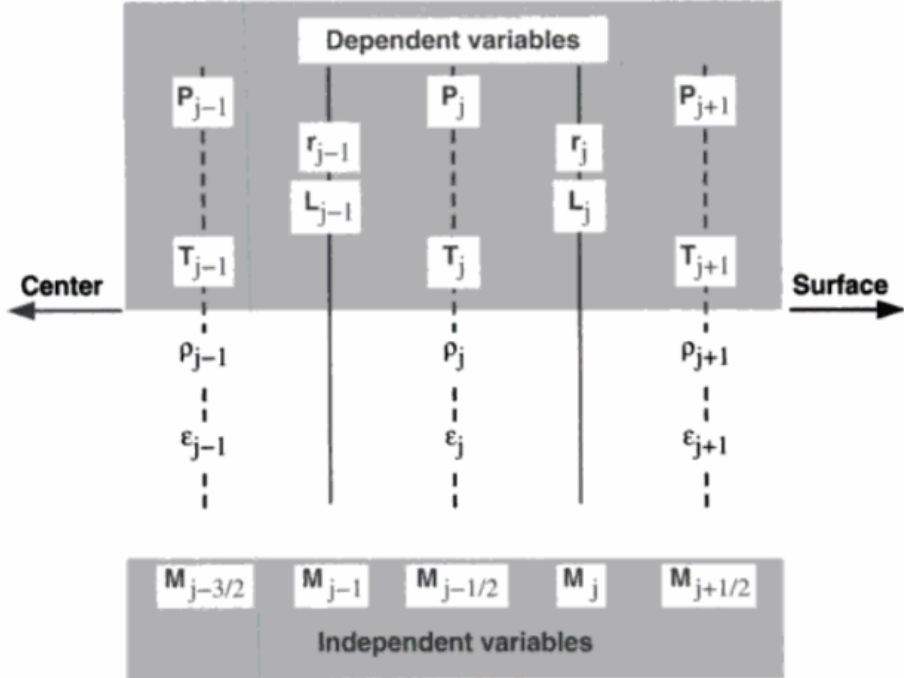


FIGURE 2.3: The grid setup of the STELLAR as shown in Bodenheimer et al. (2006), the variables of density, nuclear energy, opacity and, total energy ($\rho, E_{nuc}, \kappa, \epsilon$ respectively) are all found as functions of the variables shown at the top of the grid. M_r is the lagrangian co-ordinate, with pressure, radius, temperature and, luminosity being the four dependent variables (P, r, T, L , respectively).

STELLAR requires initial values for variables at t^n point, as such a converged model of a protostellar core of approximately 50 jupiter masses, $0.05M_\odot$, luminosity of $2.2 \times 10^{-2}L_\odot$ and radius $0.56R_\odot$ was used at the centre of the grid.

The STELLAR code has been further developed to use an input file that externally defines mass accretion rate, time step and total time. Minor adjustment to the internal time step of STELLAR was made to scale. The early stages, and through the main accretion phase, require greater accuracy, and thus a smaller internal time step, by adding a multiplicative factor of the current time to the fixed time step. This has small impact in early stages

but increases the time step later which reduces the total run time.

$$\text{DTMIN} = 1.0 \times 10^4 + (1.0 \times 10^{-5} \times \text{TIMOD}) \quad (2.111)$$

Where DTMIN is the minimum timestep and TIMOD is the internal current time of the program. This proved effective in reducing program run time with a change from ≈ 150 hours to $\approx 6 - 24$ hours. We made small additions to a makefile in order to reset certain files to an original state. These files are altered when the program is run, which if reused will cause program to fail. The solution was to include a copy function that overwrites the altered file with the original, each time the program is compiled.

The main body of code has been designed to read in variables from a variety of input files. These variables allow control over internal functions, an example being the time step limits for the Henyey method. Assigning the variables in external files makes for a much simpler process in controlling how the program performs. We focused on developing one of these external files, 'dummymain.f'. This file controls multiple fundamental variables, namely the mass flux and time frame of formation. We aimed to modify this file to specify variable or constant accretion models, with options to choose final mass and then inclusion of episodic bursts.

2.12 Pre Main Sequence Phases

GMCs contain large quantities of mass, on the order of millions of solar masses. These GMC's will either expand, or collapse, depending on the Jeans instability criteria shown in Eq. 2.3. A collapsing cloud is decreasing in volume and, as such, increasing its density. This increase allows for fragmentation to take place. Fragmentation is a series of localised collapsing envelopes within the GMC. This fragmentation process will lead to the generation of multiple protostellar cores. We focus on the processes after this fragmentation has taken place, by looking at one protostellar core and its encapsulating envelope.

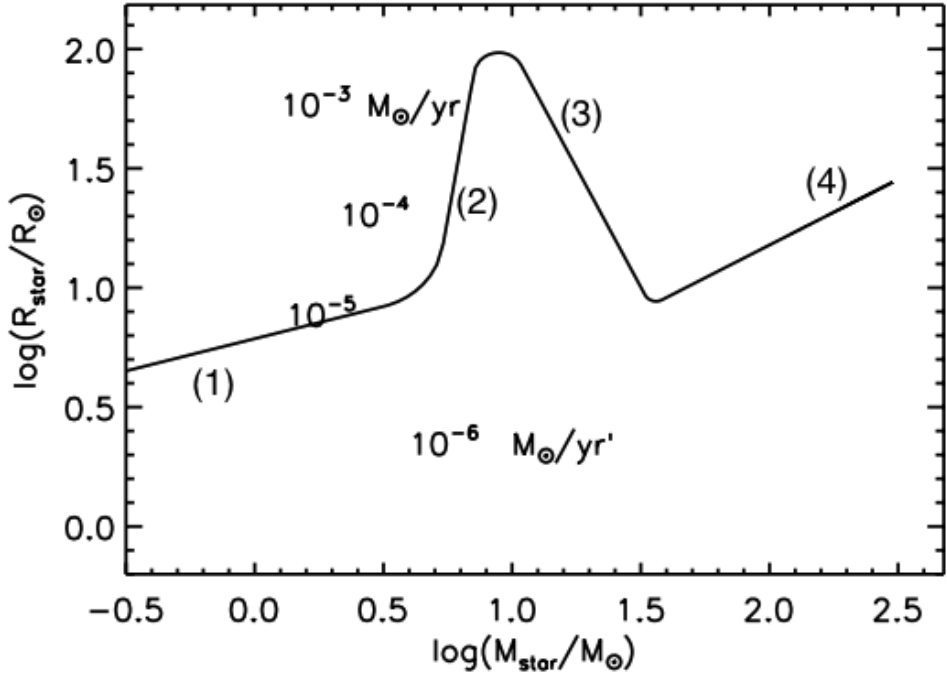


FIGURE 2.4: The evolutionary track for radius as a function of stellar mass, as found by the code used in Smith (2014). The figure shows an extreme example of the pre main sequence phases using a star with a final mass of $300M_{\odot}$. Labels on the figure, 1, 2, 3 and, 4 indicate the adiabatic accretion, swelling, KH contraction and main sequence transition phases, respectively.

2.12.1 Adiabatic Accretion

The central protostellar core will accrete mass from its surrounding envelope as it continues to collapse. This process of collapse leads to the increase of local density which corresponds to an increase in opacity. At some critical point during this stage, the opacity will have increased to a point where all the internal energy converted from potential energy will be absorbed and contained within the star itself. Since the energy is not lost from the system, we call this adiabatic collapse. The accretion of matter in this stage directly corresponds to an increase in temperature.

2.12.2 Swelling

The protostar will go through a swelling (interchangeably called bloating) phase if it reaches, or exceeds, an accretion rate of $\dot{M} \sim 10^{-5} M_{\odot}/\text{yr}$, as shown by Palla & Stahler (1990 & 1991). This process will happen before reaching the zero age main sequence. The swelling occurs due to

the internal temperatures of $\sim 10^6 K$ which initialises deuterium burning in the shell. This deuterium burning stage is crucial; stars more massive than $\sim 3M_\odot$ would not exist without the deuterium burning. The burning initiates convection within the core, thus regulating internal temperature to keep below the hydrogen fusion temperature which allows the star to continue accreting mass. A scenario where the accretion exceeds $\dot{M} \sim 10^{-3} M_\odot/yr$ however, will go through the swelling phase regardless to the effect of deuterium burning. This swelling occurs due to the entropy contained in the deep centre of the star rapidly moving toward the outer shells and surface.

2.12.3 Kelvin-Helmholtz Contraction

The previous swelling phase will contribute to a decrease in opacity, the reversed method of reaching the adiabatic phase, as such the pre-main-sequence star becomes much more luminous allowing the energy from within to be radiated away. The Kelvin-Helmholtz timescale is given by

$$t_{kh} = \frac{\text{Total Energy}}{\text{Rate of energy Loss}} = \frac{GM^2}{RL} \quad (2.112)$$

Where; G is the gravitational constant, M is the mass of the star, R is the radius of the star, and L is the luminosity of the star. A critical point will be reached whereby the timescale for radiating energy away, t_{KH} , will be shorter than the accretion timescale, t_{acc} , allowing the total energy and therefore temperature to decrease. To maintain virial equilibrium, the star will contract. This contraction increases internal core temperature will lead to the eventual 'ignition' of the star, however this is not immediate and can take a significant time to happen, on the order of 10^5 to $10^7 yr$.

2.12.4 Main Sequence Transition

The transition from contraction to main sequence is a mass dependent time frame, massive stars will take somewhere in the same order as accretion time of $1 - 10 \times 10^5 yrs$, whereas low mass stars can take on the order of $10^6 - 10^8 yrs$. Over this time the temperature increases within the stellar core to a value $\geq 10^7 K$ where it is now high enough that hydrogen fusion

can take place. This is the point at which we now define the protostellar core as a zero age main sequence star.

Chapter 3

Method

We aim to find a connection between the results of our variable accretion rate model to previous work and observational data, with the eventual desire of being able to accurately produce a fully comprehensive stellar evolution for stars of all masses. A key step is determining a complete accretion method that holds true for all star formation within GMCs. Eventually equipping a three dimensional magneto-hydrodynamic code with a conclusive accretion model will lead to better understanding of star formation from cloud to main sequence.

Using the STELLAR code, provided by Bodenheimer et al. (2006), we build on the ideas developed in Smith (2014), aiming to produce more detailed tracks involving relations between mass, time, radius, temperature and luminosity. We also aim to model short episodic accretion bursts in line with the recent results from Hosokawa et al. (2016).

An interface to the STELLAR evolution code allowed the accretion models and the main and minimum phase's timescales to be defined externally. The accretion methods from Smith (2014), were coded into the input file which then evaluates the accretion rate for each time step before being passed into the main STELLAR evolution program.

3.1 Accretion

We explore four debated methods of protostellar accretion rates; constant (Shu, 1977), accelerated (McKee & Tan, 2003), a power law (Calvet et al., 2000), and an exponential (Myers et al., 1998). We split the process into two defined stages of accretion; an initial main accretion phase set as the first $t_{acc} = 1 \times 10^5$ year period, this transitions into a minimum accretion

period of 9×10^5 years, which we call the "clean up" phase where accretion rate is set to a minimum value of $\approx 10^{-7} M_{\odot}$. The clean up accretion stage is crucial to allow time for the star to fully evolve. The incorporated minimum accretion rate keeps the program from collapsing early and from breaking boundary conditions, but the nominal accretion rate has small impact on the end result. This "clean up" accretion rate adds another $\approx 1 - 2\%$ of the mass at the end of the first stage.

In the case of the power law and exponential, the accretion rate continues to drop throughout the entire run, unless dropping below a $10^{-8} \frac{M_{\odot}}{\text{yr}}$ threshold rate, if passing this rate the program will fix it at the threshold rate until finishing all iterations. We still define it as the main accretion phase, because 75% – 85% of the final mass is reached in the 10^5 yr time frame.

The total time for the evolution is $t_t = 10^6$ years, which we set the program to divide into 3×10^4 iterations at $1.052 \times 10^9 \text{ s} = 33.3$ years each.

For simplicity the accretion rate is calculated from a pre-defined value for the desired final mass of the star, allowing just one integer variable to be changed to achieve this. The calculations for accretion rate will be outlined further, but note we include an efficiency factor of 0.7 as we assume a 30% loss of mass in jets from the protostar, Shu et al. (1994).

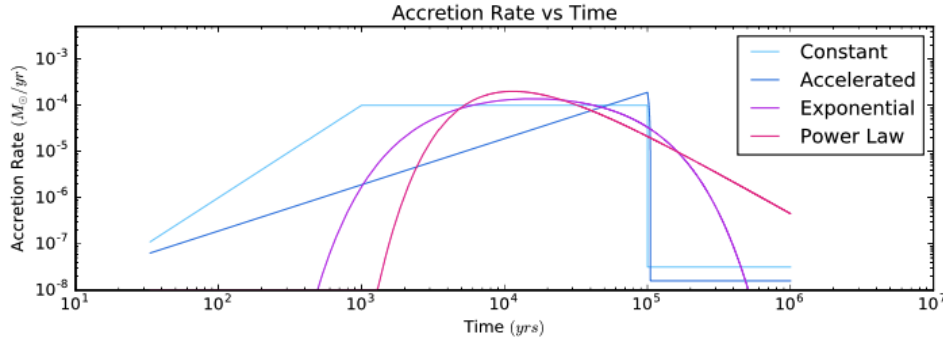


FIGURE 3.1: The four different modelled accretion rates plotted as a function time for a star of $10M_{\odot}$.

Shown in Figure 3.1 is the smooth accretion process for each method in which a $10M_{\odot}$ star was produced. Note the initial gradual increase to reach the main accretion phase rate for the constant method, used for stability. The clean up phase minimal accretion rates can be seen implemented after the $t = 10^5 \text{ yr}$ point by the sharp drop to the minimum accretion rate. Note

the differences between the exponential and power law accretion methods; the exponential rapidly increases in rate earlier but not peaking as high. The power law rate begins to drop off sooner after reaching its peak but levels off the declining rate, whereas the exponential does not.

3.1.1 Constant

The constant accretion rate is a simple fixed rate generally used in isothermal sphere models, originating from Shu (1977). Differing from Shu (1977), our model has a finite limit of molecular gas. As such, we model an accretion rate that holds steady until the end of the main accretion time, where we assume the rate drops to a minimum as the molecular cloud resources are exhausted. The initial rate is determined by the total mass of the envelope and the speed of sound in the envelope.

The constant accretion rate coded is defined by the final mass desired

$$\dot{M}_{const} = \frac{M_f}{t_{acc}} \quad (3.1)$$

Where M_f is the final mass and t_{acc} is the time of the main accretion phase. We also include an efficiency of accretion later, due to the losses from jets and outflows. The program is susceptible to failure if large rapid changes occur, such as the first iteration. To minimise this effect a small 1000 year stage at the beginning of the program is used, where the accretion is gradually increased to match the main accretion rate as defined by Eq. 3.1 and seen in Figure 3.1.

3.1.2 Accelerated

An accelerated accretion is generally used for low to intermediate mass stars as it aids in solving the luminosity problem of protostellar cores (Offner & McKee (2011)). Determined by the increase in mass flux as a function of time, followed by a steep drop off as the envelope's resources are depleted.

McKee & Tan (2003) has postulated a turbulent core model using a typical core density, $\rho \propto r^{3/2}$ results in accretions rates as a function of time,

with timescales of $\approx 10^5 \text{ yr}$.

$$\dot{M}_* \propto t \quad (3.2)$$

The definition coded for this accretion model is given using an initial accretion rate

$$\dot{M}_0 = \frac{M_\odot}{a} \times M_f \times \frac{2.857}{t_{acc}} \quad (3.3)$$

Where $\frac{M_\odot}{a}$ is in units of solar masses per year. M_f is the final mass of the star given in solar masses. t_{acc} is the time of the main accretion phase in years. The factor of 2.857 is for inclusion of mass losses at 70% efficiency. As such the total mass accreted is given by:

$$\sum_{t=0}^{100,000} \dot{M}_t = M_0 \times t \times \frac{t_t}{t_{acc}} \quad (3.4)$$

Where t is the time. t_t is the total time ($1 \times 10^6 \text{ yrs}$).

3.1.3 Exponential

An exponential accretion model (Myers et al. (1998)), is the optimal adaptation of an accretion where infall is similar to the constant rate used with isothermal spheres but followed by a declining rate. This is given by

$$\dot{M}(t) = \frac{M_0}{t_f} e^{-t/\tau_f} \quad (3.5)$$

This rate is proportional to the mass loss rate of the envelope, but going further to model a rising period rather than starting at a high rate.

$$\dot{M}(t) = \dot{M}_0 e^{(2\tau_r/\tau_f)^{1/2}} e^{-\tau_r/\tau_f} e^{-t/\tau_f} \quad (3.6)$$

Where $\tau_f = t_{acc}/t_t$ and $\tau_r = \tau_f/10$. This generates the maximum accretion rate at time, $t_m = \sqrt{\tau_r \tau_f}$. For our model this peak time occurs at $t_m \approx 1.58 \times 10^4 \text{ yrs}$.

3.1.4 Power Law

Calvet et al. (1999), shows strong observation support for an accretion with strong decay phase. As such we incorporate a power law drop off model as an accretion rate. Power law accretion is generally the preferred method for low-intermediate mass stars (Smith et al. (2000)).

The power law accretion rate is given as:

$$\dot{M}_{power} = \dot{M}_0 \left(\frac{e}{\alpha}\right)^\alpha \left(\frac{t}{t_{acc}}\right)^{-\alpha} e^{-t_{acc}/t} \quad (3.7)$$

Where α is a constant that corresponds to the accretion rate curvature. 0.5 being a gradual accretion and 2-3 being an abrupt accretion. The power law and exponential models are similar but there are important differences. The peak accretion rate in a power law model occurs early in the accretion phase after a sharp initial increase in rate (figure 3.1). The power law has a sharp increase in the accretion rate, \ddot{M} , as such it manages to reach its peak accretion rate earlier than the other variable models. The power law also has a greater peak accretion rate value than the other models.

3.1.5 Accretion Bursts

We attempt to model episodic accretion shocks, which we refer to as "bursts" from here on in. It is shown that the majority of mass accreted does not come in the form of a steady progression, but instead in massive accretion shocks of high intensity over a short time period. It has been shown that bursts are key to the fragmentation within the accretion disk, which aids the formation of multiple star systems and planetary objects(Stamatellos et al. (2011)). The bursts are modelled to accrete 90% of the final stellar mass through the short $\approx 10^3$ yrs burst phases with the final 10% accumulating in the 'off' state lasting 9×10^3 yrs.

To couple the modelled accretion methods and a burst counter part, we pass the original calculation of accretion through a secondary modulo function which determines if the accretion will be in an on or off state. The modulo functions used to determine accretion state are coded as such

$$\text{IF} \left(\frac{i}{30} \bmod 10 \right) \neq 9 \text{ THEN } \dot{M} = \dot{M}_{min} \quad (3.8)$$

and

$$\text{IF}\left(\frac{i}{30} \bmod 10\right) = 9 \text{ THEN } \dot{M} = \dot{M}_{max} \quad (3.9)$$

where i is the current iteration of the program, and where:

$$M_{min} = \dot{M} \times 0.111 \quad (3.10)$$

and,

$$M_{max} = \dot{M} \times 9.099 \quad (3.11)$$

Where \dot{M} has already been calculated for its respective accretion method at that time point.

3.1.6 Input File

We make adjustments to an input file which calls the main STELCOR code. This file was originally put together by H.W. Yorke and is used in Kuiper & Yorke (2013). We made major alterations to the file to include the accretion models outlined, and other front end adjustments. For simplified use, we include a series of requests informing the user to specify final mass, accretion time and which accretion model to use. Having all the models contained in one file, and then being able to adjust the variables once executed greatly reduces program run time.

```

1 C This is a dummy "hydro" code that calls STELCOR
2 C AUTHOR: H.W. YORKE 12-FEB-11 (JPL / CALTECH)
3 C Updated: D. HASTIE, M.D. SMITH, 1-MAY-16 (SPS, University
      of Kent)
4     include 'parm.h'
5 C Variables not included elsewhere are defined here.
6     double precision :: deetee,tpeak
7     double precision :: mdotzero,mdotstar,epsilon
8     double precision :: tnaught,tostar
9     double precision :: rateunit,fluxmin,fluxold
10    double precision :: decel,decelr
11    double precision :: initialrate,finalmass,fsolmass
12    double precision :: numru,solmass,yearins,acciters
13    double precision :: mdotstarramped,divpart
14    double precision :: taur,tauf,taueee
15    integer :: accmethod

```

```

16 C Starting values for the external mass and time.
17     CorM = 9.94373E31
18     TIME = 0.
19 C "hydro" time step (independent of STELCOR's internal time step)
20     DTIME = 1.052e9
21     solmass = 1.989d33
22     yearins = 3.1557d07
23     rateunit = solmass/yearins
24 C Terminal prompts to read user desired values.
25 C If this is to be run on a node, comment out the following
     section
26 C and go to the section underneath where you can manually enter
     values.
27 C Desired final mass
28     print*, "Enter the final desired mass in solar masses."
29     read*, fsolmass
30 C The following allows the user to choose how many iterations
31 C and therefore time period of accretion phase.
32 C This section has yet to be coded into power and accelerated
     methods
33     print*, "Enter the number of iterations of main accretion
     phase"
34     print*, "(between 1000–30000)"
35     read(*,*) acciters
36 C Section for choosing the accretion method.
37     print*, "Enter an accretion method."
38     print*, "Constant = 1, Power Law = 2, Accelerated = 3,
     Exponential = 4"
39     read(*,*) accmethod
40 C C Manual section.
41 C     fsolmass = 100
42 C C Changing acciters will adjust tostar value.
43 C     acciters = 3000
44 C     accmethod =4
45     finalmass = fsolmass*1.989d33
46 CCCCCCCCCCCCCCCCCCCCCCCCCCCCCCCCCCCCCCCCCCCCCCCCCCCCCCCCCCCCC
47 C     Beginning of the Constant section.          C
48 CCCCCCCCCCCCCCCCCCCCCCCCCCCCCCCCCCCCCCCCCCCCCCCCCCCCCCCCCCCCC
49     if (accmethod .EQ. 1) then
50 C Epsilon is the efficiency factor (Mass loss to jets)
51         epsilon = 0.3
52 C Total time scale

```

```

53      tnaught = 1.0d06
54 C Time scale of accretion phase
55      tostar = (tnaught/30000)*acciters
56 C Efficiency applied to accretion
57      divpart = tostar * (1-epsilon)
58 C The accretion factor.
59      initialrate = fsolmass / divpart
60 C Putting accretion factor into cgs units
61      mdotzero = initialrate * rateunit
62 C Accretion with the efficiency included
63      mdotstar = mdotzero * (1-epsilon)
64 C Reduced accretion for initial stages
65      mdotstarramped = mdotstar/900
66      iprint= 1
67 C The accretion rates of high and low states for bursts.
68      fluxM1= 0.1 * mdotstar
69      fluxM2= 9 * mdotstar
70      fluxold=fluxM2
71      do i=1,30000
72 C The following if loop specifies the accretion rate.
73      if(i.LE.31 .AND. i.LE.acciters)then
74 C The accretion rate increases proportional to
75 C the iteration number squared
76      fluxM = mdotstarramped * (i**2)
77      else if(i .LE. acciters) then
78 C Burst selection of high/low state
79      if(mod(i / 3,10).eq.9)then
80          fluxM = 0.1 * mdotstar
81      else
82          fluxM= 9.0 * mdotstar
83      endif
84      else
85 C Low accretion rate for trickle phase
86          fluxM= rateunit * 1.0d-08
87      endif
88      iprint= 1
89 C Update time and mass in the calling program.
90      TIME=TIME+DTIME
91      CorM=CorM+DTIME*0.5*(fluxM+fluxold)
92      call stelcor(CorM,CorR,CorL,fluxM,TIME,iprint)
93 C Stellar radius CorR and intrinsic luminosity CorL are determined
     by stellar

```

```

94 C evolution calculations in STELCOR. For the total luminosity ,
   add the intrinsic
95 C luminosity to the accretion luminosity .
96         accL = 0.75 * 6.6832d-8 * CorM * fluxM / CorR
97         fluxold=fluxM
98 C Variables to write to data file
99         write(6,201) i ,TIME,DTIME,CorM,CorR,CorL,accL+CorL,fluxM
100        enddo
101        stop
102 CCCCCCCCCCCCCCCCCCCCCCCCCCCCCCCCCCCCCCCCCCCCCCCCCCCCCCCCCCCCCCCCC
103 C      This is the end of the Constant section .      C
104 CCCCCCCCCCCCCCCCCCCCCCCCCCCCCCCCCCCCCCCCCCCCCCCCCCCCCCCCCCCCCCCCC
105 C This is the beggining of the PowerLaw section . C
106 CCCCCCCCCCCCCCCCCCCCCCCCCCCCCCCCCCCCCCCCCCCCCCCCCCCCCCCCCCCCCCCCC
107        elseif (accmethod .EQ. 2) then
108          alpha = 1.75
109          acon    = (exp(1.0)/alpha)**alpha
110          deetee = 1.0/3.0d04
111          tnaught = 1.0d06
112          tostar = 2.0d04
113          mdotzero = rateunit * 2.86143d-05 * fsolmass
114          epsilon = 0.3
115          mdotstar = mdotzero * (1.0 - epsilon)
116          fluxmin = rateunit*1.0d-08
117          fluxold = rateunit*1.0d-07
118          do i=1,30000
119            tpeak = real(i)*deetee*tnaught/tostar
120            teeaye = tpeak**(-alpha)
121            fluxM = mdotstar *acon*teeaye* exp(-1.0/tpeak)
122            if (fluxM .le. fluxmin) fluxM=fluxmin
123            iprint= 1
124            TIME=TIME+DTIME
125            CorM=CorM+DTIME*0.5*(fluxM+fluxold)
126            call stelcor(CorM,CorR,CorL,fluxM,TIME,iprint)
127 C Stellar radius CorR and intrinsic luminosity CorL are determined
   by stellar
128 C evolution calculations in STELCOR. For the total luminosity ,
   add the intrinsic
129 C luminosity to the accretion luminosity .
130         accL = 0.75 * 6.6832d-8 * CorM * fluxM / CorR
131         fluxold=fluxM
132         write(6,201) i ,TIME,DTIME,CorM,CorR,CorL,accL+CorL,fluxM

```

```

133      enddo
134      stop
135 CCCCCCCCCCCCCCCCCCCCCCCCCCCCCCCCCCCCCCCCCCCCCCCCCCCCCCCCCCCCCCCCCCCCC
136 C      End of the PowerLaw section.          C
137 CCCCCCCCCCCCCCCCCCCCCCCCCCCCCCCCCCCCCCCCCCCCCCCCCCCCCCCCCCCCCCCCCCCCC
138 C      Beginning of the Accelerated section.    C
139 CCCCCCCCCCCCCCCCCCCCCCCCCCCCCCCCCCCCCCCCCCCCCCCCCCCCCCCCCCCCCCCCCCCCC
140      elseif (accmethod .EQ. 3) then
141          deetee = 1.0/3.0d04
142          tnaught = 1.0d06
143          tostar = (tnaught/30000)*acciters
144          epsilon = 0.3
145          decel = 1.0
146          decelr=0.0
147          initialrate = rateunit*fsolmass*2/tostar
148          print*, initialrate
149          print*,tostar
150          mdotstar = initialrate * (1. - epsilon)
151          fluxmin = rateunit*1.0d-08
152          fluxold = rateunit*1.0d-07
153 do i=1,30000
154     tpeak     = real(i)*deetee*tnaught/tostar
155     fluxM    = mdotstar*tpeak
156     if (tpeak .gt. 1.0) fluxM = decelr*mdotstar*(decel-
157     tpeak)
158     if (tpeak .gt. decel) fluxM = 1.0d+17
159     iprint= 1
160 C Update time and mass in the calling program
161     TIME=TIME+DTIME
162     CorM=CorM+DTIME*0.5*(fluxM+fluxold)
163     call stelcor (CorM,CorR,CorL,fluxM,TIME,iprint)
164     accL = 0.75 * 6.6832d-8 * CorM * fluxM / CorR
165     fluxold=fluxM
166     write(6,201) i ,TIME,DTIME,CorM,CorR,CorL,accL+CorL,fluxM
167 enddo
168 stop
169 CCCCCCCCCCCCCCCCCCCCCCCCCCCCCCCCCCCCCCCCCCCCCCCCCCCCCCCCCCCCCCCCCCCCC
170 C      End of the Accelerated section.          C
171 C      Beginning of the Exponential section.    C
172 CCCCCCCCCCCCCCCCCCCCCCCCCCCCCCCCCCCCCCCCCCCCCCCCCCCCCCCCCCCCCCCCCCCCC
173      elseif (accmethod .EQ. 4) then

```

```

174      deetee = 1.0 / 3.0d04
175      tnaught = 1.0d06
176      tostar = 1.0d5
177      mdotzero = rateunit * 1.9804d-05 * fsolmass
178      epsilon = 0.3
179      mdotstar = mdotzero * (1.0 - epsilon)
180      tauf = 0.5*(tostar/tnaught)
181      taur = 0.1*tauf
182      taueee = exp(2.0*sqrt(taur/tauf))
183      fluxmin = rateunit*1.0d-09
184      fluxold = rateunit*1.0d-09
185      do i=1,30000
186          tpeak = real(i)*deetee
187          fluxM = mdotstar*taueee*exp(-taur/tpeak)*exp(-tpeak/tauf)
188          if (fluxM .lt. fluxmin) fluxM = fluxmin
189          iprint= 1
190          TIME=TIME+DTIME
191          CorM=CorM+DTIME*0.5*(fluxM+fluxold)
192          call stelcor(CorM,CorR,CorL,fluxM,TIME,iprint)
193          accL = 0.75 * 6.6832d-8 * CorM * fluxM / CorR
194          fluxold=fluxM
195          write(6,201) i ,TIME,DTIME,CorM,CorR,CorL,accL+CorL,fluxM
196      enddo
197      stop
198 CCCCCCCCCCCCCCCCCCCCCCCCCCCCCCCCCCCCCCCCCCCCCCCCCCCCCCCCCCCCCCCCCCCCCCCCC
199 C           End of the Exponential section.             C
200 CCCCCCCCCCCCCCCCCCCCCCCCCCCCCCCCCCCCCCCCCCCCCCCCCCCCCCCCCCCCCCCCCCCCCCCCC
201 201  format(' HYDRO OUTPUT: ',i5,1p,7d10.2)
202  else
203      Print*, "Invalid selection"
204  end if
205  end

```

The code contains all four accretion models with bursts. It can be seen that there is some deviation in the equations outlined to the ones used in the code for each model. There is limitation with the Fortran code when it comes to more complex functions, such as those found in the power law code and exponential models. An example, on lines 113 and 177, the included multiplicative factors of 2.86143×10^5 and 1.9804×10^5 are found using the 'capsule' code from Smith (2014), as we cannot include solutions to partial gamma functions and integrations with this version of Fortran.

The constant section has been fully commented to aid the user. The other three models use the same variables so are not commented and differences in the calculations can be followed by the equations outlined earlier. Not shown in the code above, but in the final `dummymain.f` file we include the choice to include the episodic bursts.

3.2 Evolutionary Tracks

3.2.1 Mass Radius

We aim to provide a detailed map of the growth of stars through the pre-main-sequence phases, providing insight into how the stellar evolution and structure effects the radius of the protostar. Radii of stars is a key observational quantity and, as such, mapping it as a function of stellar mass gives crucial understanding to the evolutionary stage a protostar is in.

3.2.2 Theoretical Hertzsprung Russell Track

Using our model and stellar equations (2.102, 2.103) outlined earlier we can map the tracks of $\log(L/L_\odot)$ against $\log(T/T_\odot)$ for the pre-main sequence stars, sometimes referred to as the theoretical Hertzsprung Russell diagram. The tracks produced are governed by the chosen time frame and the values of internal parameters such as, metallicity and opacity. These tracks aid determining the age of stars and star clusters. The Hertzsprung-Russel diagrams we use compare stellar luminosity to temperature. We obtain these tracks by taking the output data file produced by the STELLAR program and then pass it through the CAPS code used in Smith (2014) to obtain the temperature of the core, as this is not exclusively output from our STELLAR code.

3.2.3 Mass Luminosity

In recent years there has been a tendency to record luminosity as a function of the clump mass. This method is effective in showing the evolutionary stages and then the path taken to ZAMS and the final mass attained. The track can be broken down into two stages, the pre-main and

main sequence paths. A vertical line represents the growing luminosity of the embedded protostar as the mass of the system (star and molecular cloud) remains relatively constant. This growing luminosity is an evolutionary aging technique. As the star reaches main sequence the cloud is dissipated through various processes including molecular outflows. This second stage is shown by luminosity remaining relatively constant and the mass decreasing, shown by a horizontal plot. The luminosity of clump and mass of clump are found to be easily measurable with modern telescopes, as such large quantities of new data are available to overlay on the track plots to provide comparison. Through this thesis, we model and track a single star's formation however, we model the clump as if it is host to a complete cluster. Thus, in tables 5.1 and 5.2 we display clump masses between one and two orders of magnitude greater than the final mass of the star we model.

Chapter 4

Results

Which accretion model is most consistent with observational data? This question is hard to answer because of the differences between reality and the isolated single star scenario in this thesis. However, we can still try to find significant data points, such as the model that has a greatest swelling radius and/or greatest peak luminosity. By mapping these as reference points we can determine if there is correlation with observation.

We recognise that protostellar accretion can collapse, or end, at any stage if the mass supply is cut off. As such we must posit the question of the effects of rapid shutoff during a key phase of the evolution. Does the result of cutoff during the swelling or contraction phase lead to significant differences in tracks or other indicators such as spectral signature.

Whilst the model we use is more advanced than the likes of classic isothermal collapse, it is not fully inclusive of new research into star forming environments. More recent findings have shown giant molecular clouds tend to have long reaching, roughly cylindrical, arms that mass will flow along, with protostars and their clump flowing too. As such the filaments feed the clumps and the clumps feed the protostar, this dynamic process will significantly change the gravity, density and opacity of the protostellar clump. As such a higher mass star at an instantaneous point in time would be forming from a lower mass clump than our model suggests. So we must address the issue, is static spherical modelling a good enough representation of star formation?

Does a single base accretion rate apply throughout the entire protostellar evolution phase? Do protostars accrete mass using just one method, for all stages of evolution? We understand that stars form in dynamic regions,

where the current state of the protostar will give varying effects on its surroundings through the use of radiative feedback and jets, then we must also question if these effects can have a large enough impact on the envelope as to change the accretion rate. Is the space-time grid in our model large enough to encapsulate the extent of protostellar feedback?

4.0.1 Notes

An overview table of each accretion method we modelled is presented before displaying the results in graphical form. The tables help reference key values from each test and its corresponding series of graphs. The tables are condensed versions of the complete sets of data which can be found in the digital appendix.

The figures of evolutionary tracks shown in the results section give an overview of the data produced in this thesis. The range of star masses produced is across three orders of magnitude. All the tracks produced can be found in the digital appendix, whilst all are not required to understand the results, they may still be of interest.

4.1 Mass Radius

Here we compare the results from all four accretion models across a range of masses for the radius of protostar as a function of the mass. By plotting the tracks for all methods on one diagram we can easily spot significant differences between them. The final masses stated in the following tabled data are rounded to the nearest integer for ease of referencing between each model, the true masses differ by $\approx 1 - 5\%$.

Table 4.1 shows the final radius and its corresponding mass. It is evident that once a protostar has ended its accretion phase, the final radius is correlated to the final mass regardless of the accretion process. This can be seen for all results where each of the model's final radii are all within $< 5\%$ of each other. The only exception is $100M_{\odot}$ power law result of $34.32R_{\odot}$ which is $\approx 12\%$ less than the constant accretion model $38.92R_{\odot}$.

TABLE 4.1: A comparative table of final radii and final mass achieved using the respective accretion method. The masses highlighted here are a selection of relevant data points to the graphs featured.

Final Mass (M_{\odot})	Accretion Method's Final Radius (R_{\odot})			
	Accelerated	Constant	Exponential	Power Law
1	2.48	2.50	2.48	2.50
5	2.69	2.69	2.69	2.69
10	4.11	4.09	4.09	4.08
15	5.37	5.36	5.37	5.31
20	6.53	6.53	6.53	6.46
25	7.70	7.70	7.68	7.53
100	37.20	38.92	38.35	34.32

TABLE 4.2: The data table of final mass and peak radius achieved using the respective accretion method. The masses highlighted here are a selection of relevant data points to the graphs featured. Full data available in the digital appendix.

Final Mass (M_{\odot})	Accretion Method's Peak Radius (R_{\odot})			
	Accelerated	Constant	Exponential	Power Law
1	65.26	66.7	58.93	55.05
5	136.55	136.12	137.99	119.274
10	334.91	323.42	298.98	258.73
15	342.10	346.41	316.23	390.97
20	357.91	357.91	428.35	429.78
25	352.16	363.66	432.66	462.84
100	664.08	589.33	662.64	819.32

Table 4.2 shows how significantly larger the radius of the protostar is during the accretion phase is from the final radius. The stars that undergo the swelling phase exacerbate this difference.

Figure 4.1 shows the accelerated accretion sharply swelling at approximately the $5M_{\odot}$ point, much before the other methods of $9 - 10M_{\odot}$. However it can be seen that the accelerated accretion sharply swells later than the others in the lower mass scenarios, Figures 4.2, 4.3.

The transition between no swelling occurring to a full swelling phase occurs at masses between $4 - 8M_{\odot}$ as shown by Figures 4.4 - 4.6. This also correlates to a jump in peak radius over the 5 and $10M_{\odot}$ data points shown in Table 4.2. Note, the swelling phase does not begin simultaneously for each accretion method of same final mass. The swelling phase also holds up over different mass ranges; shown clearly in Figure 4.2, the power law and exponential have higher peak values but radius drops at a lower mass,

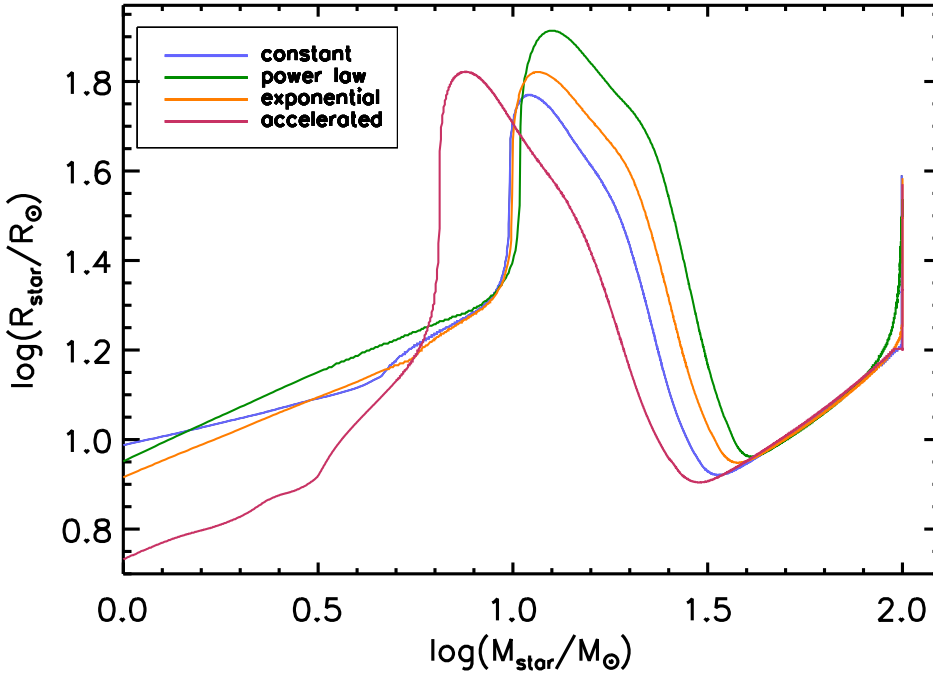


FIGURE 4.1: The radius tracks for protostars of final mass, $100M_{\odot}$. All four accretion methods are coloured accordingly as found in the legend.

whereas the drop occurs at a higher mass for the constant and accelerated models. As questioned earlier it can be seen over the range $5 - 10M_{\odot}$, the accretion phase ends during the Kelvin-Helmholtz contraction phase, resulting in a drop in radius until the program ends. The higher mass stars continue to accrete mass during and after the contraction resulting in the star partially gaining back the radius lost, figures 4.2 & 4.1.

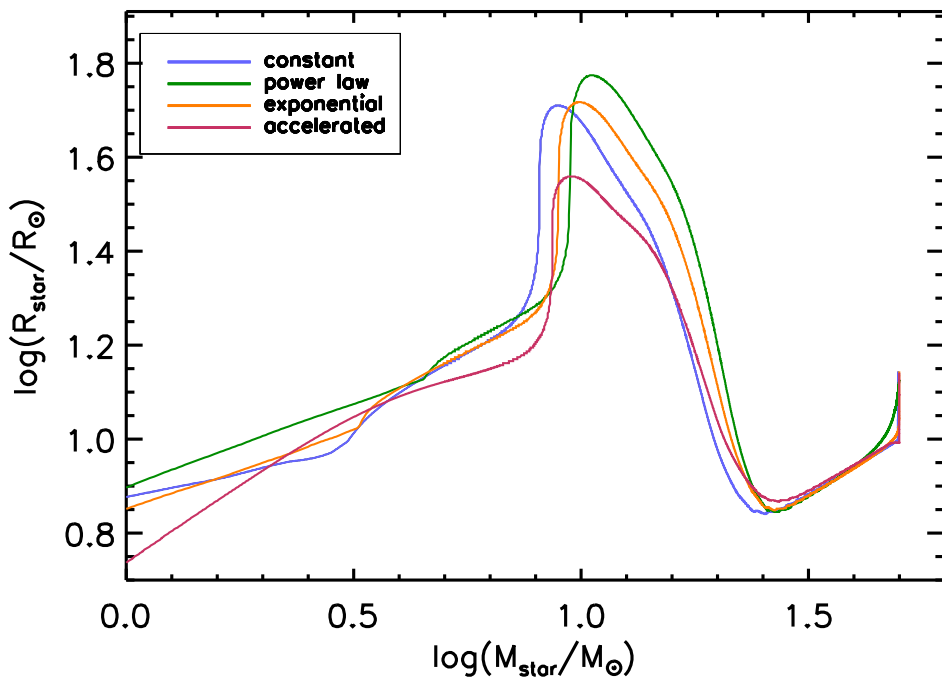


FIGURE 4.2: The radius tracks for protostars of final mass, $50M_{\odot}$. All four accretion methods are coloured accordingly as found in the legend.

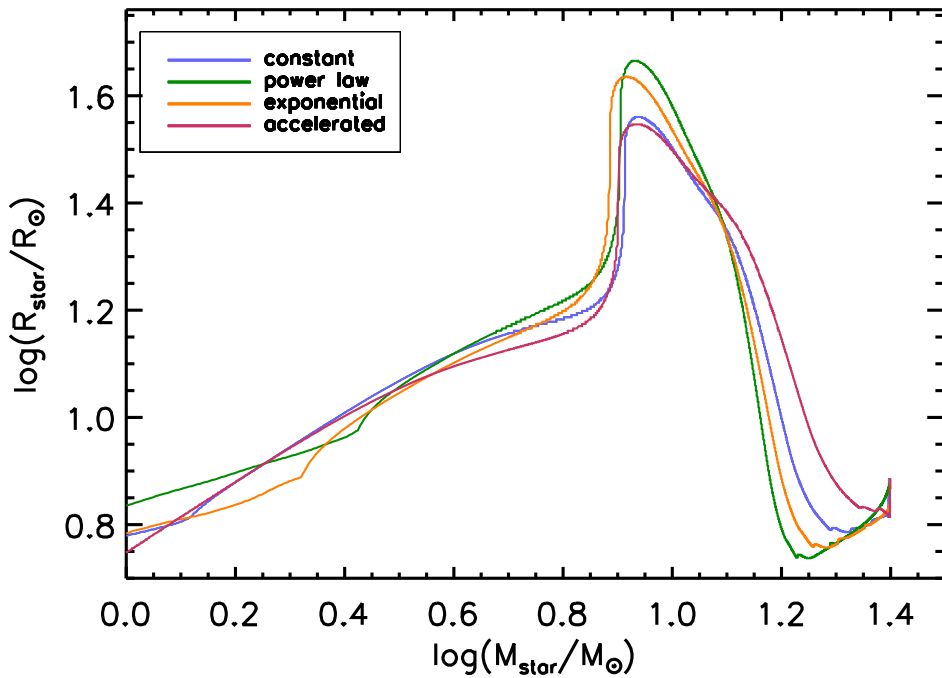


FIGURE 4.3: The radius tracks for protostars of final mass, $25M_{\odot}$.

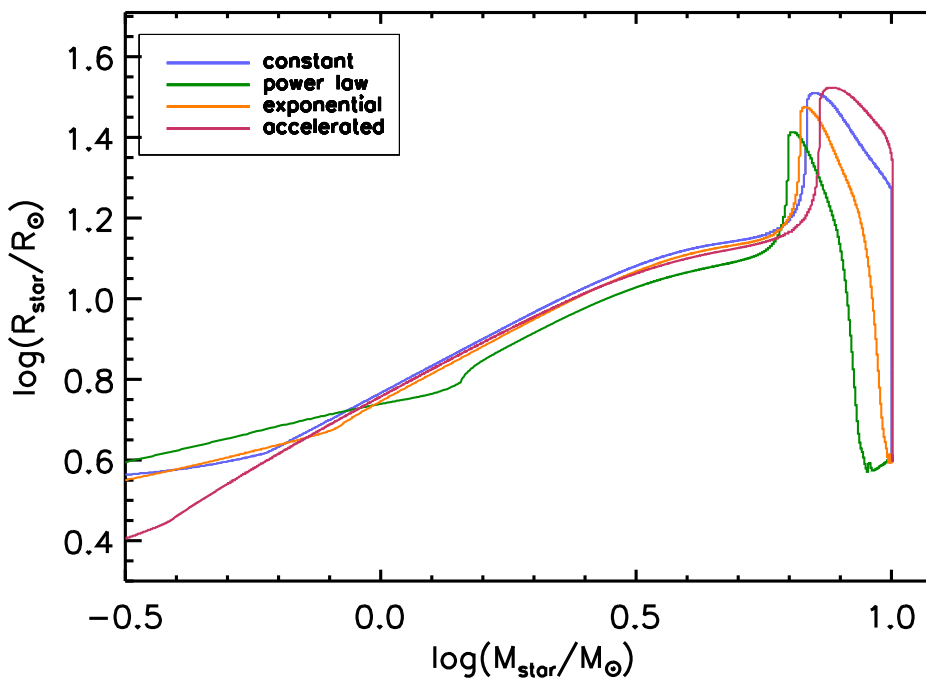


FIGURE 4.4: The radius tracks for protostars of final mass,
 $10M_{\odot}$.

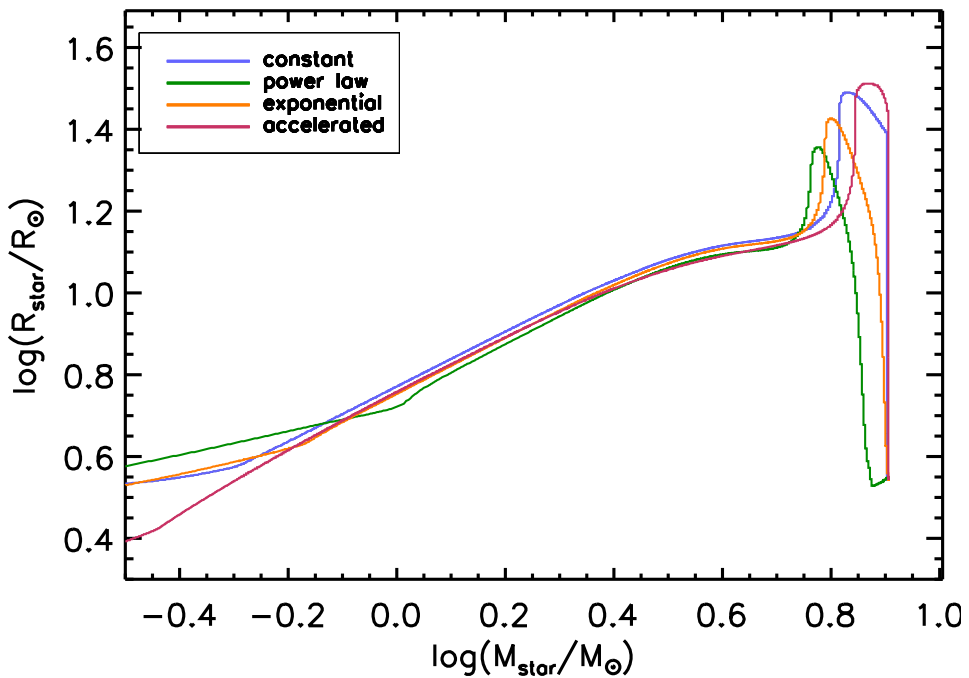


FIGURE 4.5: The radius tracks for protostars of final mass,
 $8M_{\odot}$.

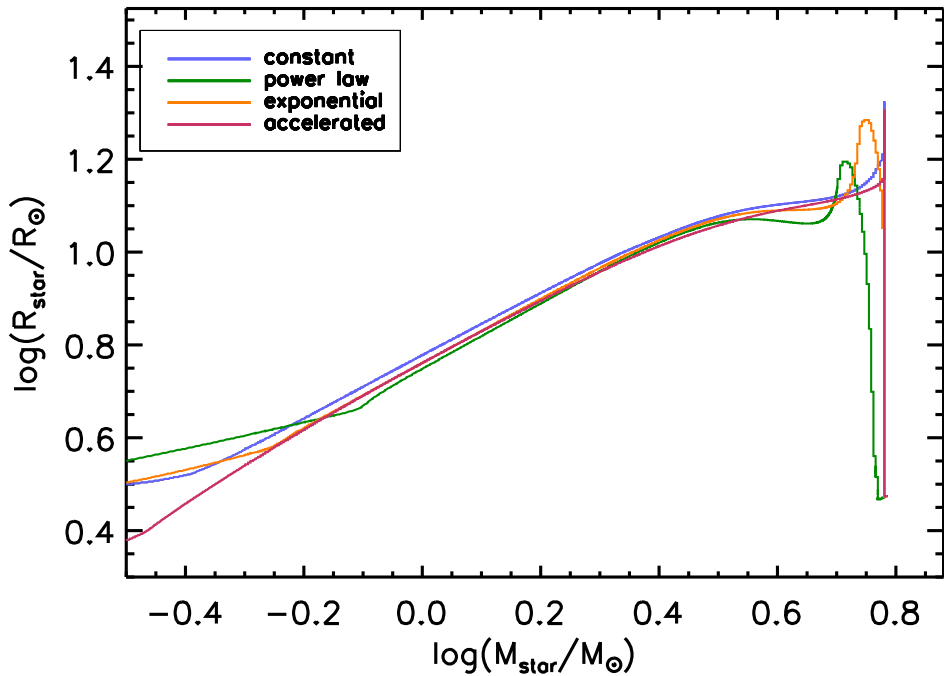


FIGURE 4.6: The radius tracks for protostars of final mass,
 $6M_{\odot}$.

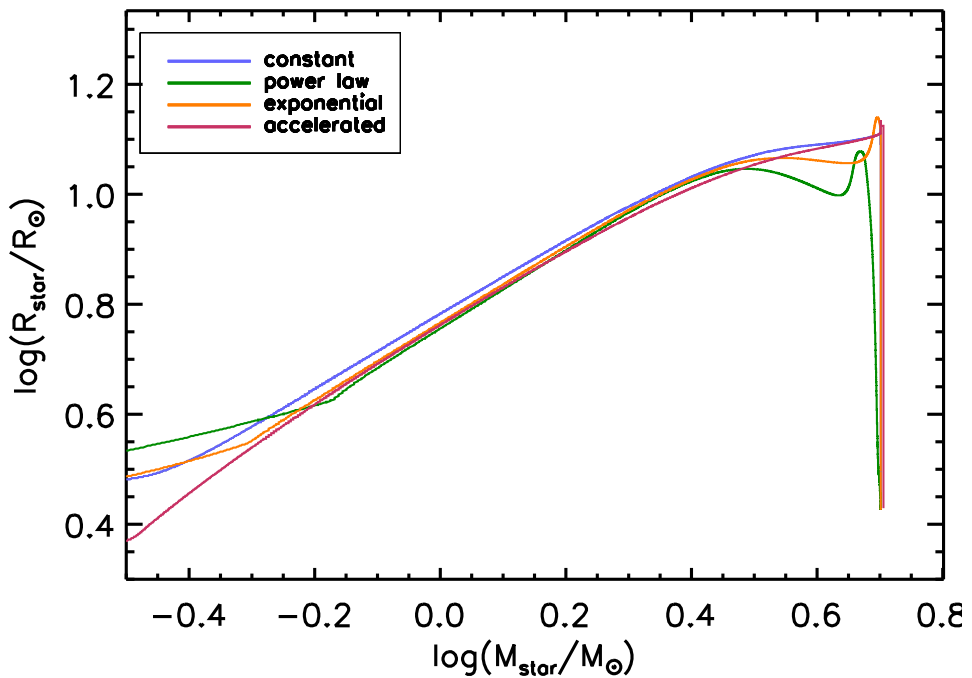


FIGURE 4.7: The radius tracks for protostars of final mass,
 $5M_{\odot}$.

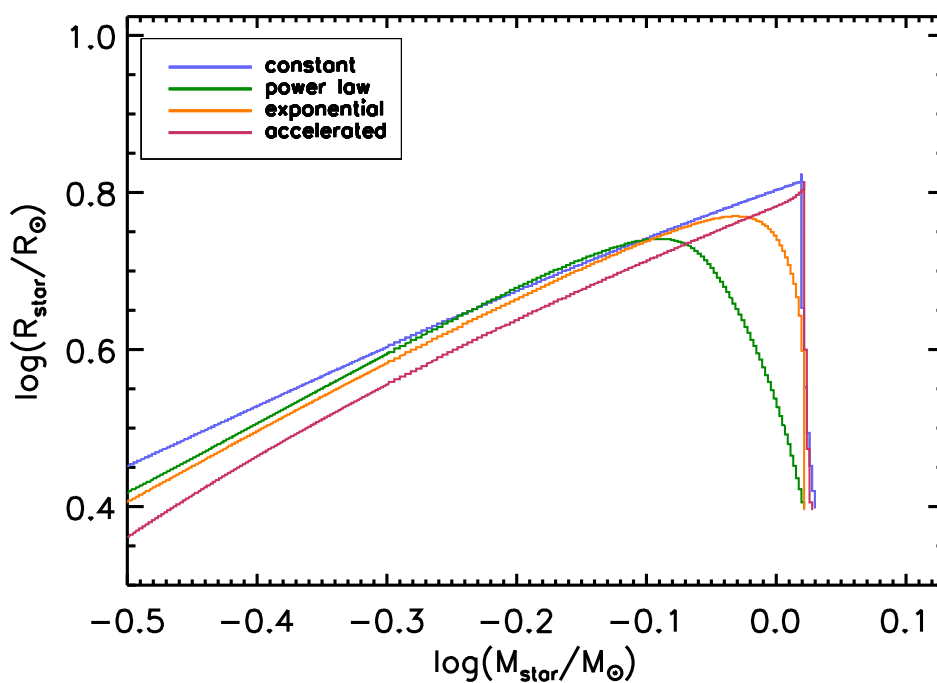


FIGURE 4.8: The radius tracks for protostars of final mass,
 $1M_{\odot}$.

4.2 Theoretical Hertzsprung Russell

We aimed to use the H-R diagram as another indicator to potential significant points of interest in the evolution of protostars. Here we plot the protostellar models individually to keep the track simple to follow and avoiding multiple overlapping points when using group plots. The temperature is not a direct output from the STELLAR code so we use the results given and calculate the temperatures using the 'capsule' code from Smith (2014).

4.2.1 Constant Accretion

This section shows the resultant H-R tracks for the constant accretion model (Figures 4.9 and 4.11).

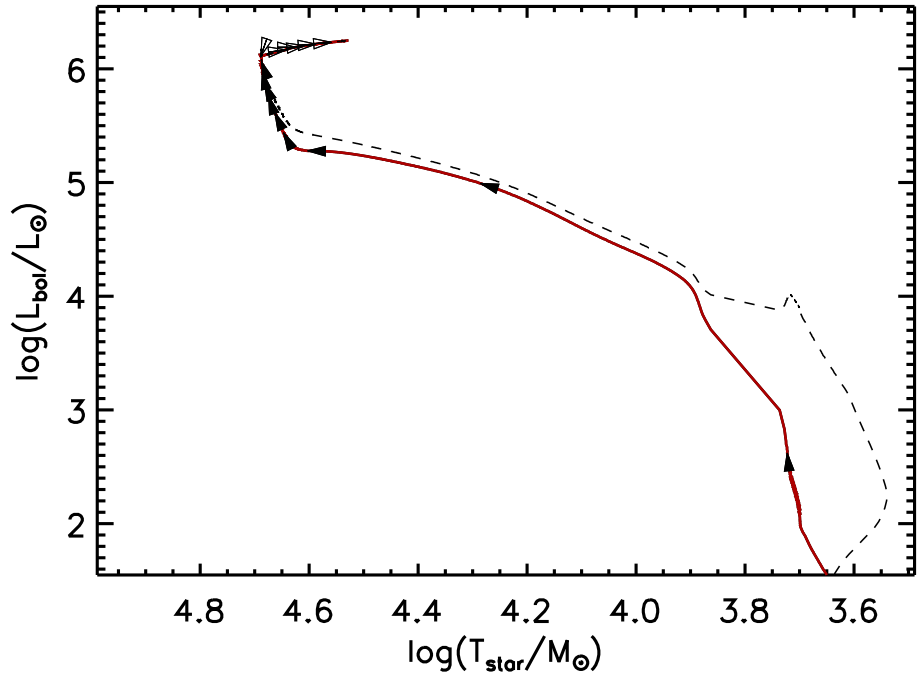


FIGURE 4.9: The H-R track for a star of $100M_{\odot}$ final mass using the cold constant accretion method. The dashed line represents the total luminosity and the solid coloured line represents the core luminosity.

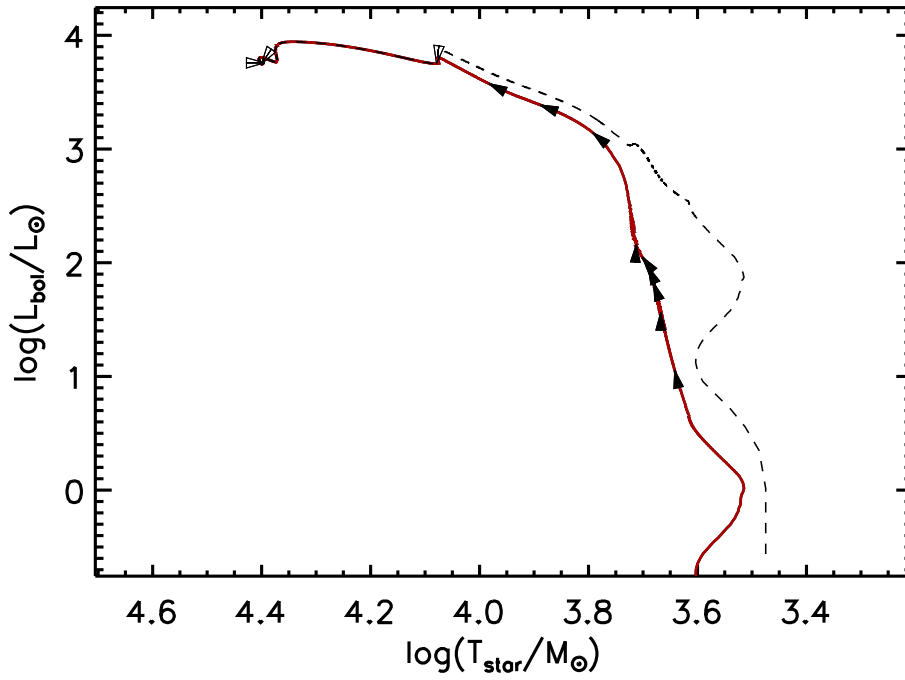


FIGURE 4.10: The H-R track for a star of $10M_{\odot}$ final mass using the cold constant accretion method. The dashed line represents the total luminosity and the solid coloured line represents the core luminosity.

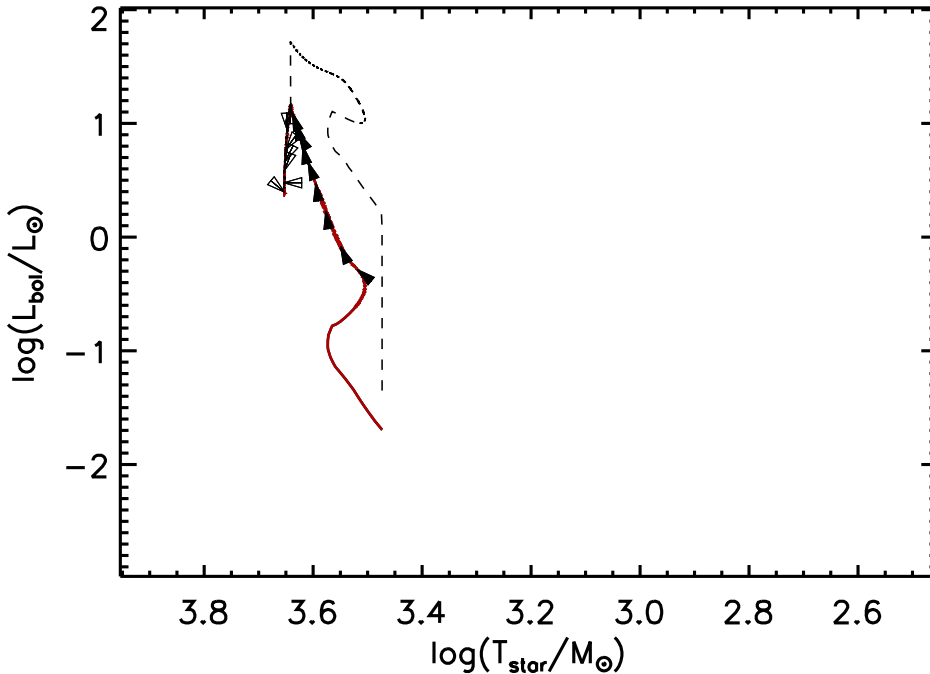


FIGURE 4.11: The H-R track for a star of $1M_{\odot}$ final mass using the cold constant accretion method. The dashed line represents the total luminosity and the solid coloured line represents the core luminosity.

4.2.2 Accelerated Accretion

The following section contains the H-R tracks for the accelerated model (Figures 4.12 and 4.14).

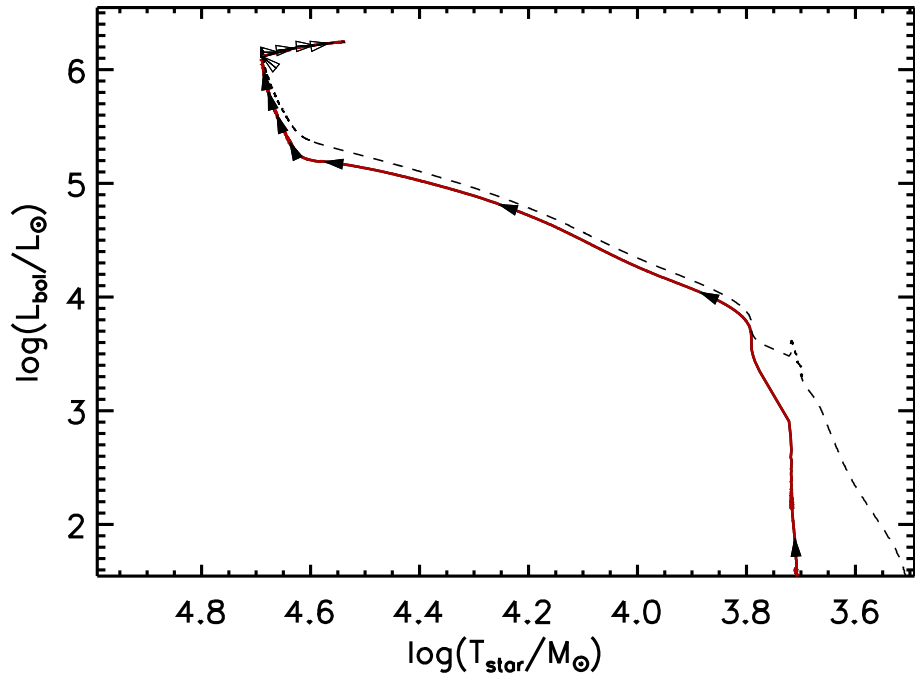


FIGURE 4.12: The H-R track for a star of $100M_{\odot}$ final mass using the cold accelerated accretion method. The dashed line represents the total luminosity and the solid coloured line represents the core luminosity.

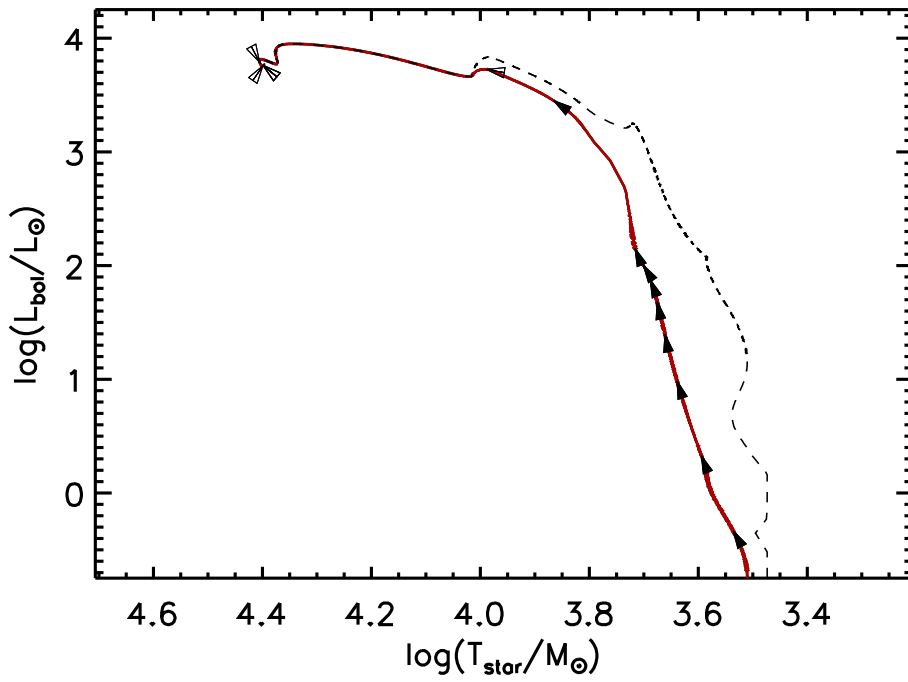


FIGURE 4.13: The H-R track for a star of $10M_{\odot}$ final mass using the cold accelerated accretion method. The dashed line represents the total luminosity and the solid coloured line represents the core luminosity.

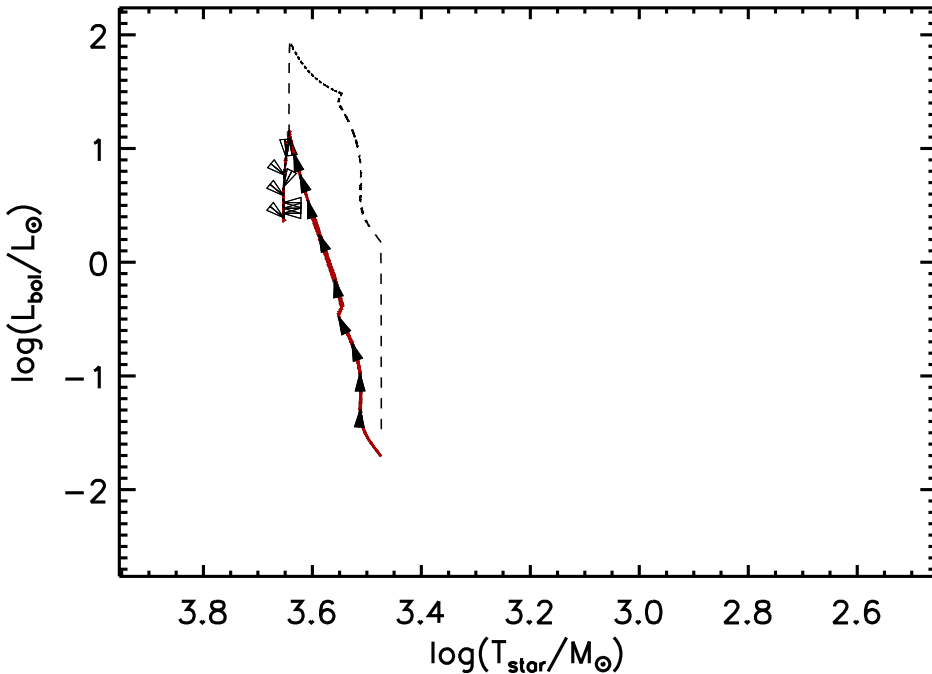


FIGURE 4.14: The H-R track for a star of $1M_{\odot}$ final mass using the cold accelerated accretion method. The dashed line represents the total luminosity and the solid coloured line represents the core luminosity.

4.2.3 Exponential Accretion

The following section contains the H-R tracks for the exponential model (Figures 4.15 to 4.17).

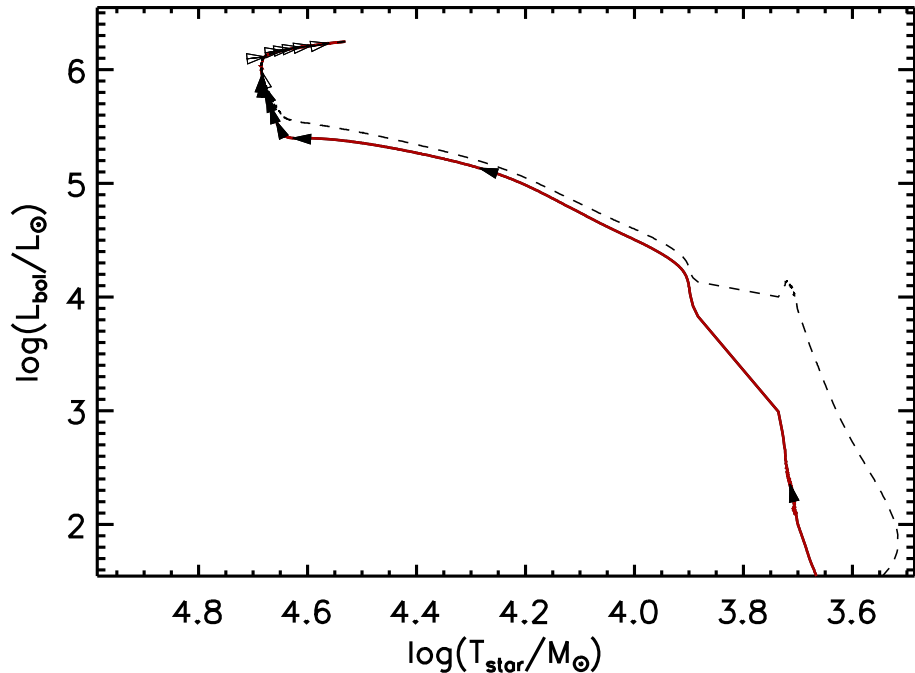


FIGURE 4.15: The H-R track for a star of $100M_{\odot}$ final mass using the cold exponential accretion method. The dashed line represents the total luminosity and the solid coloured line represents the core luminosity.

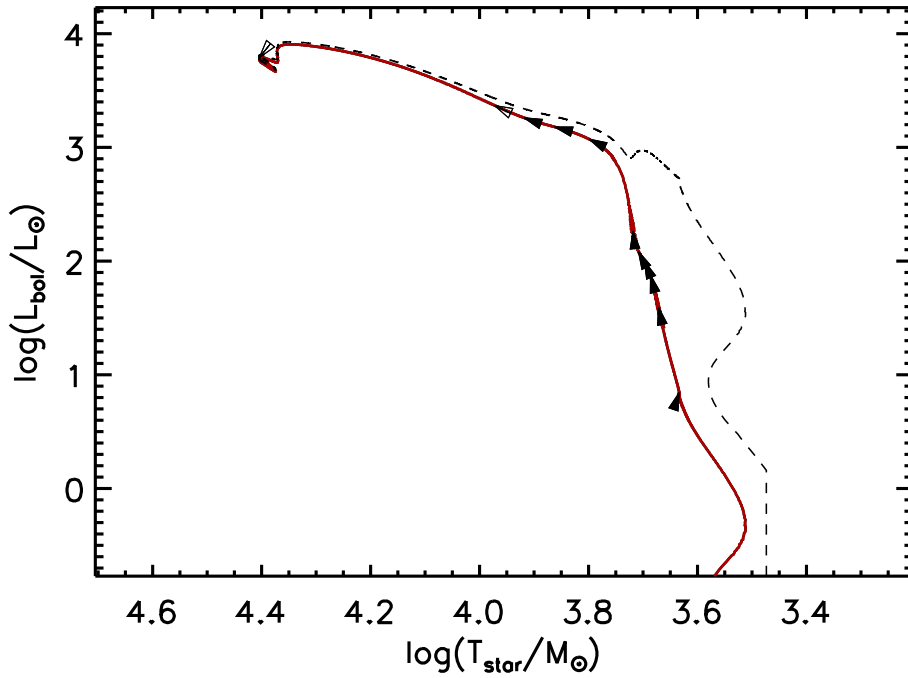


FIGURE 4.16: The H-R track for a star of $10M_{\odot}$ final mass using the cold exponential accretion method. The dashed line represents the total luminosity and the solid coloured line represents the core luminosity.

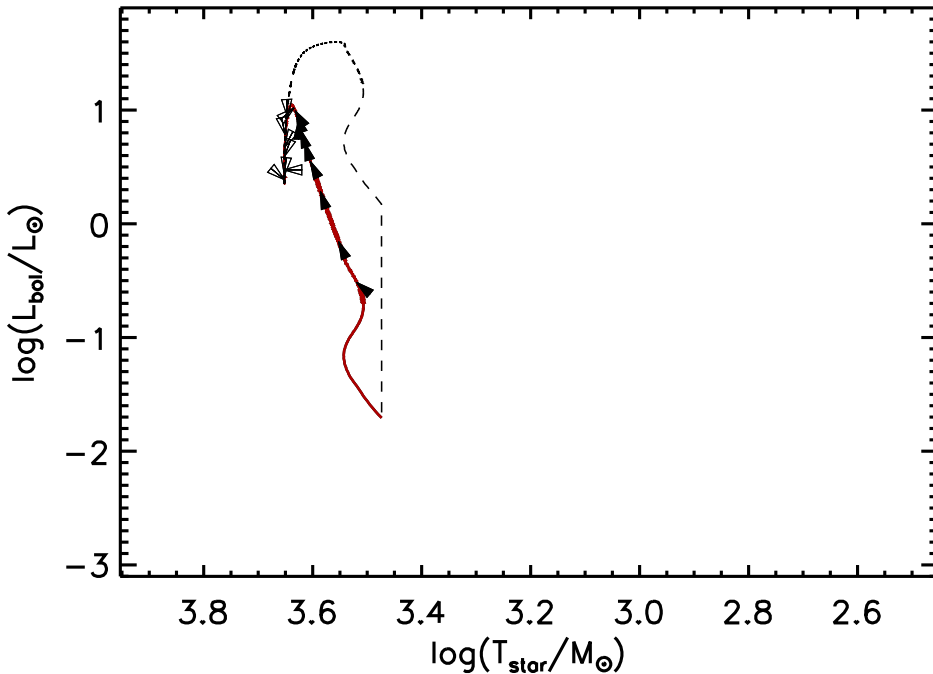


FIGURE 4.17: The H-R track for a star of $1M_{\odot}$ final mass using the cold exponential accretion method. The dashed line represents the total luminosity and the solid coloured line represents the core luminosity.

4.2.4 Power Law Accretion

The following section contains the H-R tracks for the power law accretion model (Figures 4.18 to 4.20).

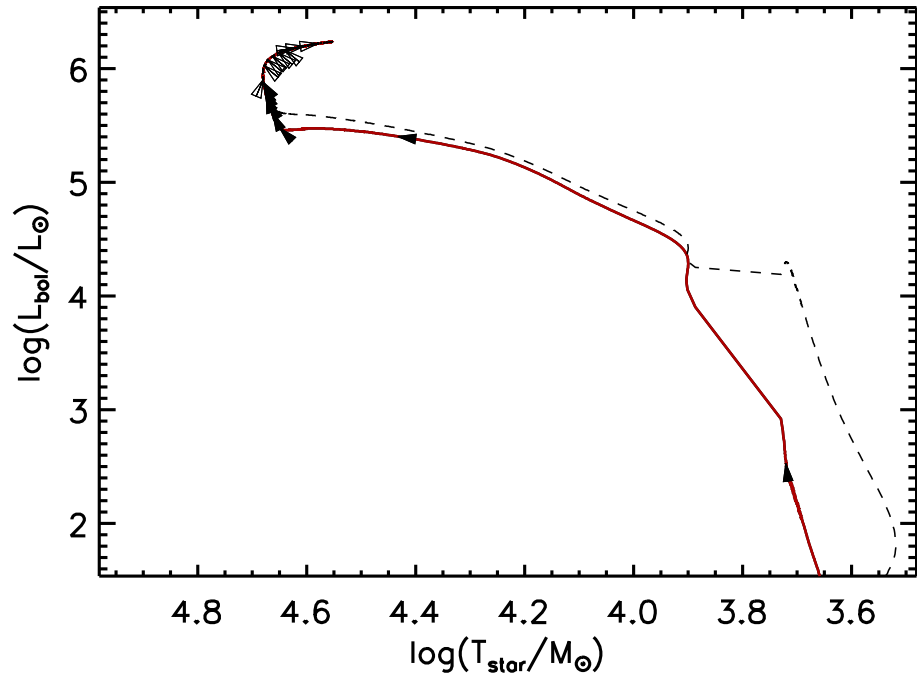


FIGURE 4.18: The H-R track for a star of $100M_{\odot}$ final mass using the cold power law accretion method. The dashed line represents the total luminosity and the solid coloured line represents the core luminosity.

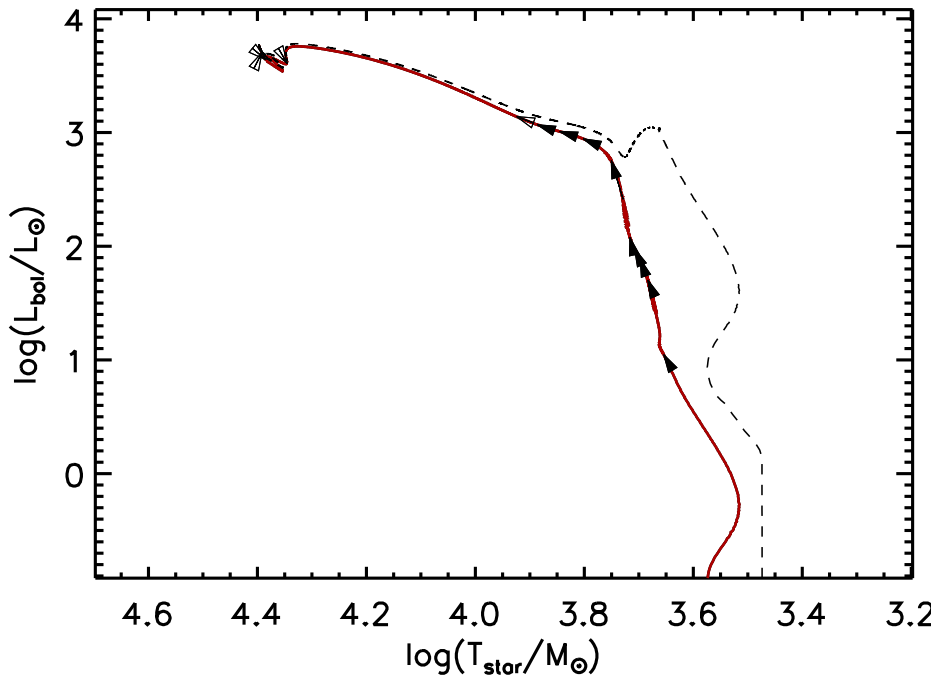


FIGURE 4.19: The H-R track for a star of $10M_{\odot}$ final mass using the cold power law accretion method. The dashed line represents the total luminosity and the solid coloured line represents the core luminosity.

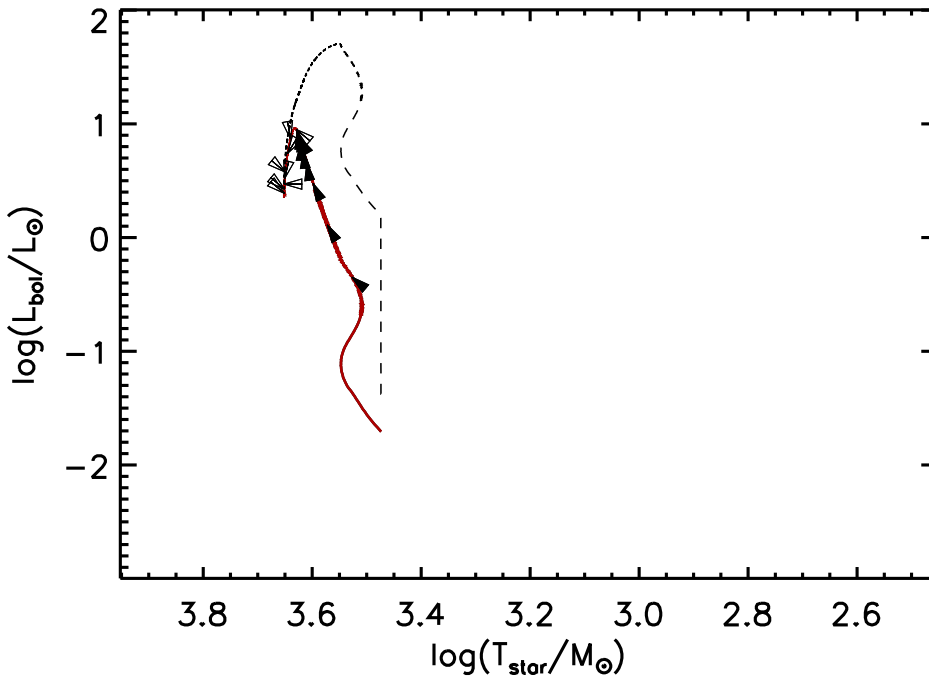


FIGURE 4.20: The H-R track for a star of $1M_{\odot}$ final mass using the cold power law accretion method. The dashed line represents the total luminosity and the solid coloured line represents the core luminosity.

4.3 Mass Luminosity

We plot the clump luminosity - clump mass relation with observational data overlaid. As mentioned previously, the clump mass is calculated as if it is host to many stars, with the modelled star being dominant. We calculate the total mass required for the star to form (envelope mass) using a modified version of Equation 5 found in Molinari et al. (2008), the modification as defined in Smith (2014) is given.

$$M_{env} = \log(2.0) + 0.55 + 1.41 \times \log(3 \times M_f) \quad (4.1)$$

The result is a star formation efficiency of $\approx 21\%$ or envelope mass of ≈ 4.7 times greater than the final mass the star formed, including the mass loss from jets.

We also include recent ATLASGAL data provided by Urquhart et al. (2014). The Urquhart data provides information on a large number of stellar objects which primarily include intermediate to high mass stars found in the region between $280^\circ < l < 350^\circ$. We include dashed straight lines on all the plots which represent fixed values of 0.1, 1, 10 and, 100 luminosity-to-mass ratios. These are centred at $x = 0, y = 1$ on the log scale axis, as this fits well with the observed data as shown later.

4.3.1 Constant Accretion

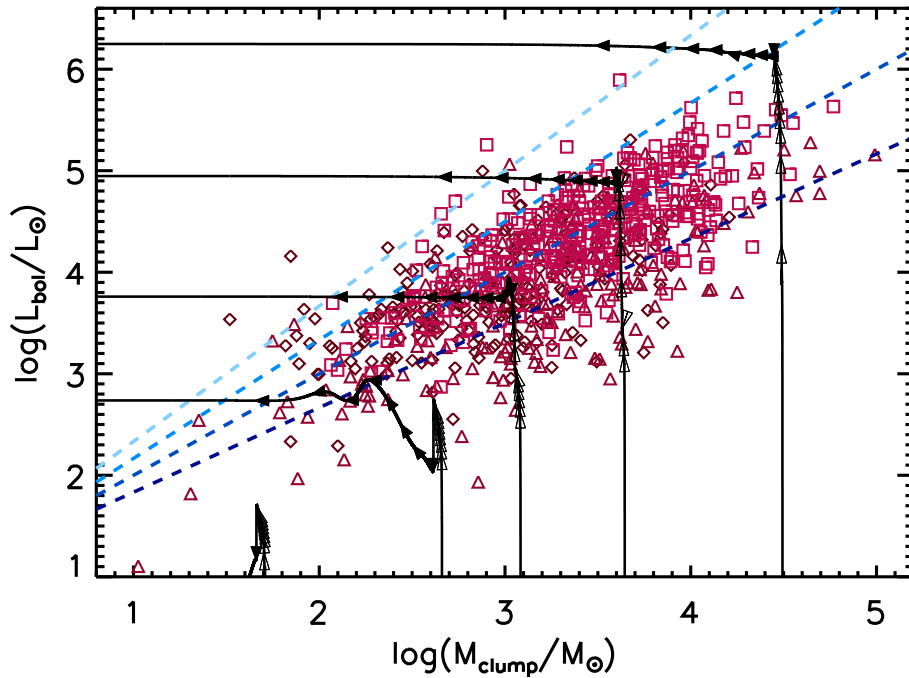


FIGURE 4.21: The Mass Luminosity tracks using the cold constant accretion method. The final masses of the stars associated with tracks from left to right, $1M_{\odot}$, $5M_{\odot}$, $10M_{\odot}$, $25M_{\odot}$, $100M_{\odot}$.

4.3.2 Accelerated Accretion

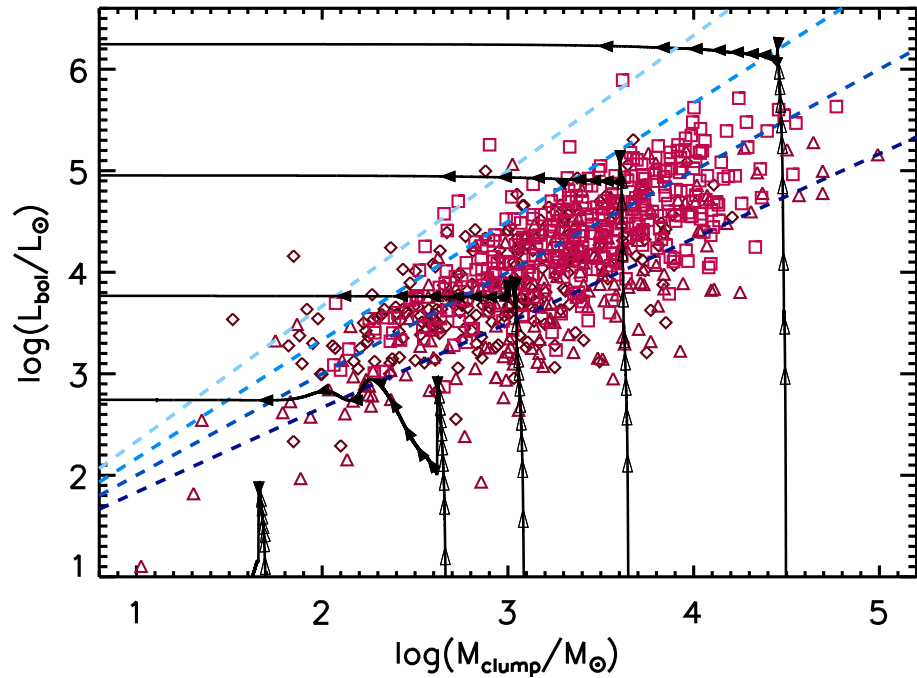


FIGURE 4.22: The Mass Luminosity tracks using the cold accelerated accretion method. The final masses of the stars associated with tracks from left to right, $1M_{\odot}$, $5M_{\odot}$, $10M_{\odot}$, $25M_{\odot}$, $100M_{\odot}$

4.3.3 Exponential Accretion

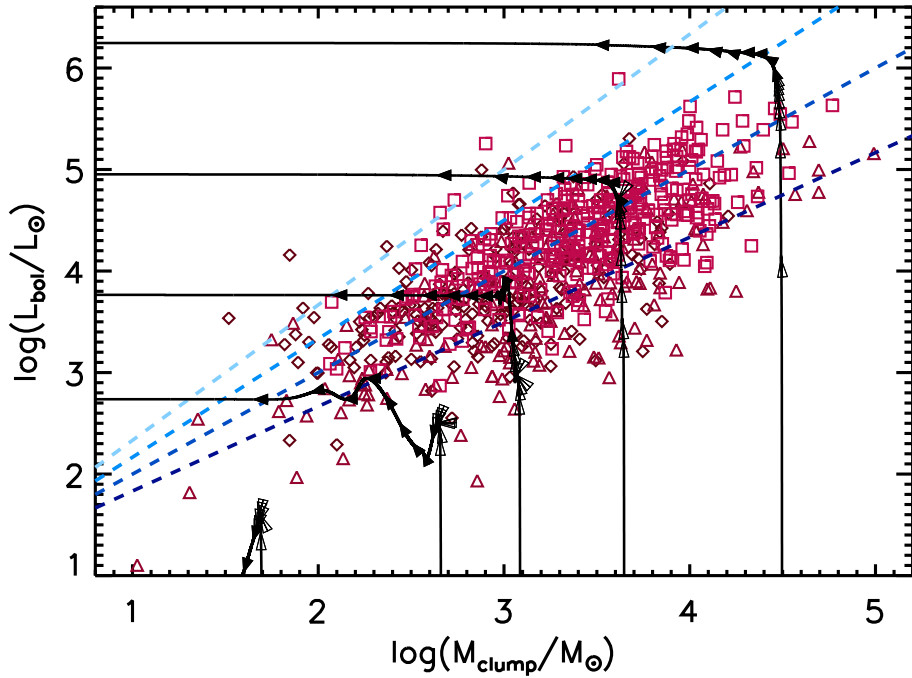


FIGURE 4.23: The Mass Luminosity tracks using the cold exponential accretion method. The final masses of the stars associated with tracks from left to right, $1M_{\odot}$, $5M_{\odot}$, $10M_{\odot}$, $25M_{\odot}$, $100M_{\odot}$

4.3.4 Power Law Accretion

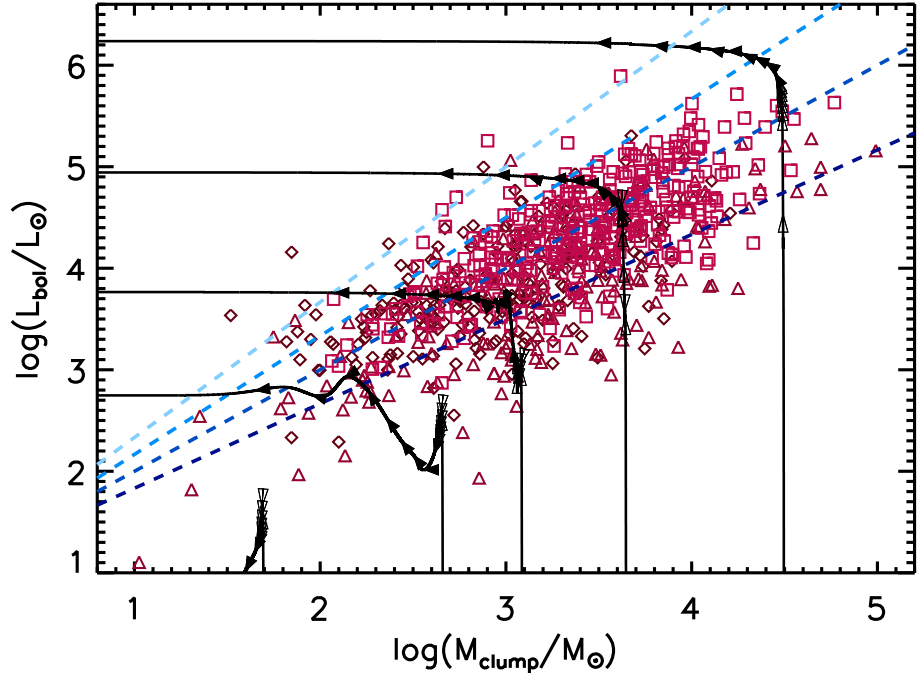


FIGURE 4.24: The tracks for clump luminosity as a function of clump mass using the cold power law accretion method. The final masses of the stars associated with tracks from left to right, $1M_{\odot}$, $5M_{\odot}$, $10M_{\odot}$, $25M_{\odot}$, $100M_{\odot}$.

4.3.5 Clump Luminosity Clump Mass Distribution

Earlier we discussed the use of the luminosity mass diagram as an evolutionary aging mechanism. We aim to compare the model to the observational data from Urquhart et al. (2014).

The instantaneous observation of a single stellar object provides very little information of the long term evolution of stars. Even extended observation times on the order of human lifetimes of a single star would still only offer a small amount of information. As such we implement a logical assumption that overcomes the time constraint. Given a large enough sample of observed objects the resultant data will be a fair distribution and provide a good representation of a full cycle. A consequence of this is that rare events are perhaps not rare in occurrence but are just short lived events and less commonly observed.

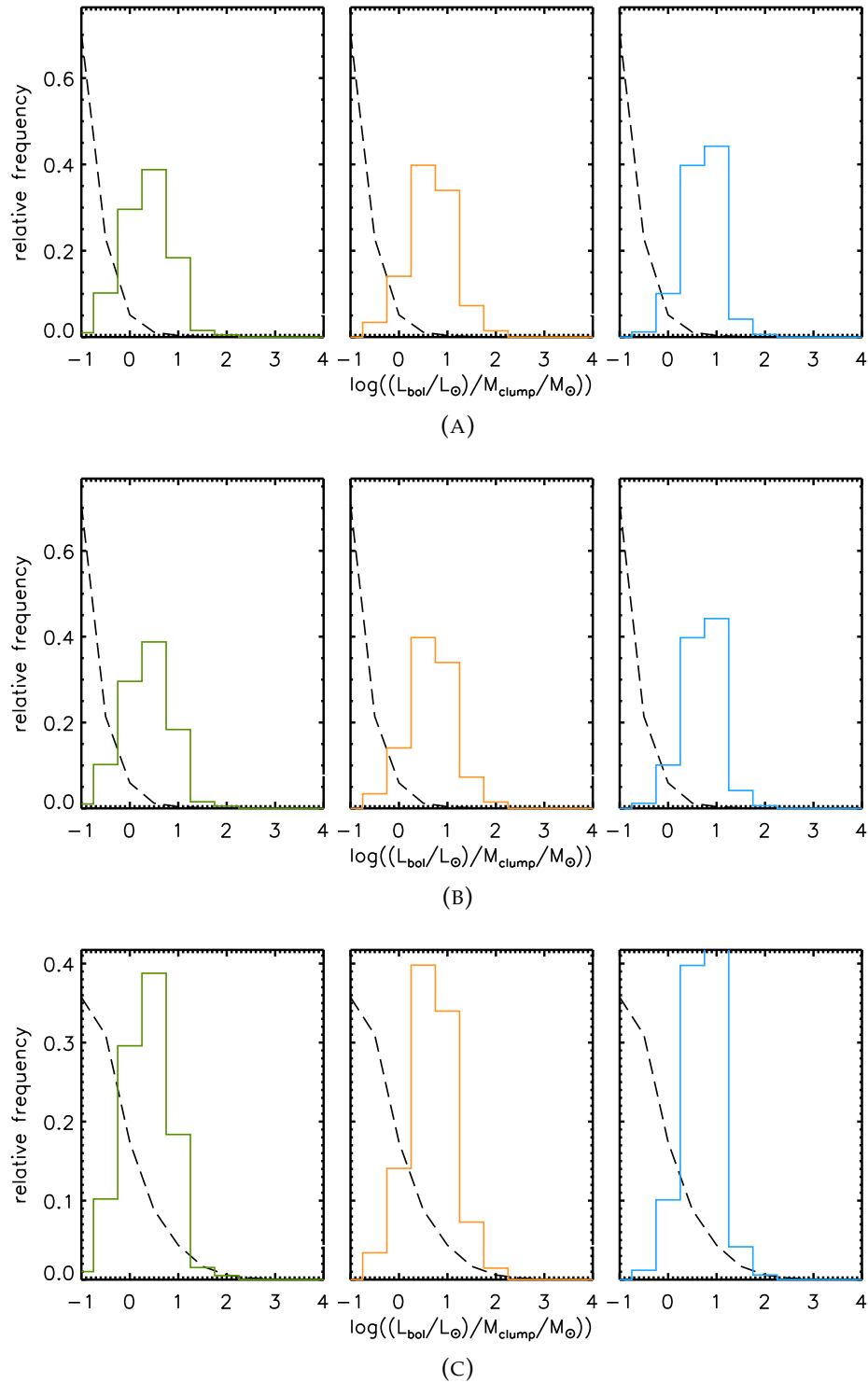
With our model data we find the luminosity mass relation of the star at each iteration. As such our model gives 30,000 ratios at equidistant time intervals; by ‘binning’ the ratios, as done with the ATLASGAL data the resultant distribution of frequencies are representative of the time spent at each ratio bin. The discussed assumption allows us to compare the two different data sets, as such we plot the model histogram over the observed data histograms for each object type. We achieve this by assuming that the chances of observing a star at each equal time step of the evolution are equal. By then binning equidistant time periods on our tracks we can calculate the number of objects in each bin to see how well our model compares to observation. We convert both model and observed data to relative frequency so they can be compared on the same axis scale.

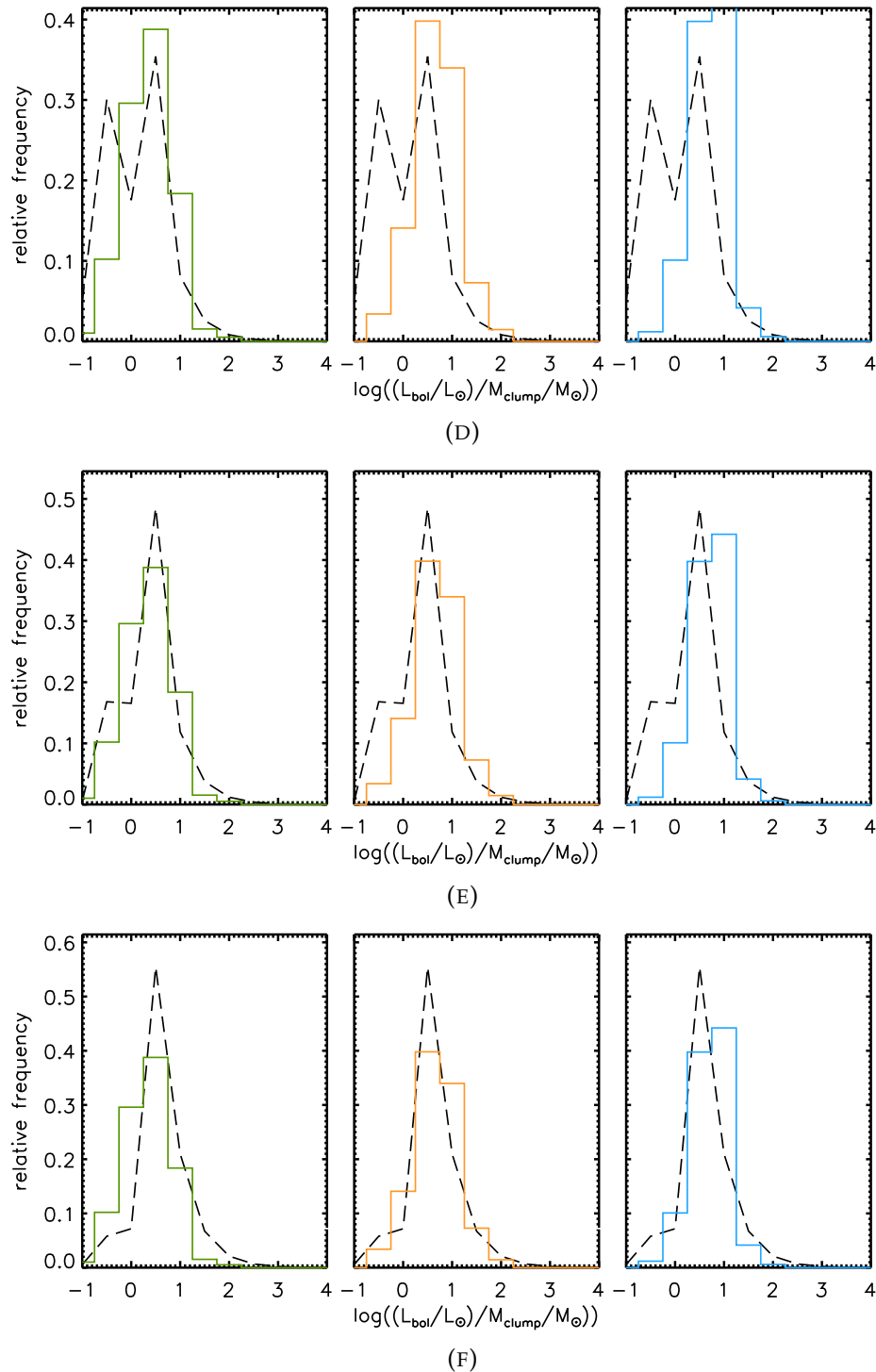
4.3.6 Smooth Accretion results

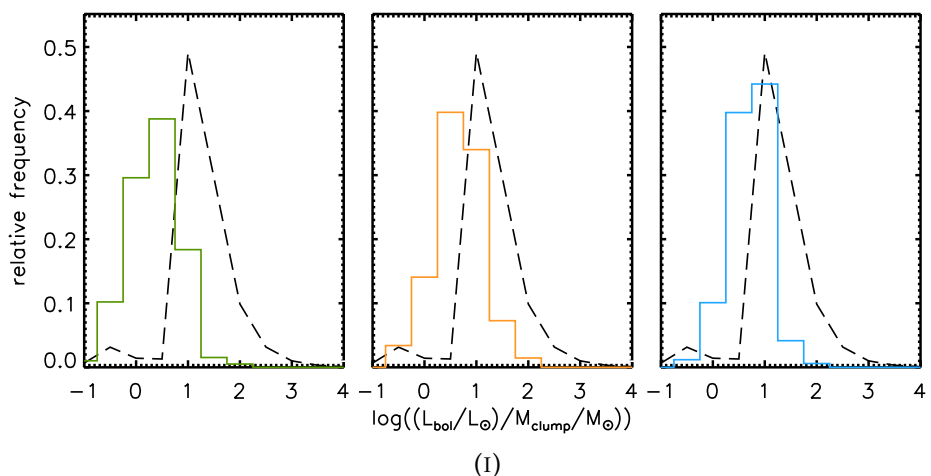
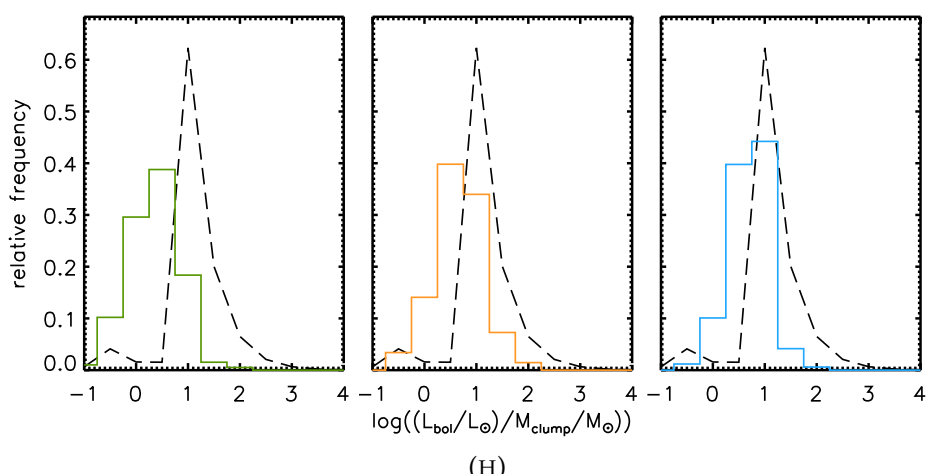
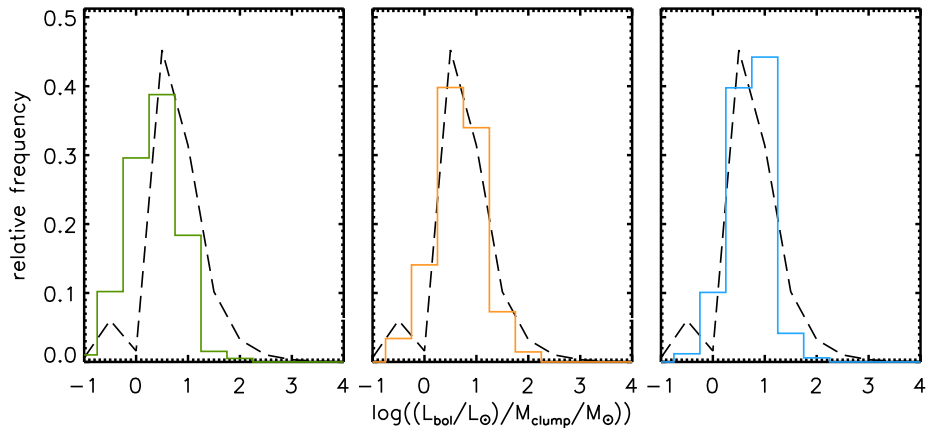
The following sections contain the histogram plots for the accretion model results of final masses. Each set of three figures has the model tracks (dashed line) and one observed object type. The left column contains the MMB distribution (green), the central column contains the YSO distribution (orange) and, the right column contains the HII distribution (blue). The models used from top to bottom are final masses; $1, 2, 4, 5, 6, 8, 10, 15, 20, 25$ and, $100 M_{\odot}$ respectively. This pattern is repeated for each accretion type.

Constant Accretion

FIGURE 4.25: Constant Distribution Results







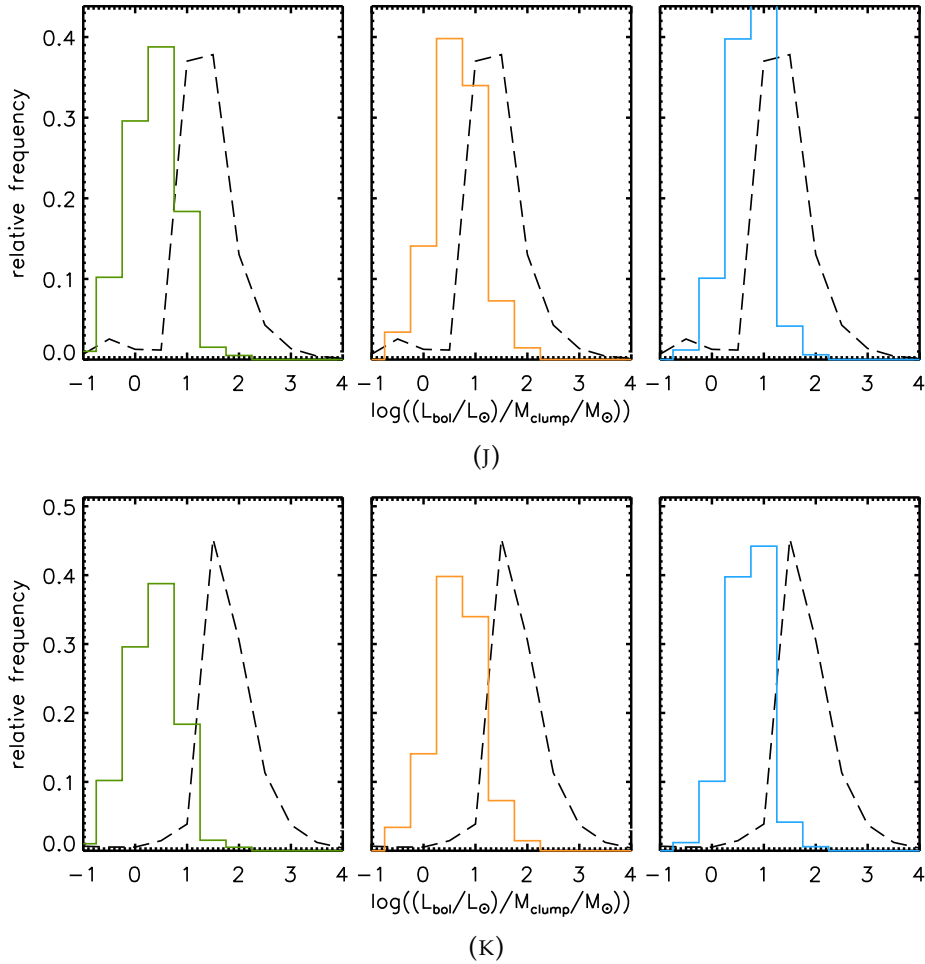
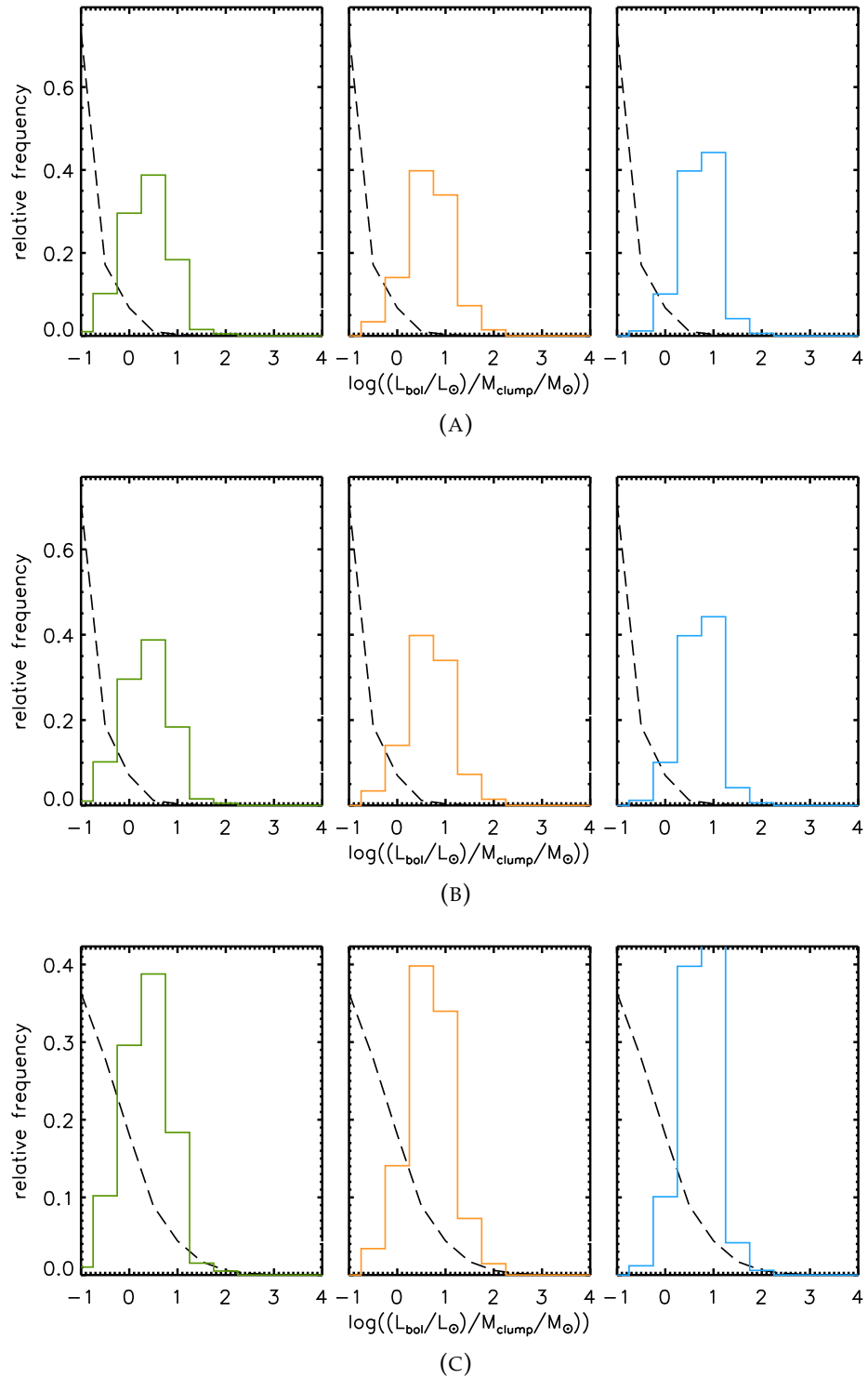
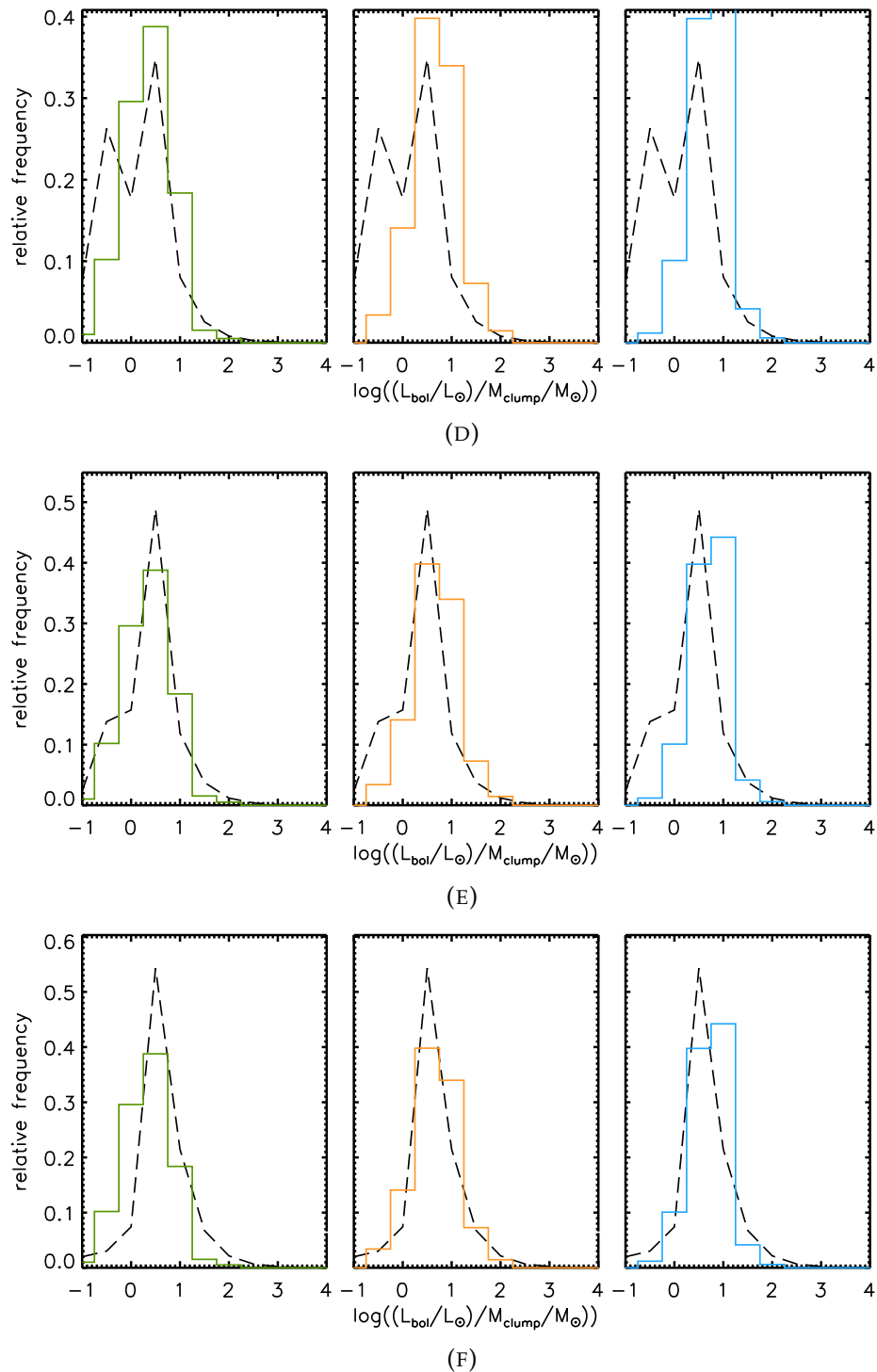


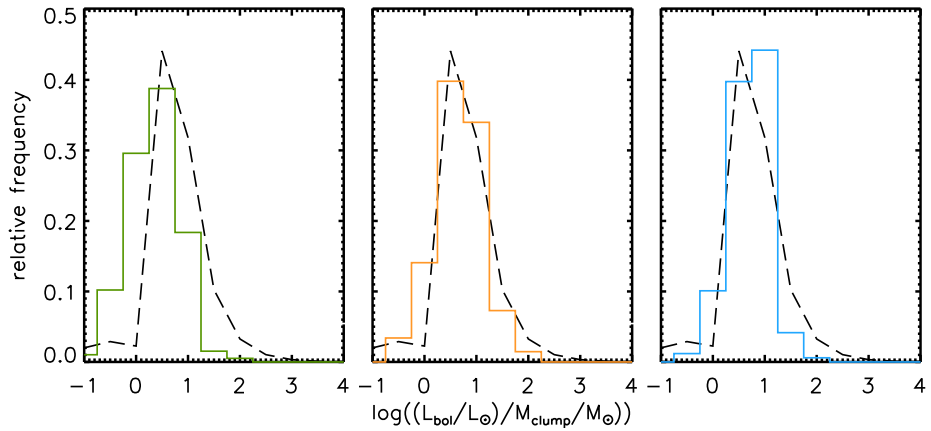
FIGURE 4.25: The ATLASGAL distributions for MMB YSO and HII object types for the left, central and right column respectively. The dashed lines on plots A,B,C,D,E,F,G,H,I,J,K represent star of final masses 1, 2, 4, 5, 6, 8, 10, 15, 20, 25 and, $100M_{\odot}$ respectively, using the constant accretion method.

Accelerated Accretion

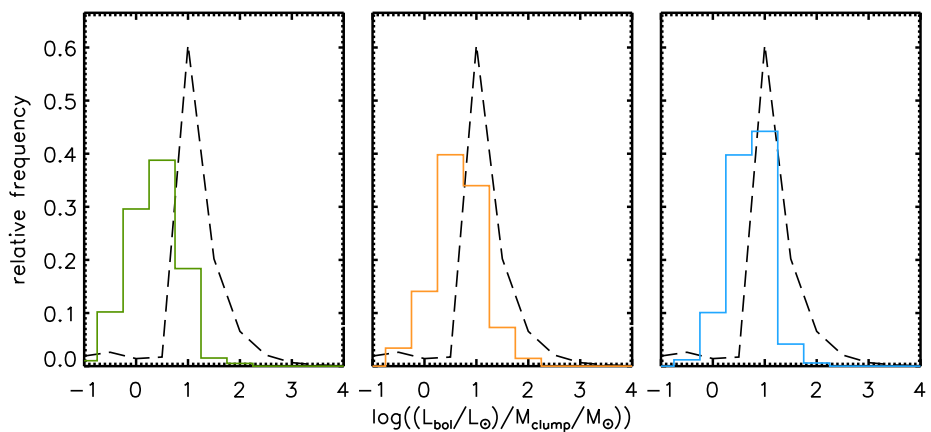
FIGURE 4.26: Accelerated Distribution Results



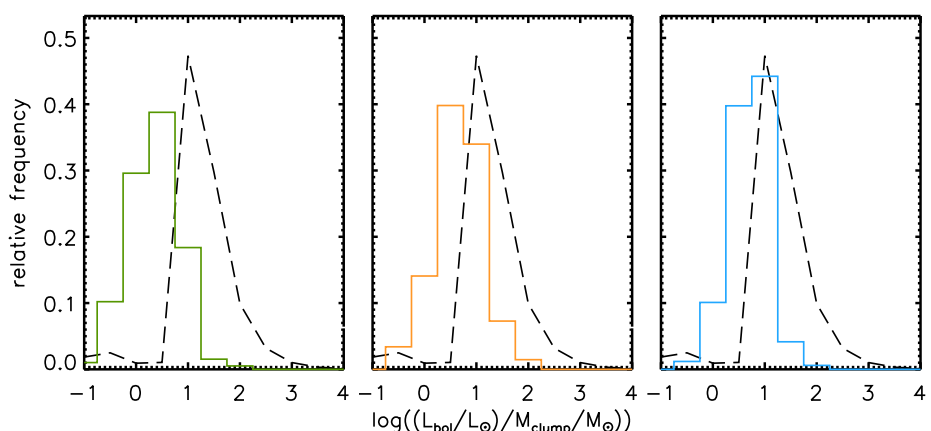




(G)



(H)



(I)

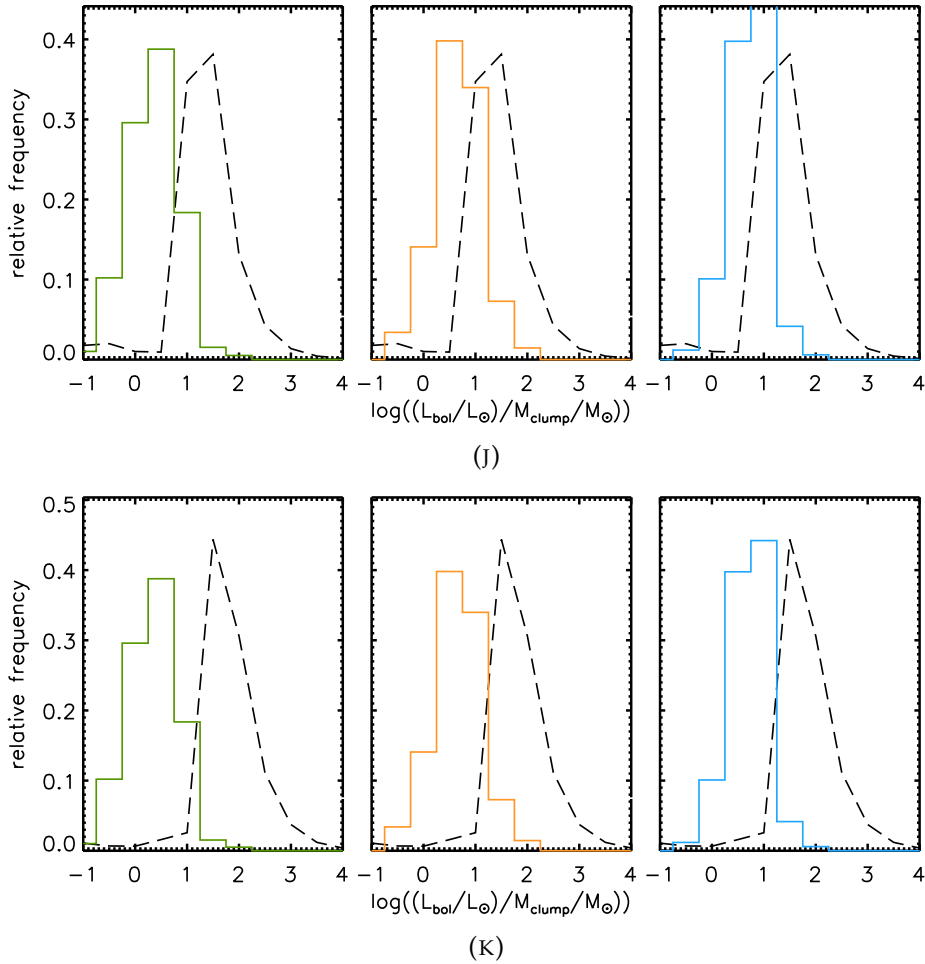
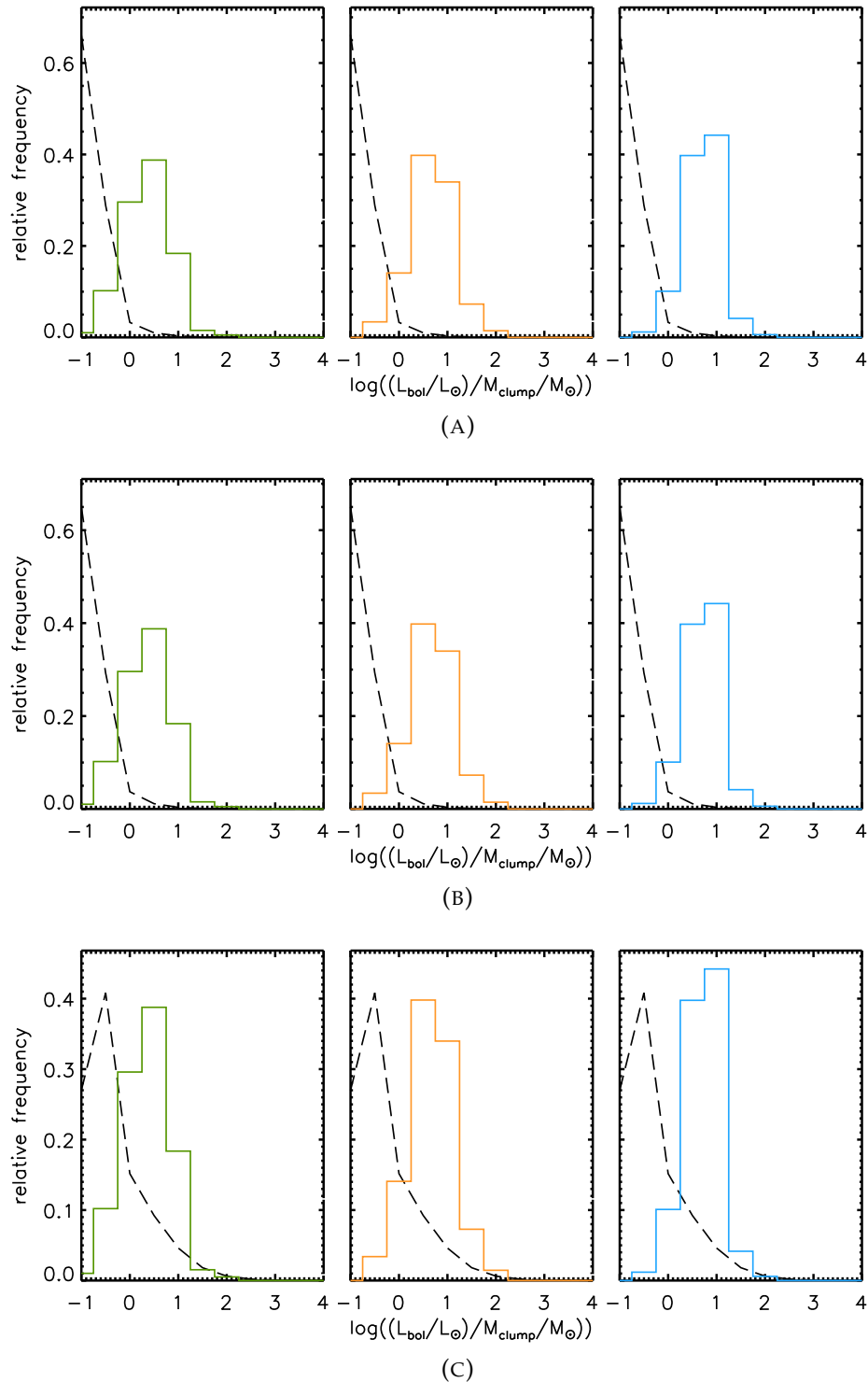
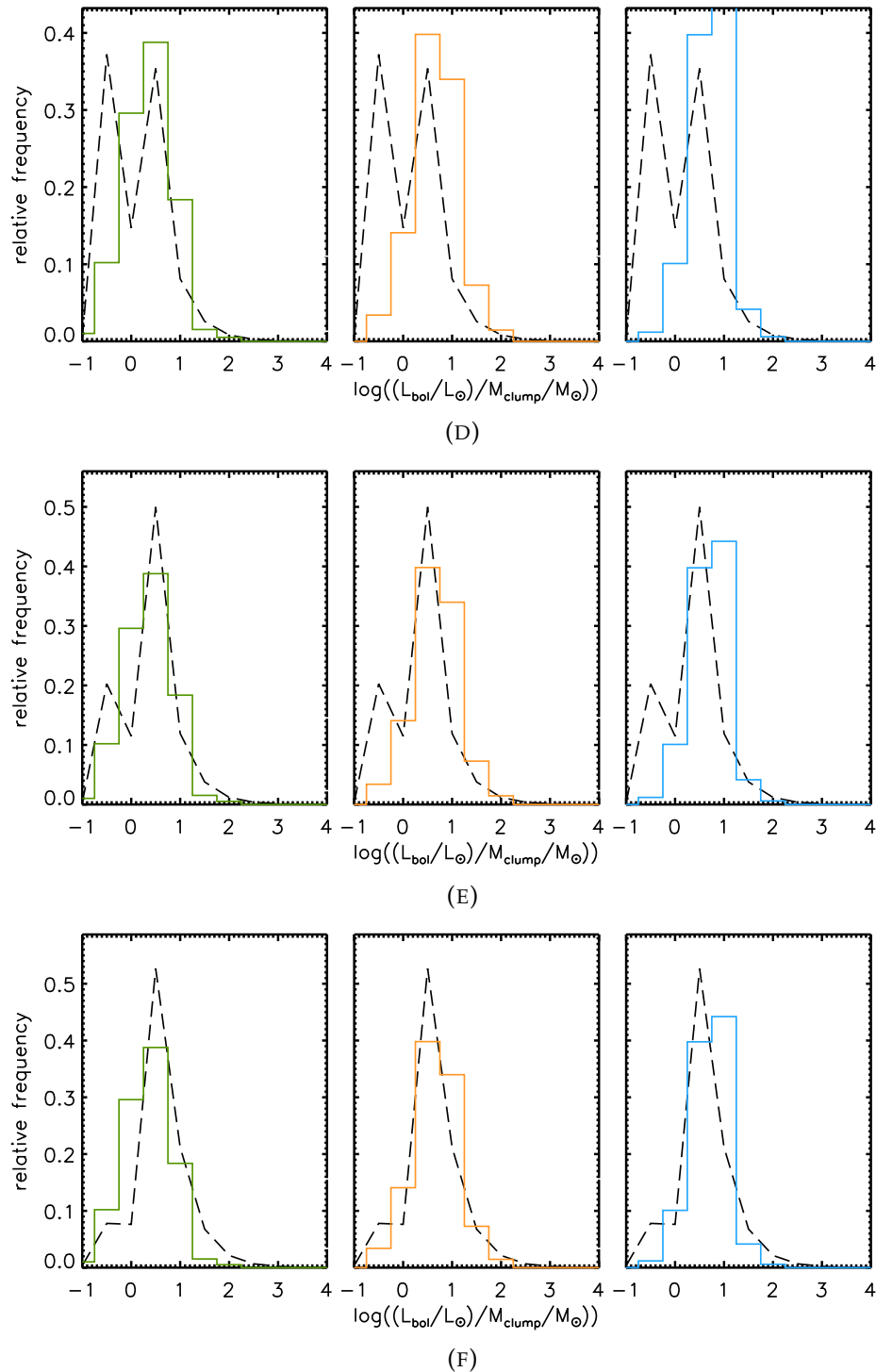


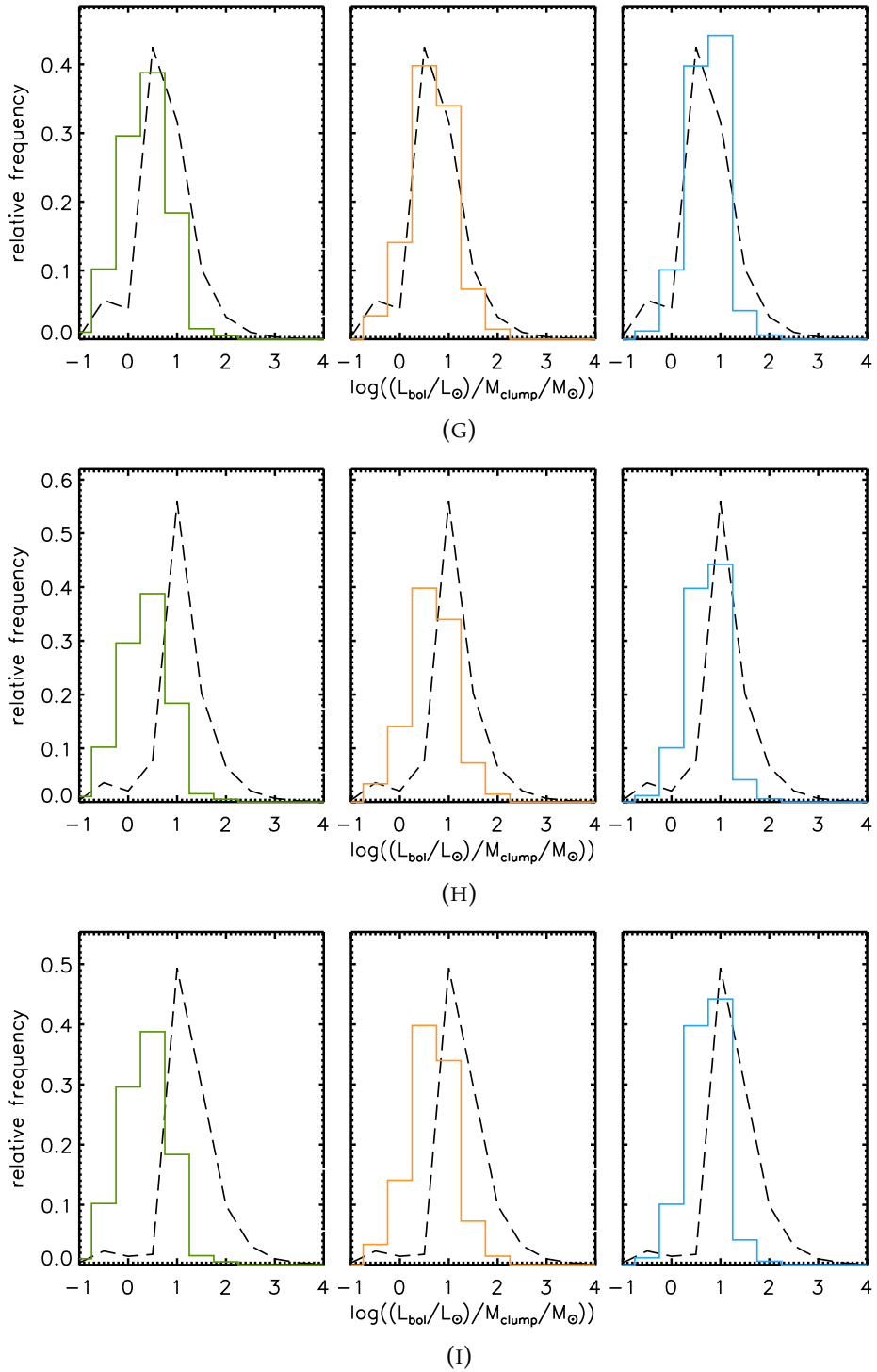
FIGURE 4.26: The ATLASGAL distributions for MMB YSO and HII object types for the left, central and right column respectively. The dashed lines on plots A,B,C,D,E,F,G,H,I,J,K represent star of final masses 1, 2, 4, 5, 6, 8, 10, 15, 20, 25 and, $100 M_{\odot}$ respectively, through the accelerated accretion.

Exponential Accretion

FIGURE 4.27: Exponential Distribution Results







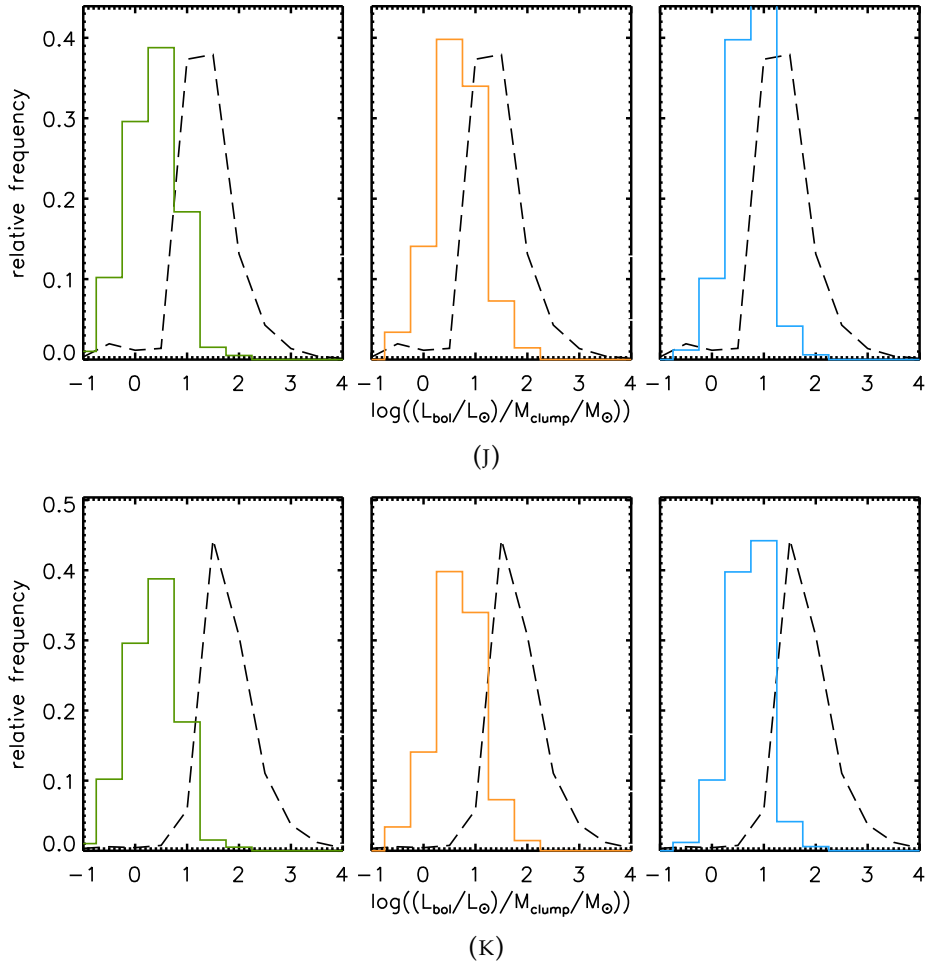
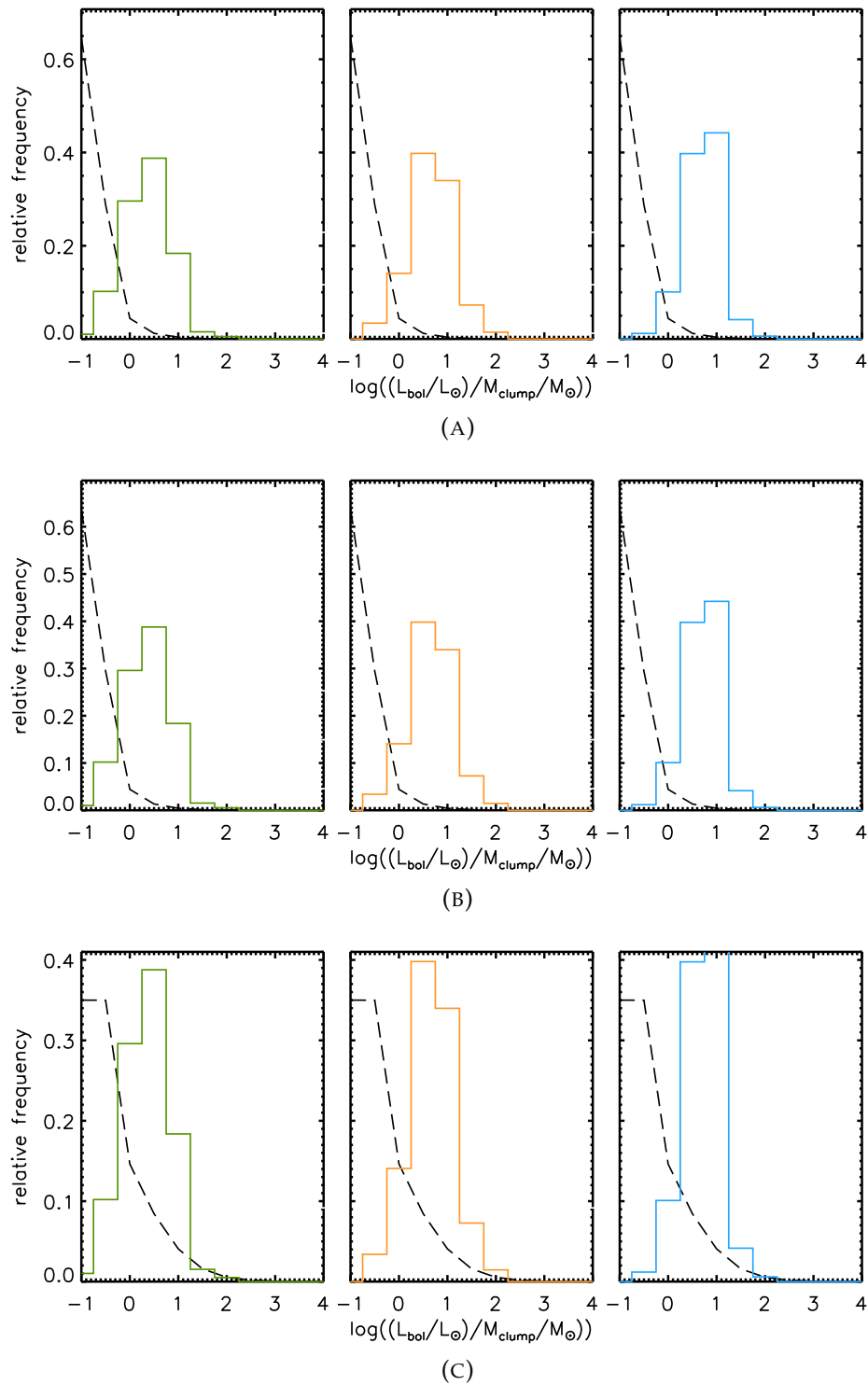
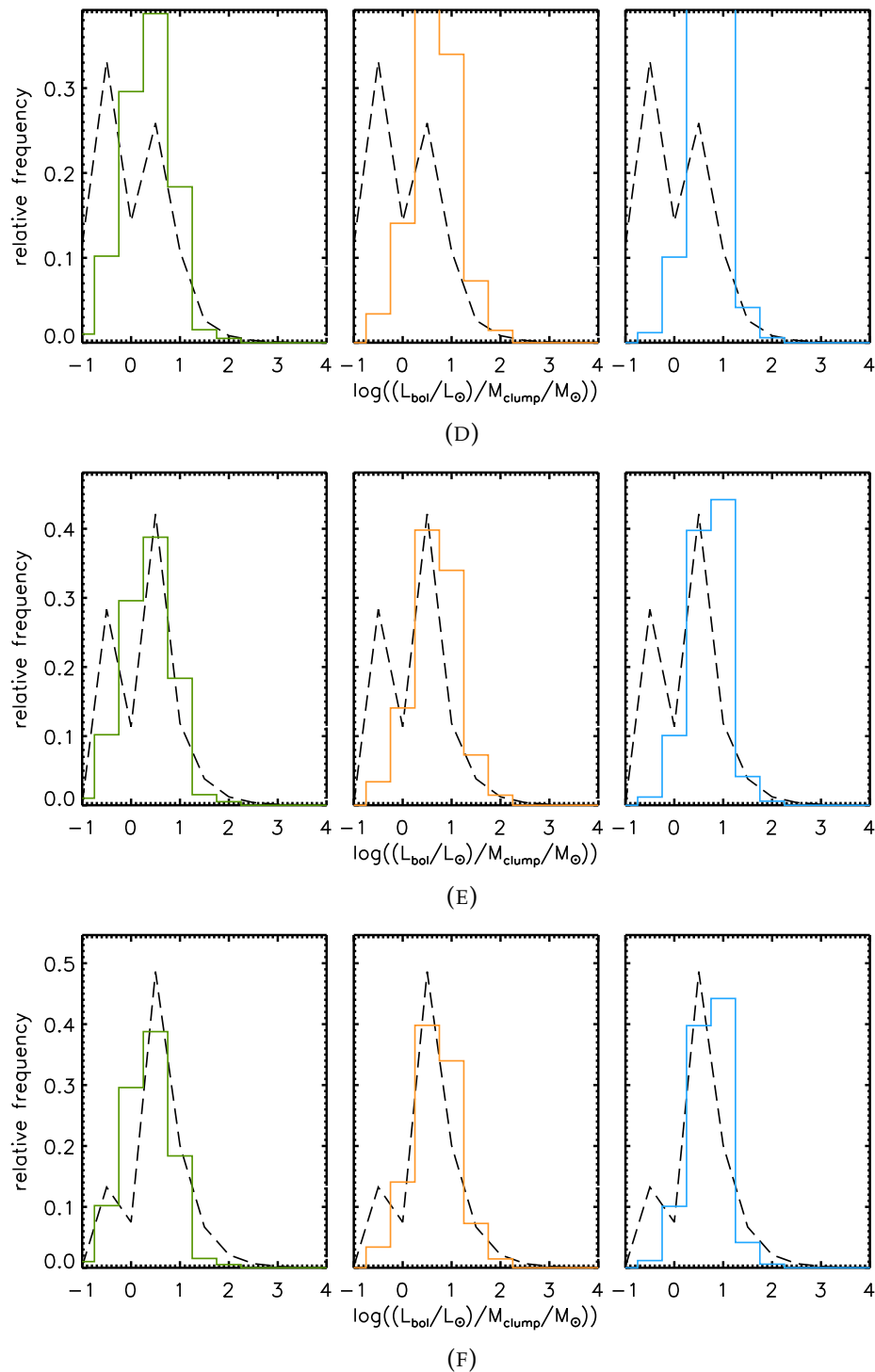


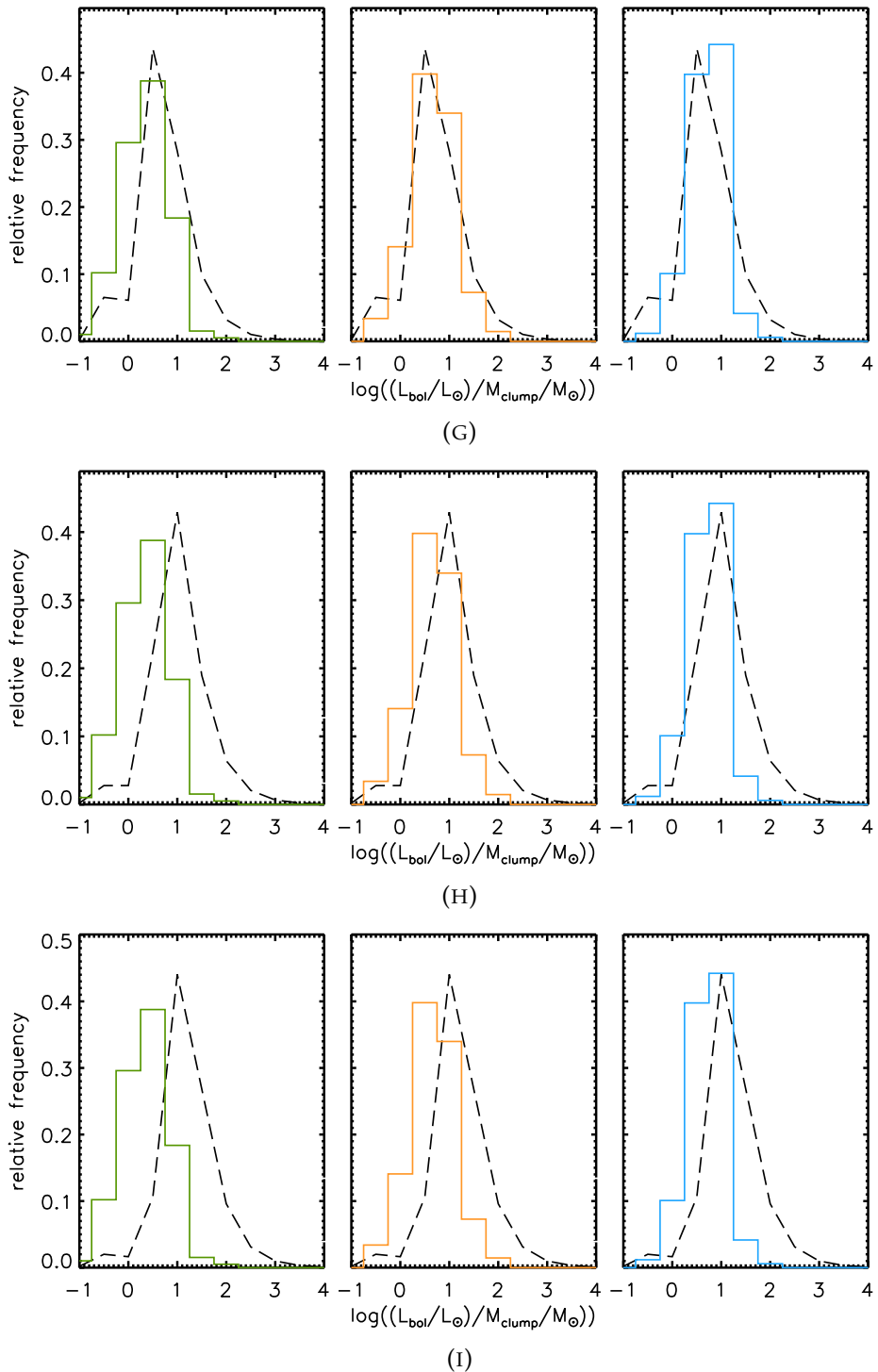
FIGURE 4.27: The ATLASGAL distributions for MMB YSO and HII object types for the left, central and right column respectively. The dashed lines on plots A,B,C,D,E,F,G,H,I,J,K represent star of final masses 1, 2, 4, 5, 6, 8, 10, 15, 20, 25 and, $100 M_{\odot}$ respectively, through the exponential accretion method.

Power Law Accretion

FIGURE 4.28: Power Law Distribution Results







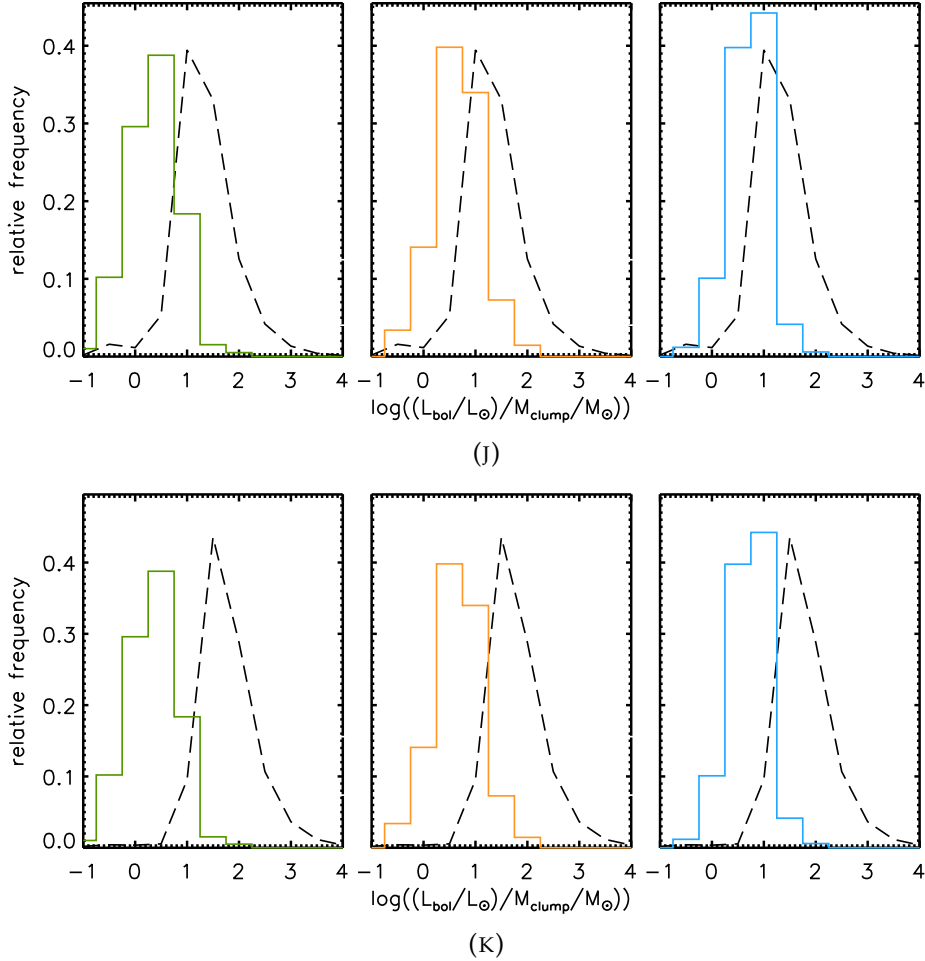


FIGURE 4.28: The ATLASGAL distributions for MMB YSO and HII object types for the left, central and right column respectively. The dashed lines on plots A,B,C,D,E,F,G,H,I,J,K represent star of final masses 1, 2, 4, 5, 6, 8, 10, 15, 20, 25 and, $100 M_{\odot}$ respectively, through the power law accretion method.

4.4 Episodic Accretion Bursts

We incorporated episodic accretion bursts as recent findings have shown their significance in the protostellar growth process. The process of applying bursts by using a modulo function was successful and required minimal alterations to get the stellar code to work with it.

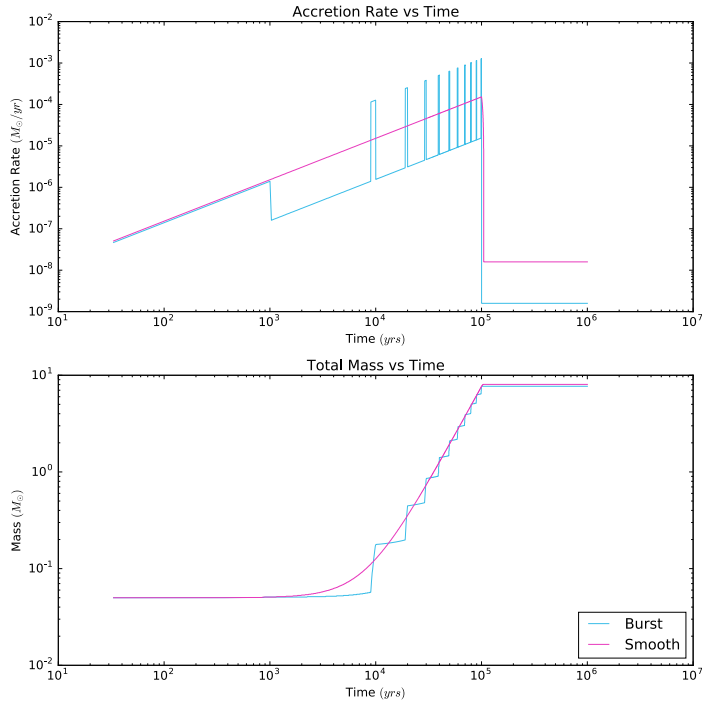


FIGURE 4.29: The accelerated accretion rate over time for both the smooth and burst accretion models. The final mass achieved is shown in the lower graph.

Figure 4.29 shows the accretion rate and mass versus time for the accelerated accretion model with, and without, bursts as an example of how the process works. The accretion rate without bursts can be viewed as a base in which the modulo function (Eq. 3.8 and 3.9) modifies to get the burst result, the result is an identical final mass. It was found that the STELLAR code would become unstable and cease running when exceeding a certain mass. The episodic accretion rate during a high phase is nearly an order of magnitude greater than the smooth accretion rate in the same time frame. As such, when trying to produce a $100M_{\odot}$ star the rate will peak at equivalent rate for a $1,000M_{\odot}$ star in the base model. It was found that the code was only stable for producing stars up to $\approx 20 - 25M_{\odot}$ masses. The following results will reflect this.

TABLE 4.3: The data table of final mass and the final radius using the respective accretion method including episodic bursts. Note that the accelerated accretion method could not run to completion for final masses greater than $16M_{\odot}$.

Final Mass (M_{\odot})	Accretion Method incl. bursts Final Radius (R_{\odot})			
	Accelerated	Constant	Exponential	Power Law
1	2.43	2.51	2.53	2.56
2	3.36	3.5	3.52	3.52
5	2.67	2.7	2.7	2.73
6	2.94	4.83	3.0	3.03
8	3.55	3.59	3.59	3.6
10	4.05	4.14	4.14	4.15
15	5.37	5.43	5.41	5.41
20	N/A	6.3	6.59	6.58

TABLE 4.4: The data table of final mass and peak radius achieved using the respective accretion method. Note that the accelerated accretion method could not run to completion for final masses greater than $16M_{\odot}$.

Final Mass (M_{\odot})	Accretion Method incl. bursts Peak Radius (R_{\odot})			
	Accelerated	Constant	Exponential	Power Law
1	64.97	68.13	83.8	89.55
2	89.12	93.72	101.34	111.4
5	238.61	152.36	146.61	130.8
6	1170.04	344.98	205.55	171.05
8	1305.16	497.34	293.23	343.54
10	948.68	674.14	590.77	468.59
15	1868.62	620.96	666.95	764.7
20	N/A	334.91	1007.62	1266.35

4.4.1 Mass radius

We again tablulate the important radii data and mass data for all episodic accretion models to view points of significant interest, noting the accelerated model could not complete the full evolution at masses greater than $16M_{\odot}$, this is discussed later.

; The following Mass-Radius (Figures 4.30 to 4.37) graphs show four tracks each of different stellar mass but all using the same accretion model. This differs from the previous Mass-Radius graphs that included all models but for the same mass. The inclusion of bursts results in large overlaps between tracks making it difficult to distinguish the tracks, notably more so when the tracks are of the same mass.

Constant Accretion

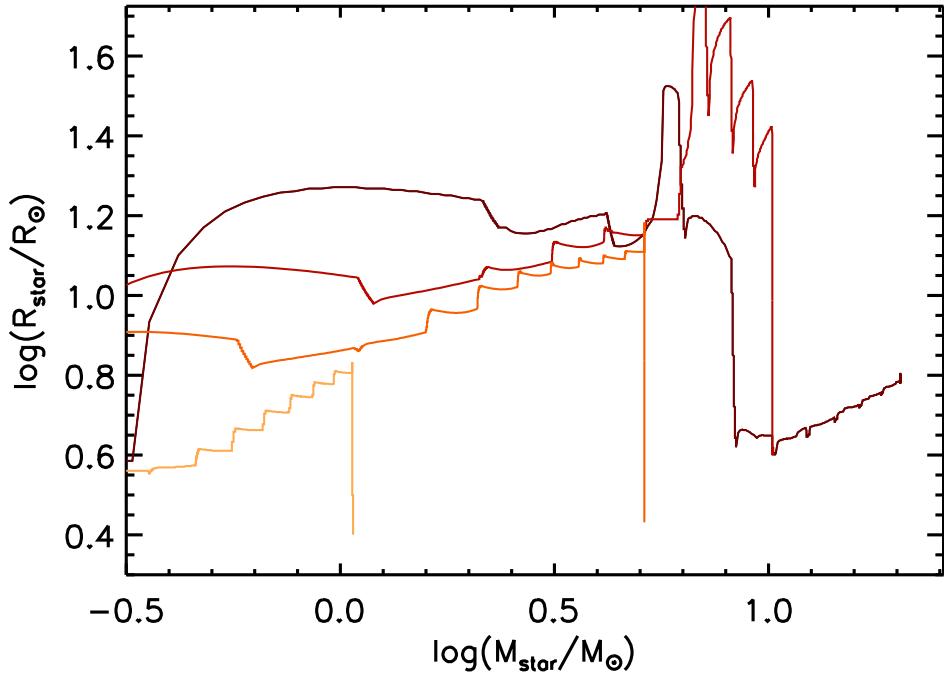


FIGURE 4.30: The radius as function of mass tracks for cold constant accretion with episodic bursts. The tracks stars of final masses $1M_{\odot}$, $5M_{\odot}$, $10M_{\odot}$ and, $20M_{\odot}$ respectively.

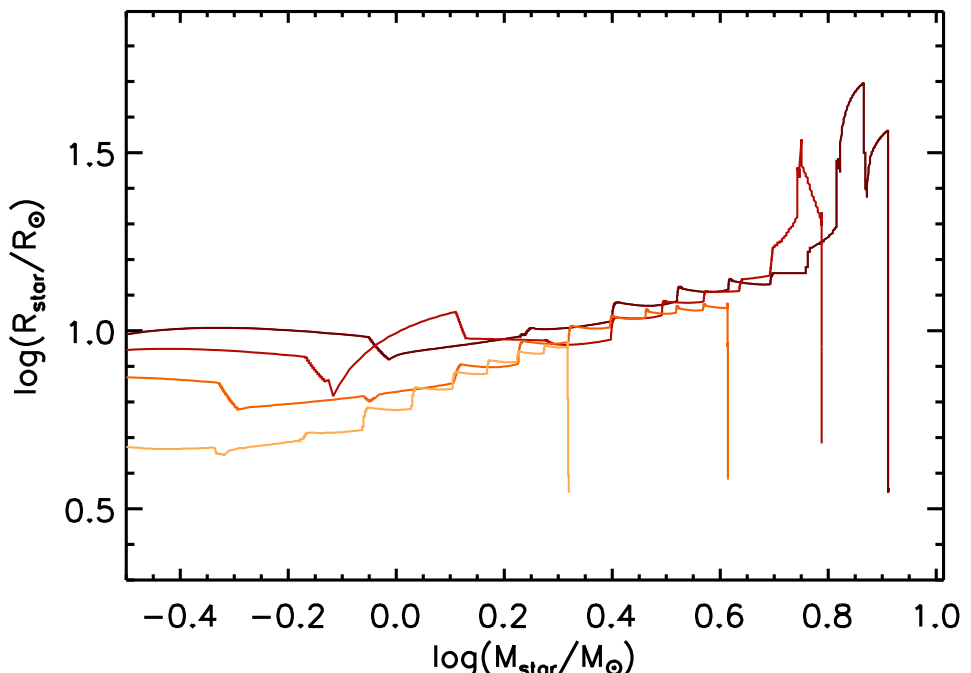


FIGURE 4.31: The radius as function of mass tracks for cold constant accretion with episodic bursts. The tracks of final masses $2M_{\odot}$, $4M_{\odot}$, $6M_{\odot}$ and, $8M_{\odot}$ respectively.

Accelerated Model

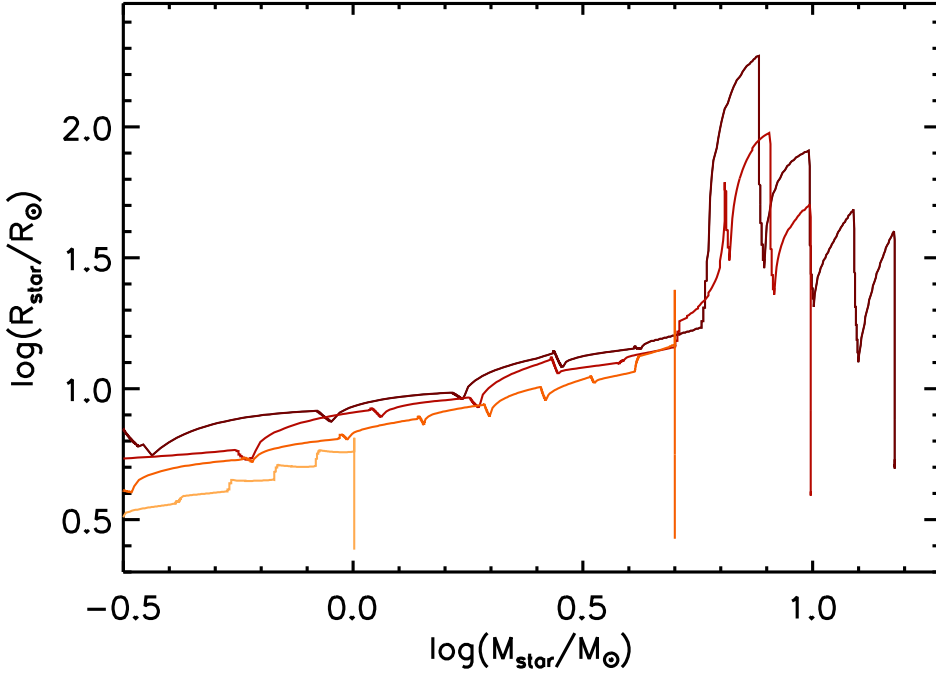


FIGURE 4.32: The radius as function of mass tracks for cold accelerated accretion with episodic bursts. The tracks represent stars of final masses $15M_{\odot}$, $10M_{\odot}$, $5M_{\odot}$ and, $1M_{\odot}$ respectively.

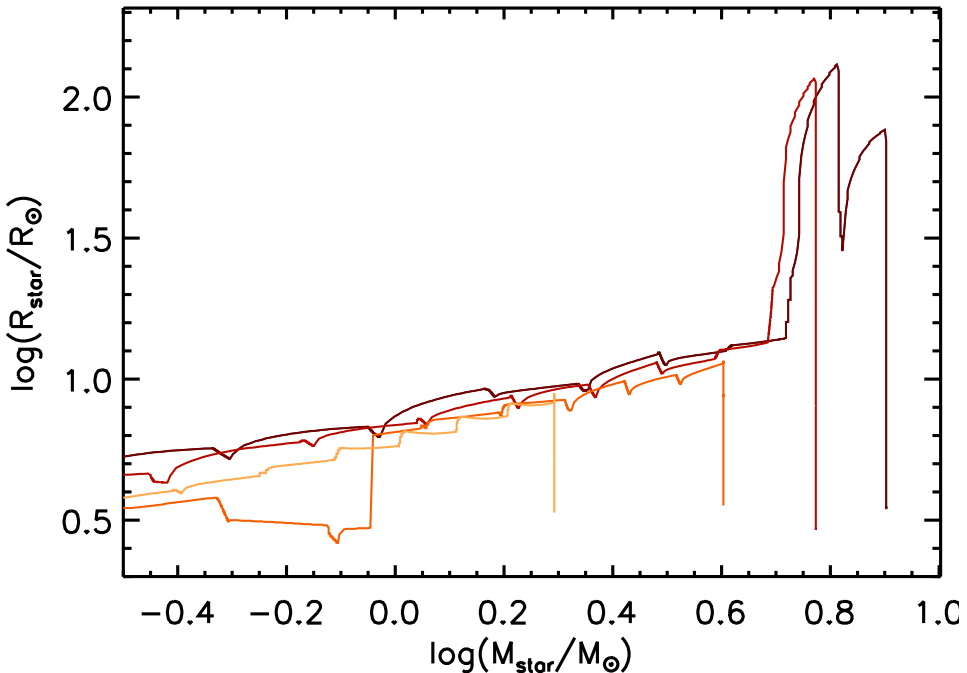


FIGURE 4.33: The radius as function of mass tracks for cold accelerated accretion with episodic bursts. The tracks represent stars of final masses $8M_{\odot}$, $6M_{\odot}$, $4M_{\odot}$ and, $2M_{\odot}$ respectively.

Exponential Model

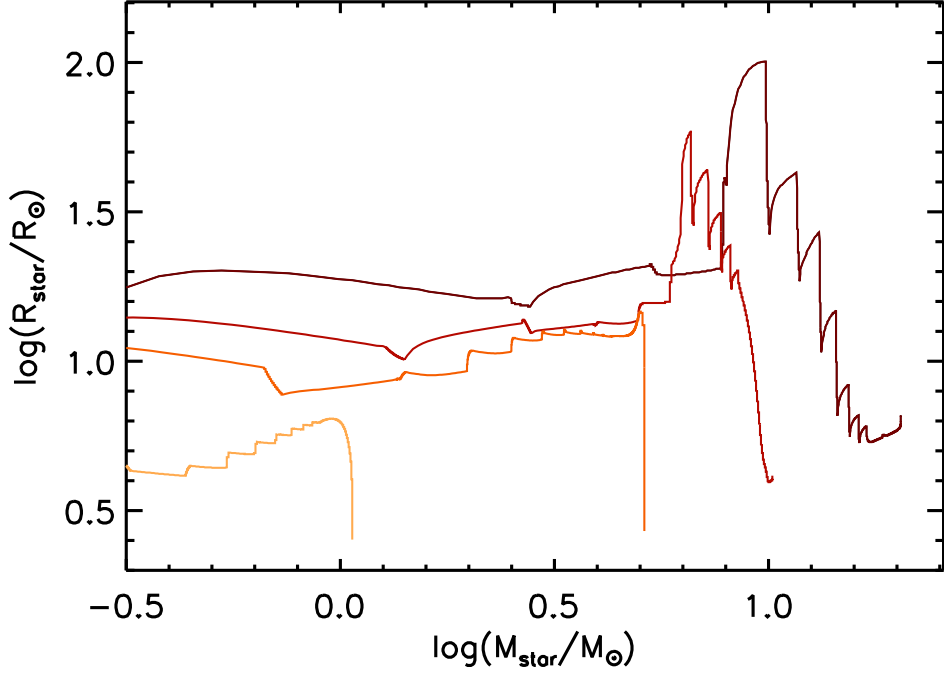


FIGURE 4.34: The radius as function of mass tracks for cold exponential accretion with episodic bursts. The tracks represent stars of final masses $20M_{\odot}$, $10M_{\odot}$, $5M_{\odot}$ and, $1M_{\odot}$ respectively.

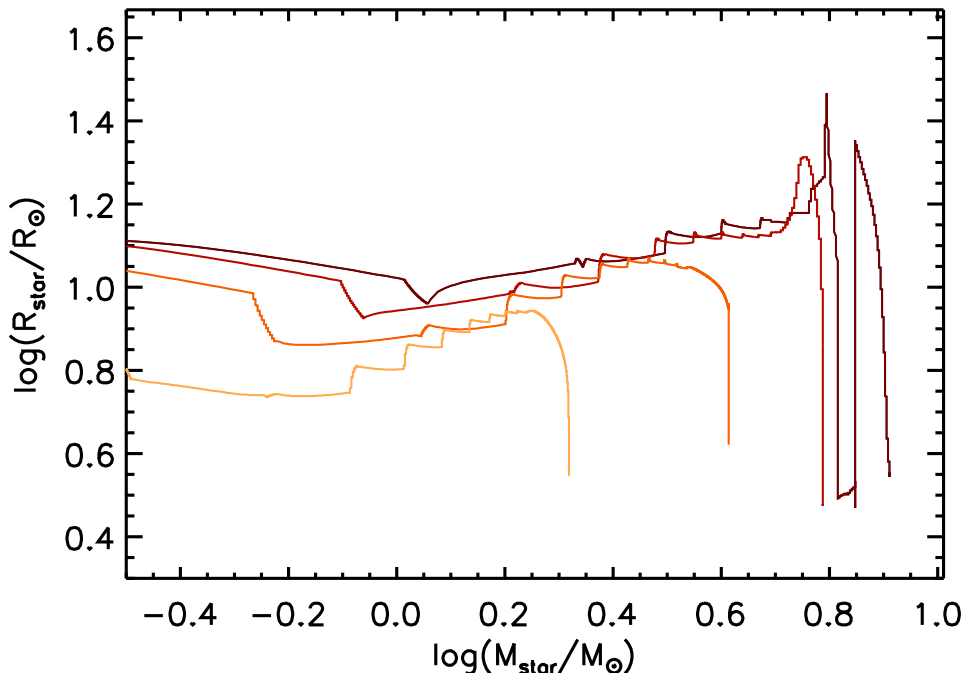


FIGURE 4.35: The radius as function of mass tracks for cold exponential accretion with episodic bursts. The tracks represent stars of final masses $8M_{\odot}$, $6M_{\odot}$, $4M_{\odot}$ and, $2M_{\odot}$ respectively.

Power Law Model

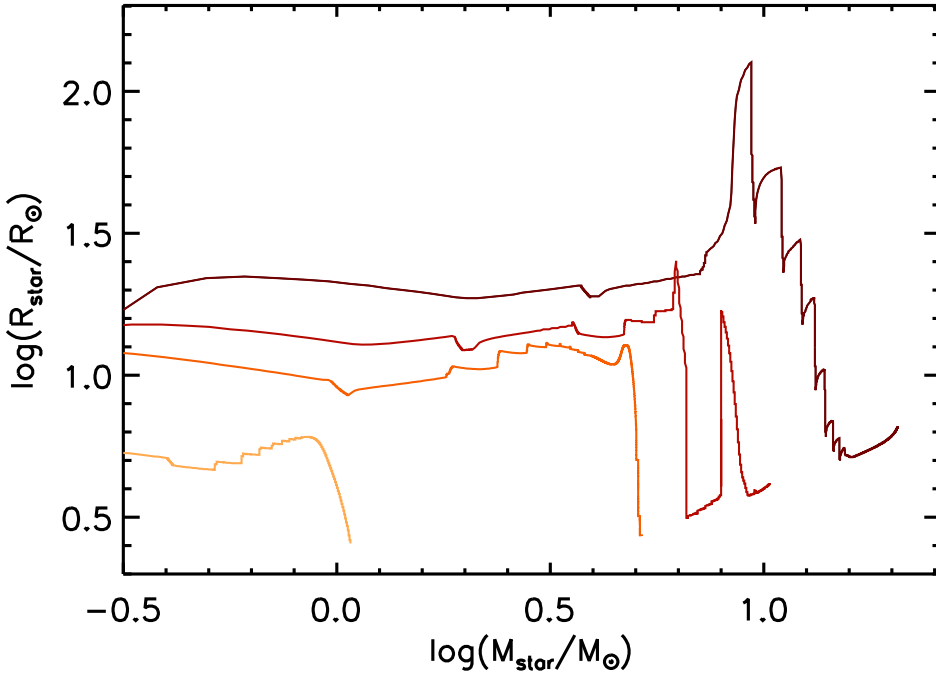


FIGURE 4.36: The radius as function of mass tracks for cold exponential accretion with episodic bursts. The tracks represent stars of final masses $20M_{\odot}$, $10M_{\odot}$, $5M_{\odot}$ and, $1M_{\odot}$ respectively.

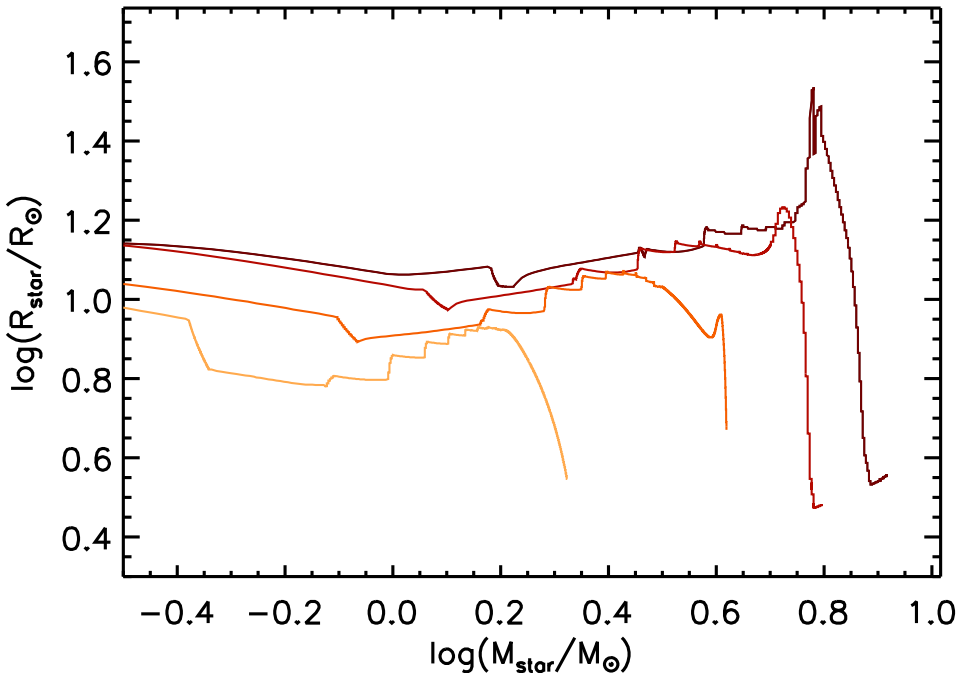


FIGURE 4.37: The radius as function of mass tracks for cold exponential accretion with episodic bursts. The tracks represent stars of final masses $8M_{\odot}$, $6M_{\odot}$, $4M_{\odot}$ and, $2M_{\odot}$ respectively.

4.4.2 Episodal theoretical H-R

We post the tracks (Figures 4.38 to 4.45) as individual results as the complex tracks become hard to distinguish if grouped. During the burst phases the luminosity drastically increases then subsides after the burst phases ends. Due to the short time scale in which these events occur, there is large overlaps in the tracks produced. Thus, the episodic bursts are harder to interpret in graphical form.

4.4.3 Constant Accretion

This section shows the resultant H-R tracks for the constant accretion model.

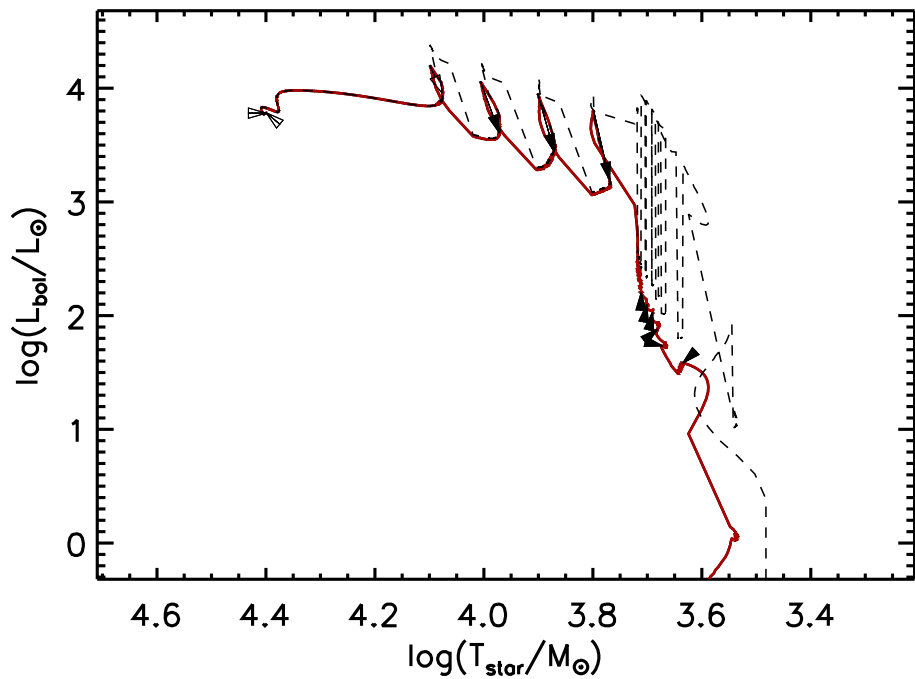


FIGURE 4.38: The H-R track for a star of $10M_{\odot}$ final mass using the cold constant accretion method with bursts. The dashed line represents the total luminosity and the solid coloured line represents the core luminosity.

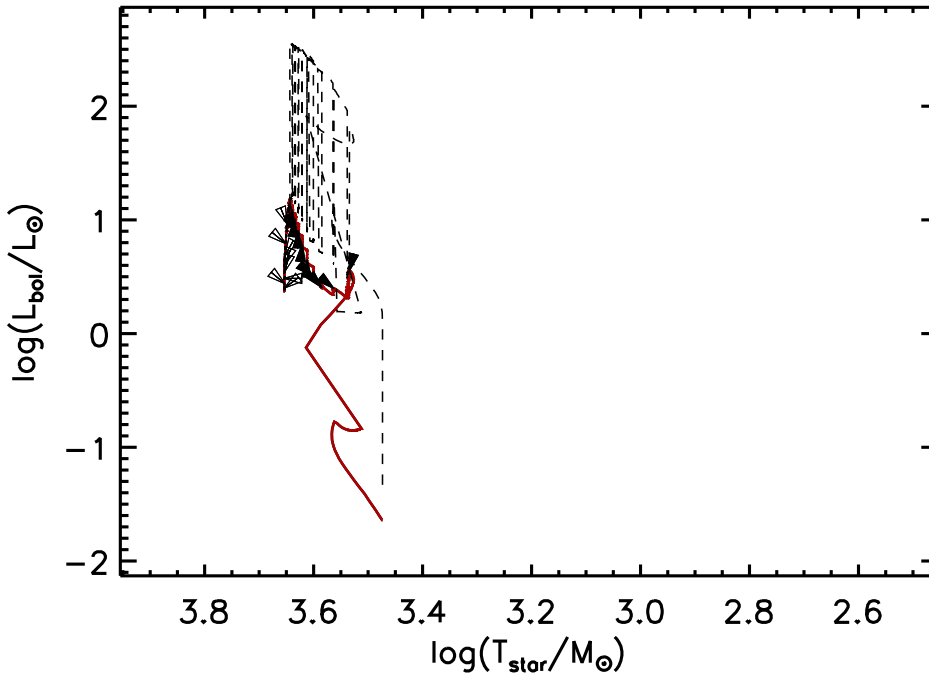


FIGURE 4.39: The H-R track for a star of $1M_{\odot}$ final mass using the cold constant accretion method including bursts. The dashed line represents the total luminosity and the solid coloured line represents the core luminosity.

4.4.4 Accelerated Accretion

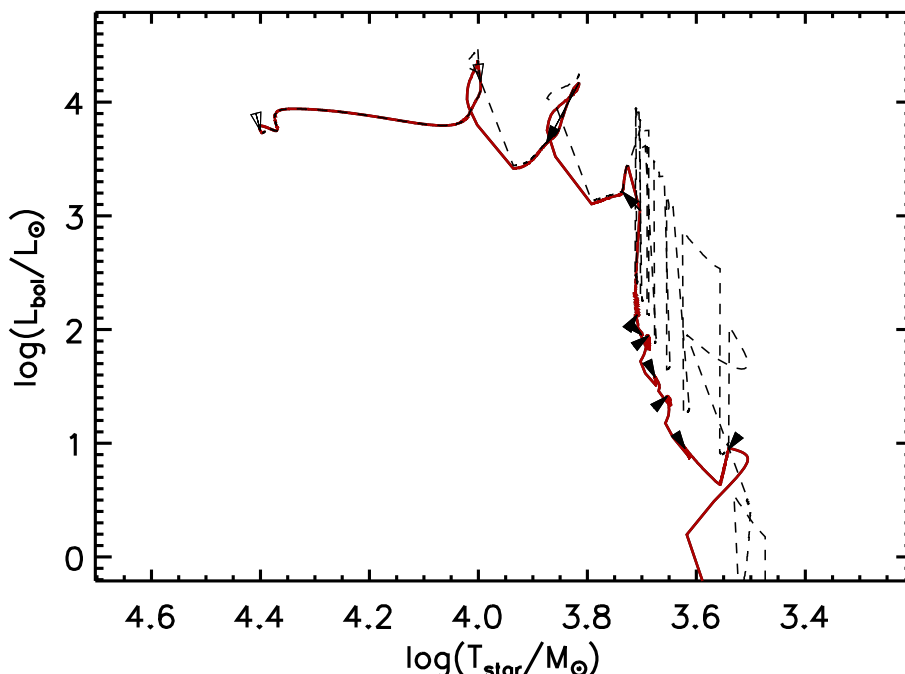


FIGURE 4.40: The H-R track for a star of $10M_{\odot}$ final mass using the cold accelerated accretion method including bursts. The dashed line represents the total luminosity and the solid coloured line represents the core luminosity.

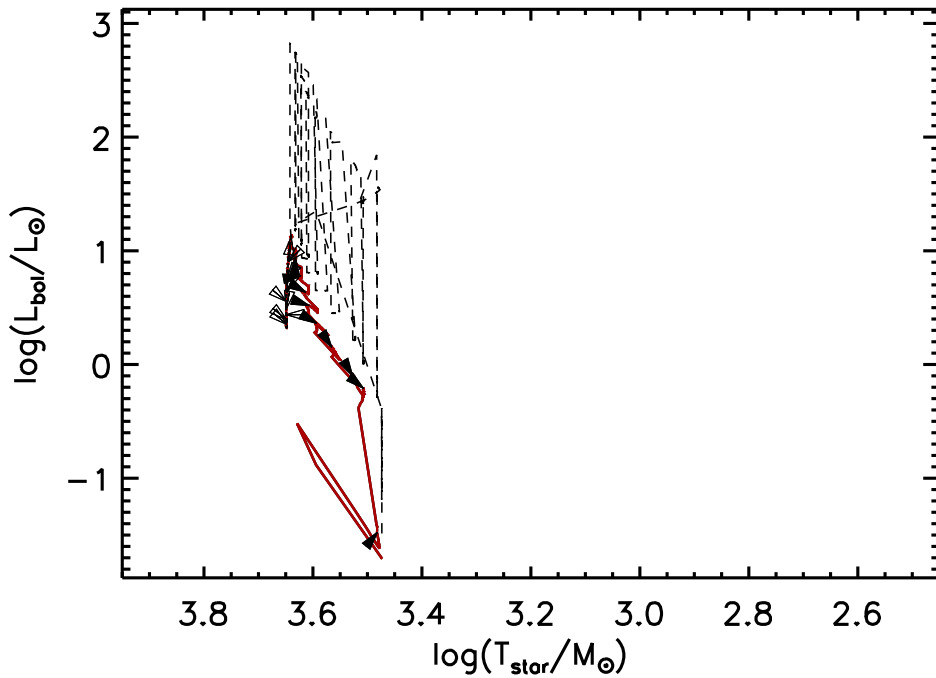


FIGURE 4.41: The H-R track for a star of $1M_{\odot}$ final mass using the cold accelerated accretion method including bursts. The dashed line represents the total luminosity and the solid coloured line represents the core luminosity.

4.4.5 Exponential Accretion

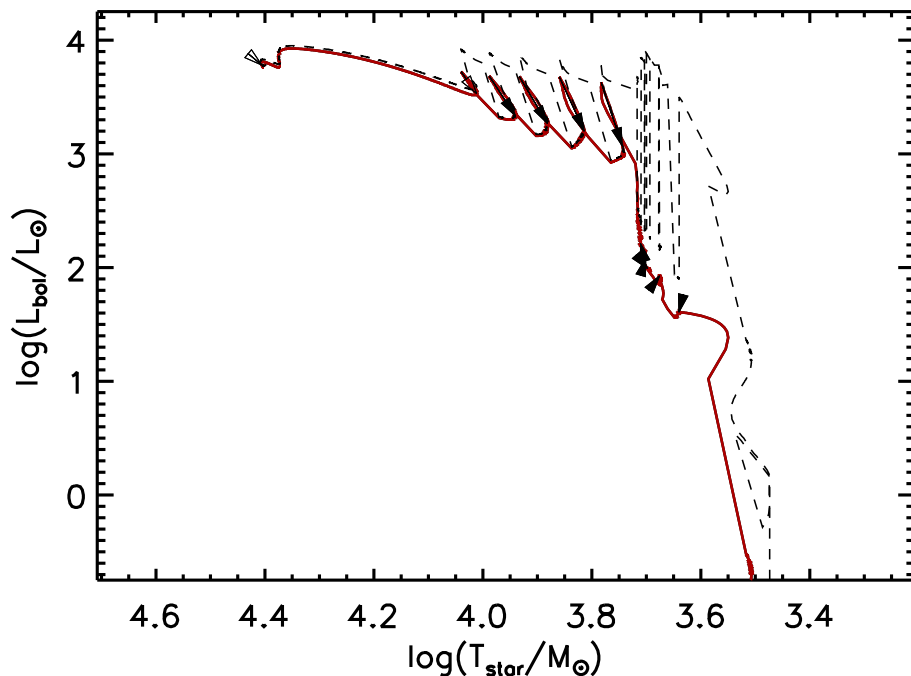


FIGURE 4.42: The H-R track for a star of $10M_{\odot}$ final mass using the cold exponential accretion method.

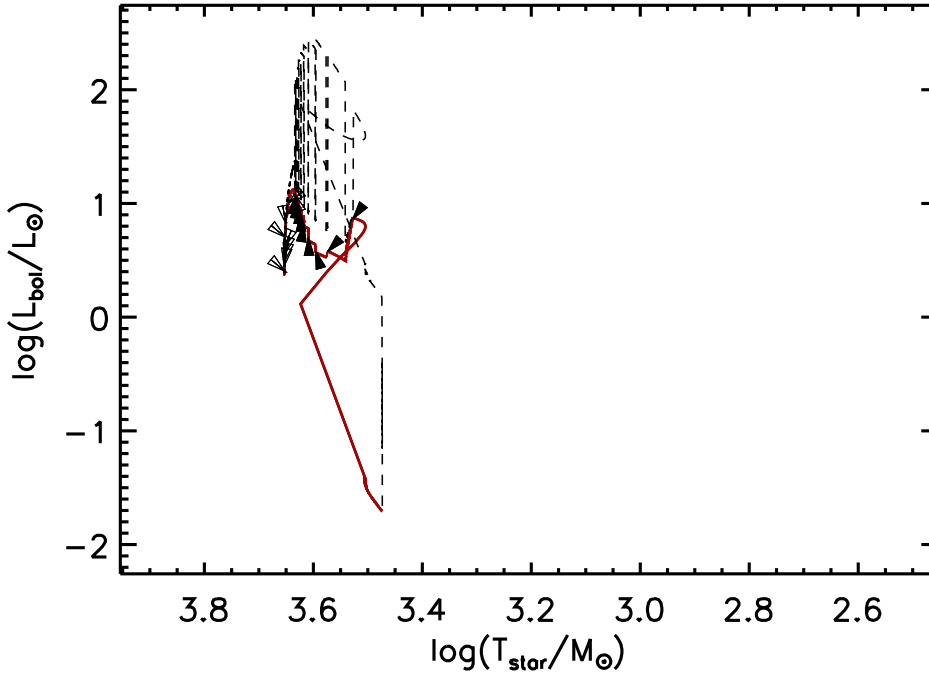


FIGURE 4.43: The H-R track for a star of $1M_{\odot}$ final mass using the cold exponential accretion method including bursts. The dashed line represents the total luminosity and the solid coloured line represents the core luminosity.

4.4.6 Power Law Accretion

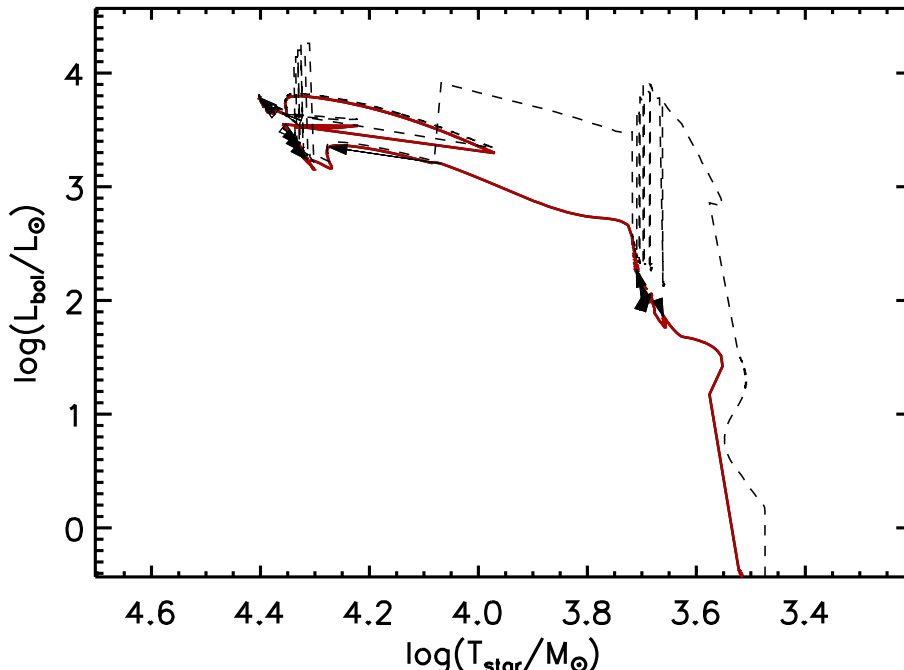


FIGURE 4.44: The H-R track for a star of $10M_{\odot}$ final mass using the cold power law accretion method including bursts. The dashed line represents the total luminosity and the solid coloured line represents the core luminosity.

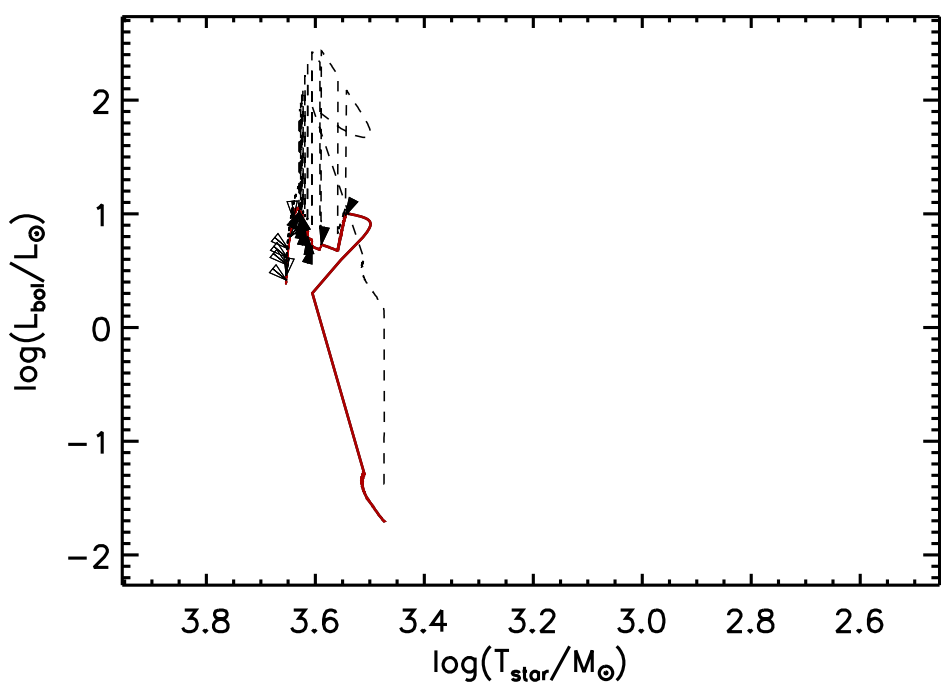


FIGURE 4.45: The H-R track for a star of $1M_{\odot}$ final mass using the cold power law accretion method.

4.4.7 Mass luminosity

Again, we plot the clump luminosity as function of clump mass alongside the ATLASGAL data. The dashed lines again represent fixed values of Mass-Luminosity at ratios of 0.1, 1, 10 and 100, from dark blue to light blue respectively.

Constant Accretion

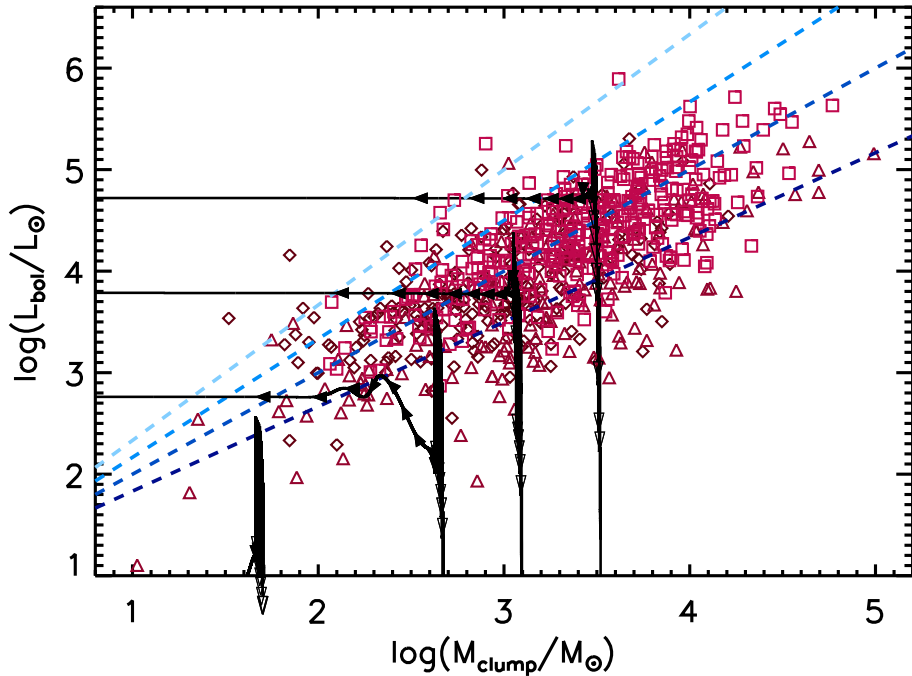


FIGURE 4.46: The Mass Luminosity tracks using the cold constant accretion method. The final masses of the stars associated with tracks from left to right, $1M_{\odot}$, $5M_{\odot}$, $10M_{\odot}$, $20M_{\odot}$.

Accelerated Accretion

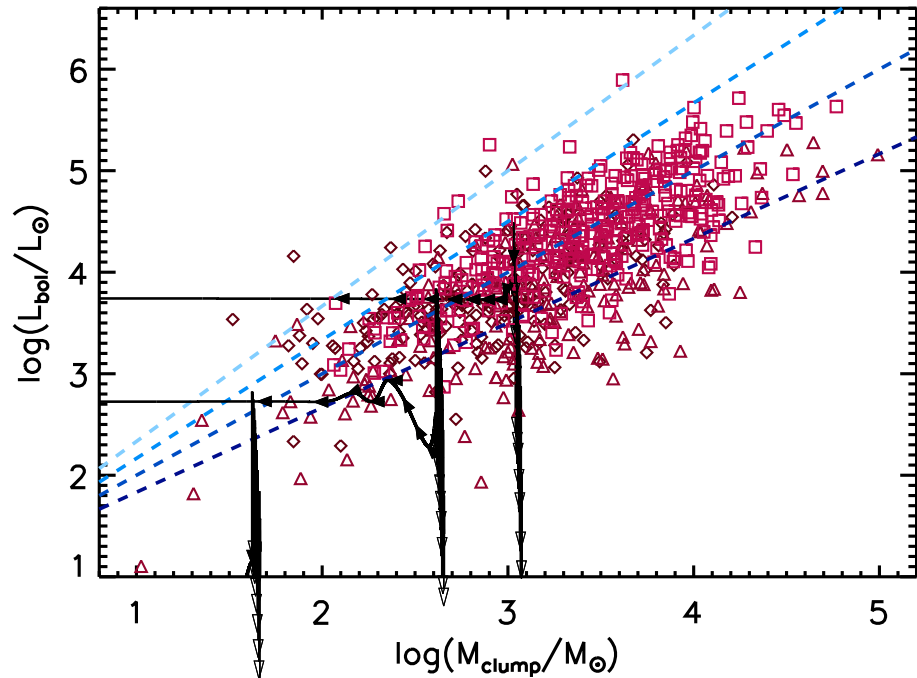


FIGURE 4.47: The Mass Luminosity tracks using the cold accelerated accretion method. The final masses of the stars associated with tracks from left to right, $1M_{\odot}, 5M_{\odot}, 10M_{\odot}$. §

Exponential Accretion

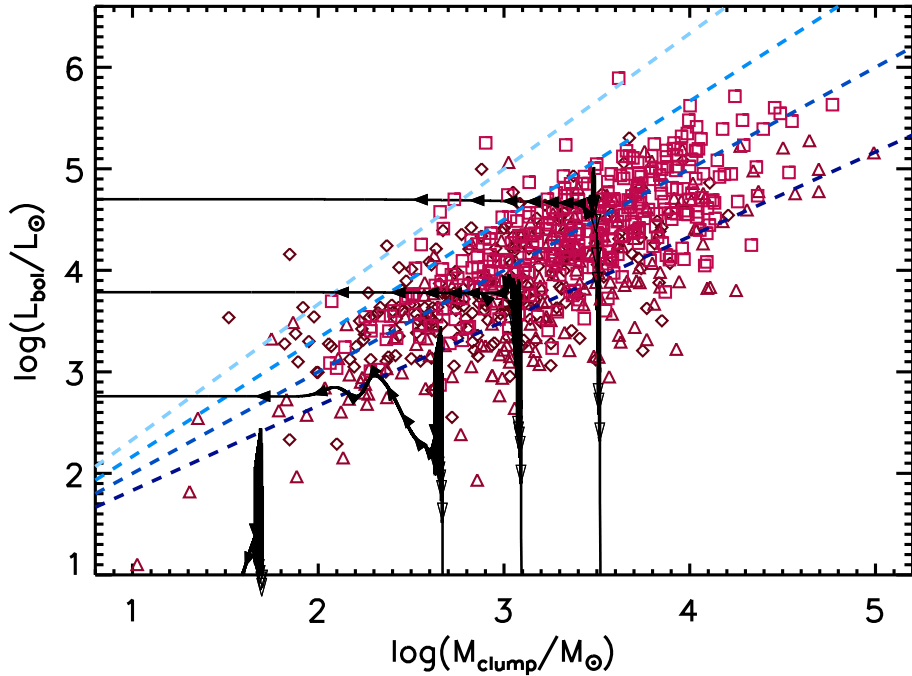


FIGURE 4.48: The Mass Luminosity tracks using the cold exponential accretion method. The final masses of the stars associated with tracks from left to right, $1M_{\odot}$, $5M_{\odot}$, $10M_{\odot}$, $20M_{\odot}$.

4.4.8 PowerLaw Accretion

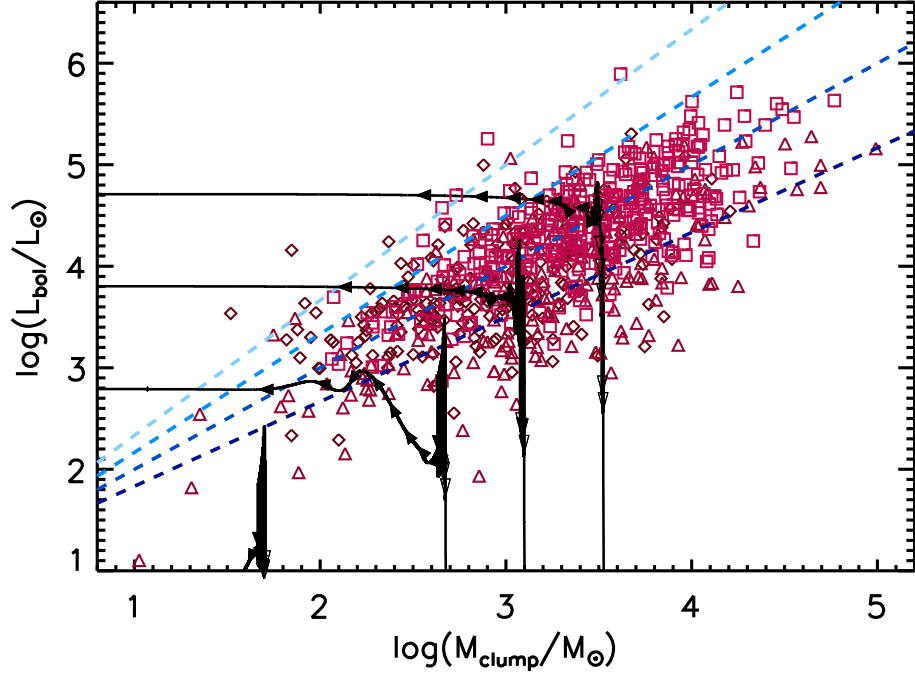


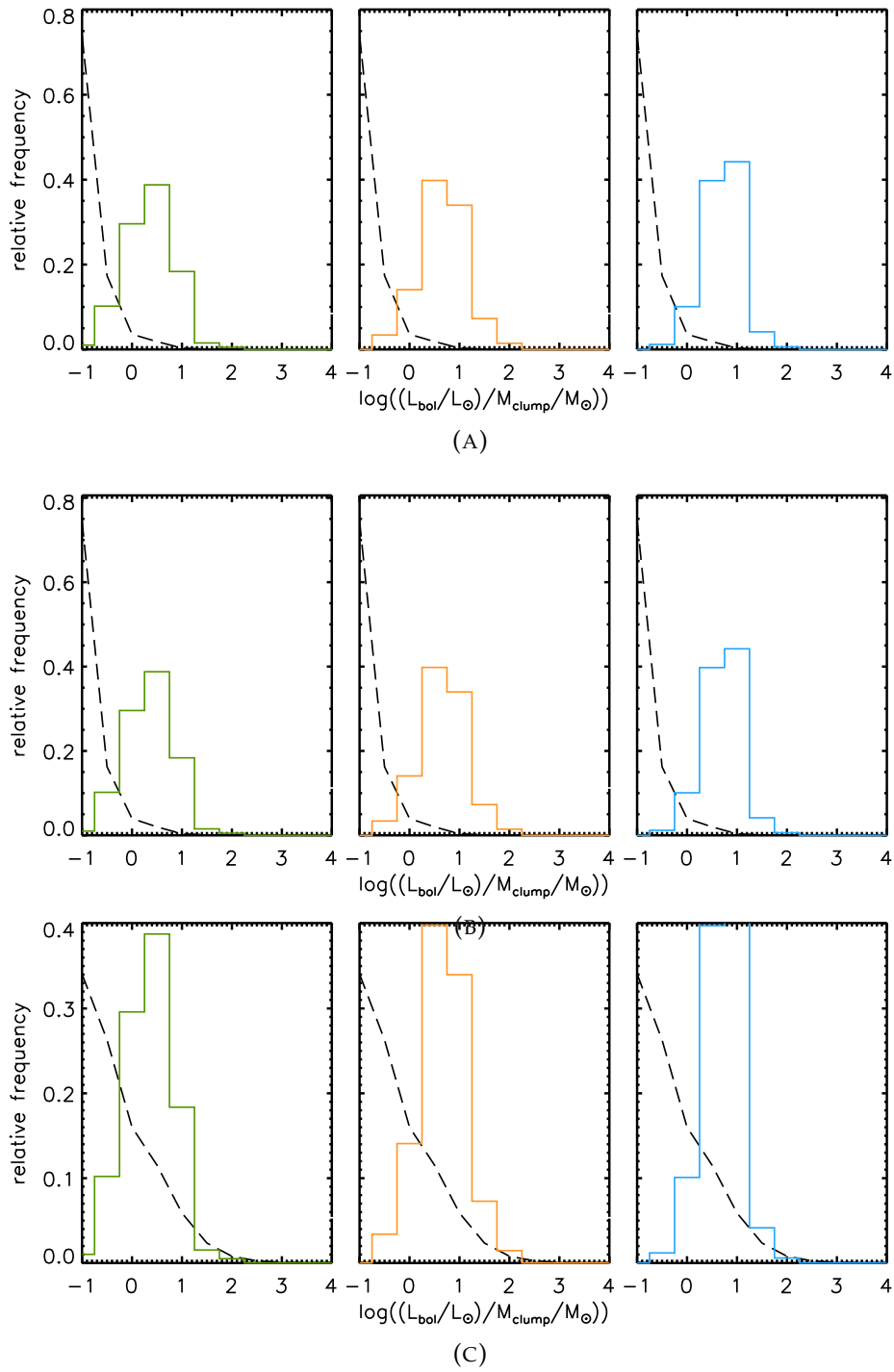
FIGURE 4.49: The tracks for clump luminosity as a function of clump mass using the cold power law accretion method. The final masses of the stars associated with tracks from left to right, $1M_{\odot}$, $5M_{\odot}$, $10M_{\odot}$, $20M_{\odot}$.

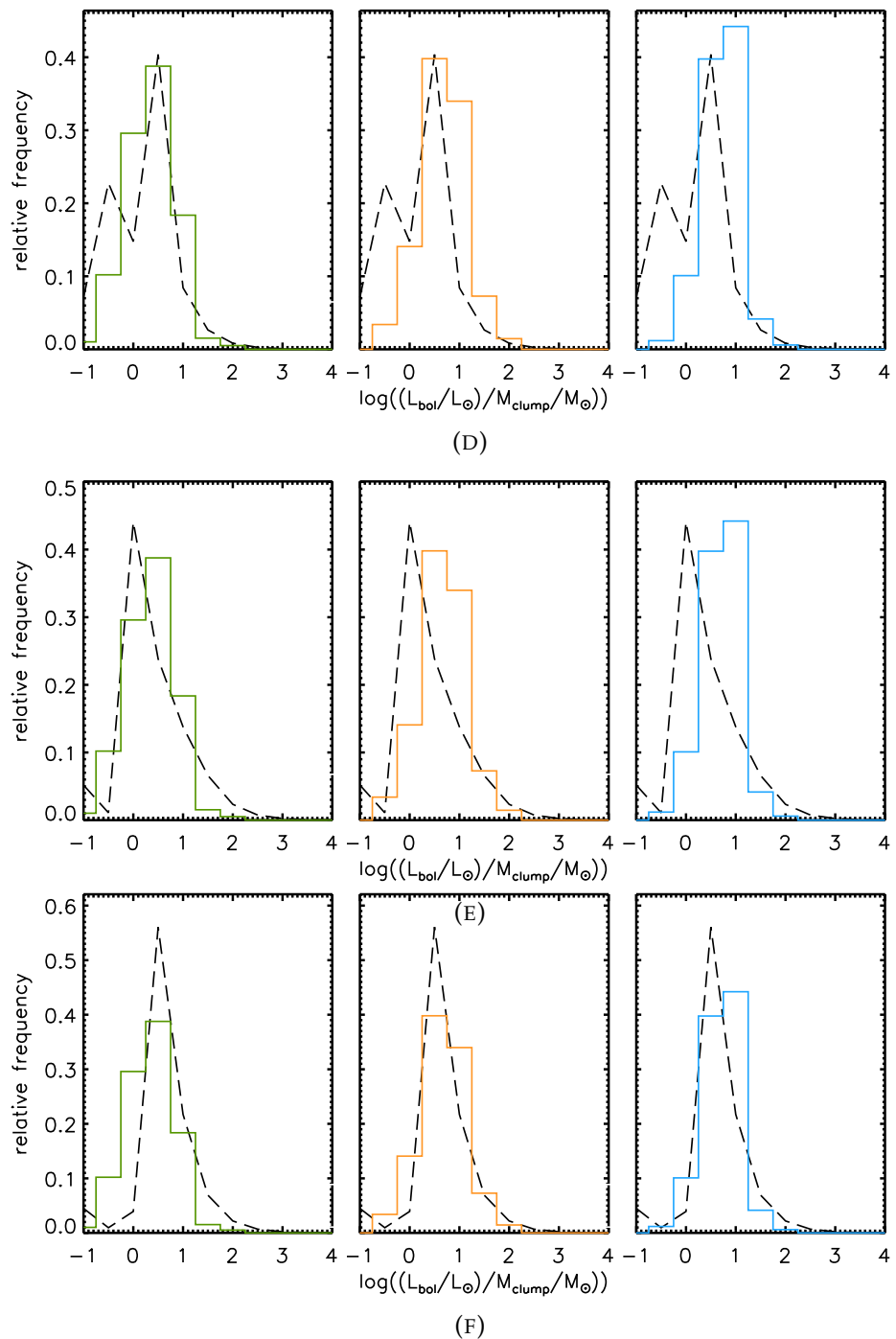
4.4.9 Luminosity-to-Mass Ratio Distribution

This section follows the same layout as the non-episodic models luminosity-to-mass section, but using the episodic burst models. It is important to notice how minimal the differences of the smooth and burst accretion methods; very similar distribution curves but the burst methods showing slightly greater frequencies in the greater luminosity mass ratio bins. This is more noticeable in the lower final mass models.

Constant

FIGURE 4.50: All Constant Burst Distribution Results





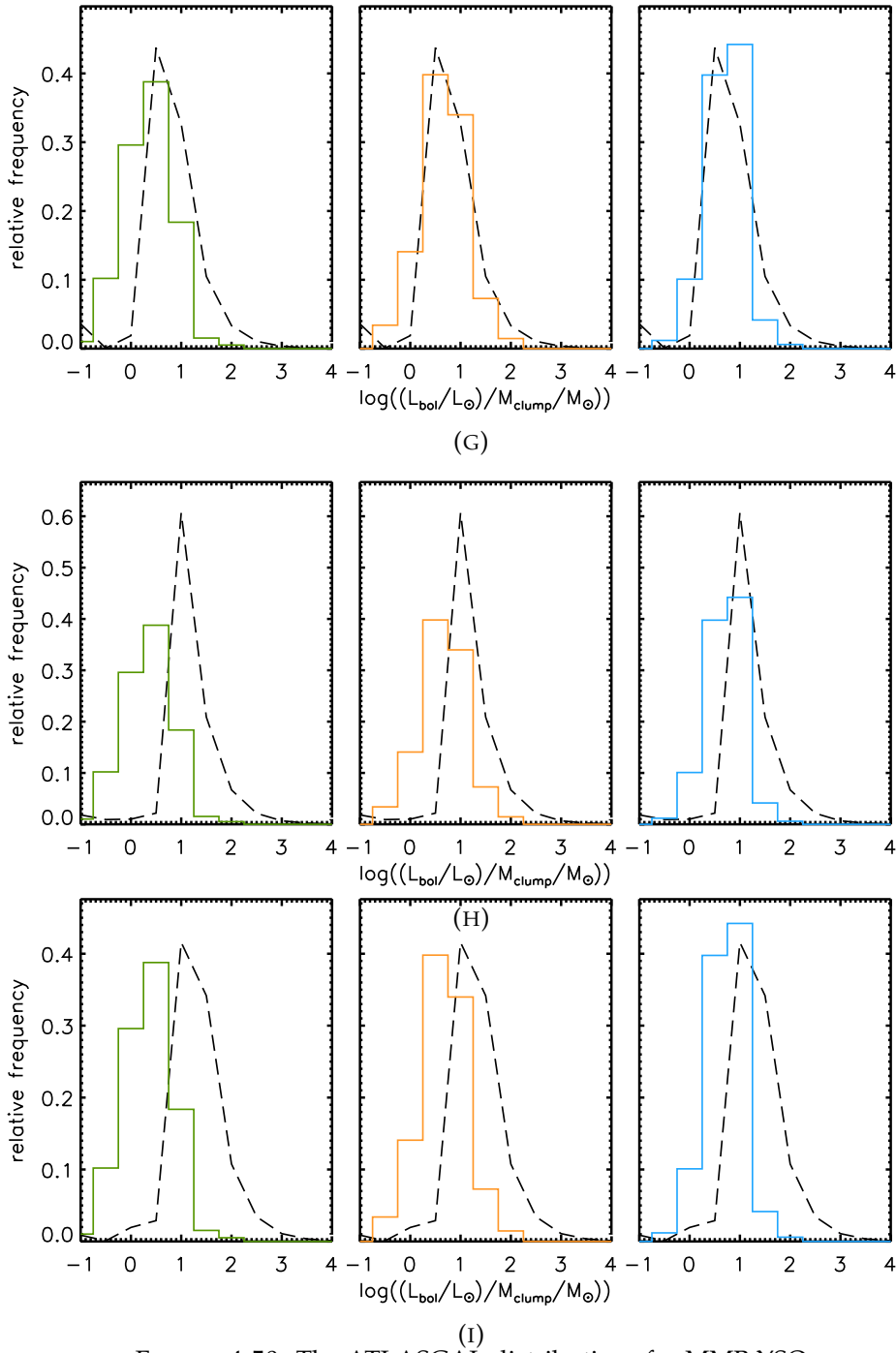
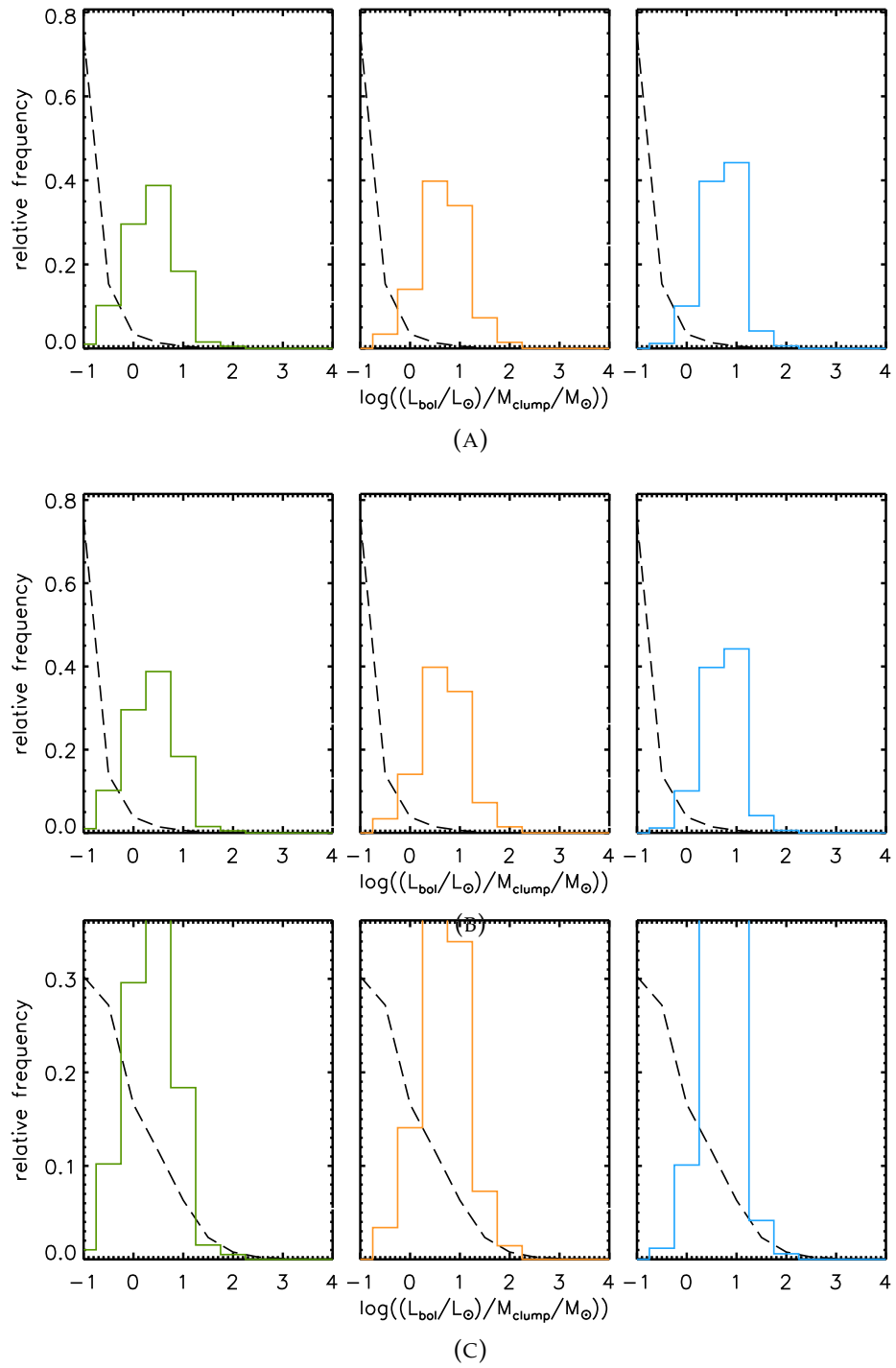
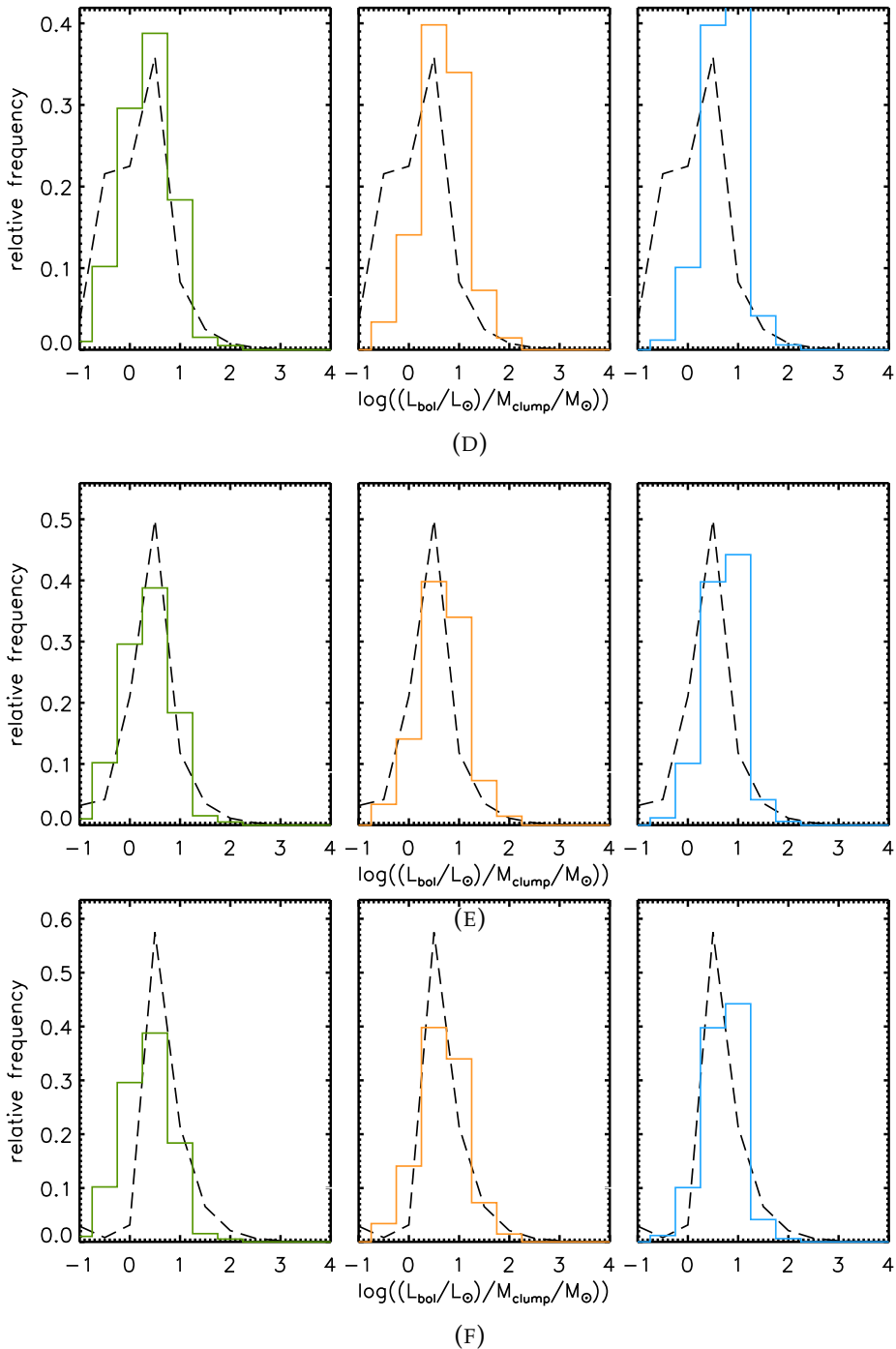


FIGURE 4.50: The ATLASGAL distributions for MMB YSO and HII object types for the left, central and right column respectively. The dashed lines on plots A,B,C,D,E,F,G,H,I represent star of final masses 1, 2, 4, 5, 6, 8, 10, 15 and, $20M_{\odot}$ respectively, using the constant accretion method including episodic bursts.

Accelerated

FIGURE 4.51: All Accelerated Burst Distribution Results





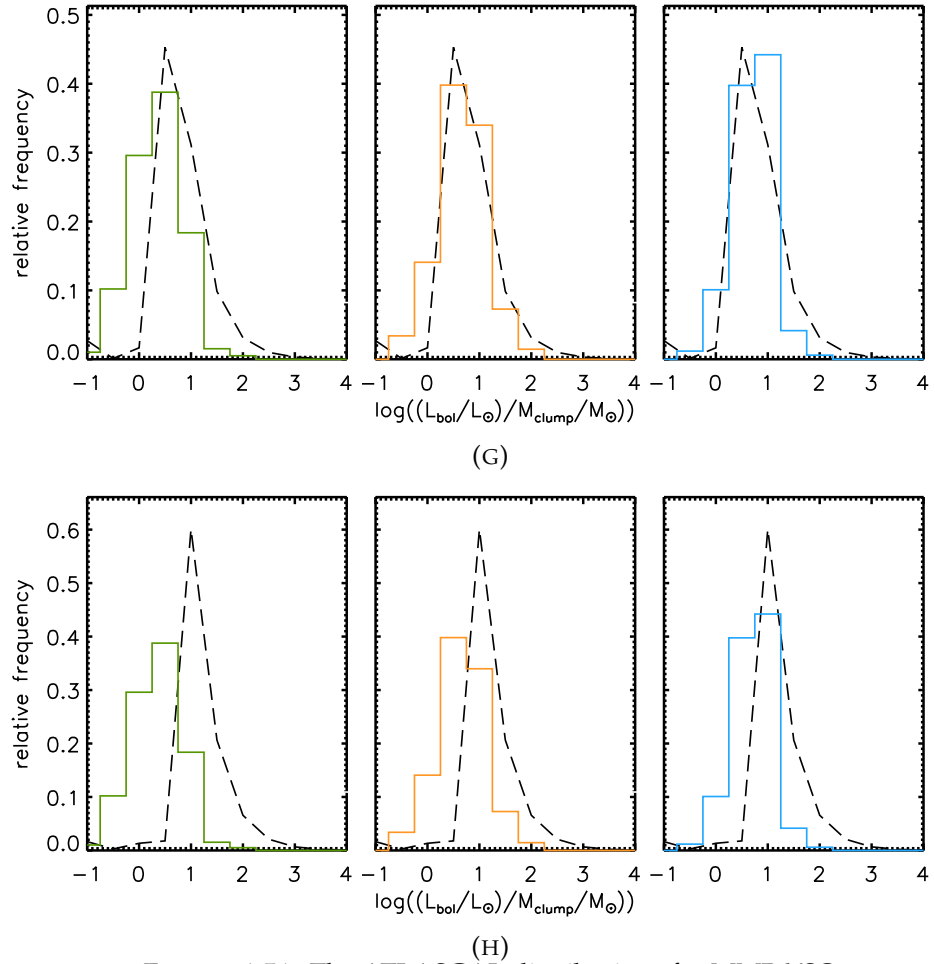
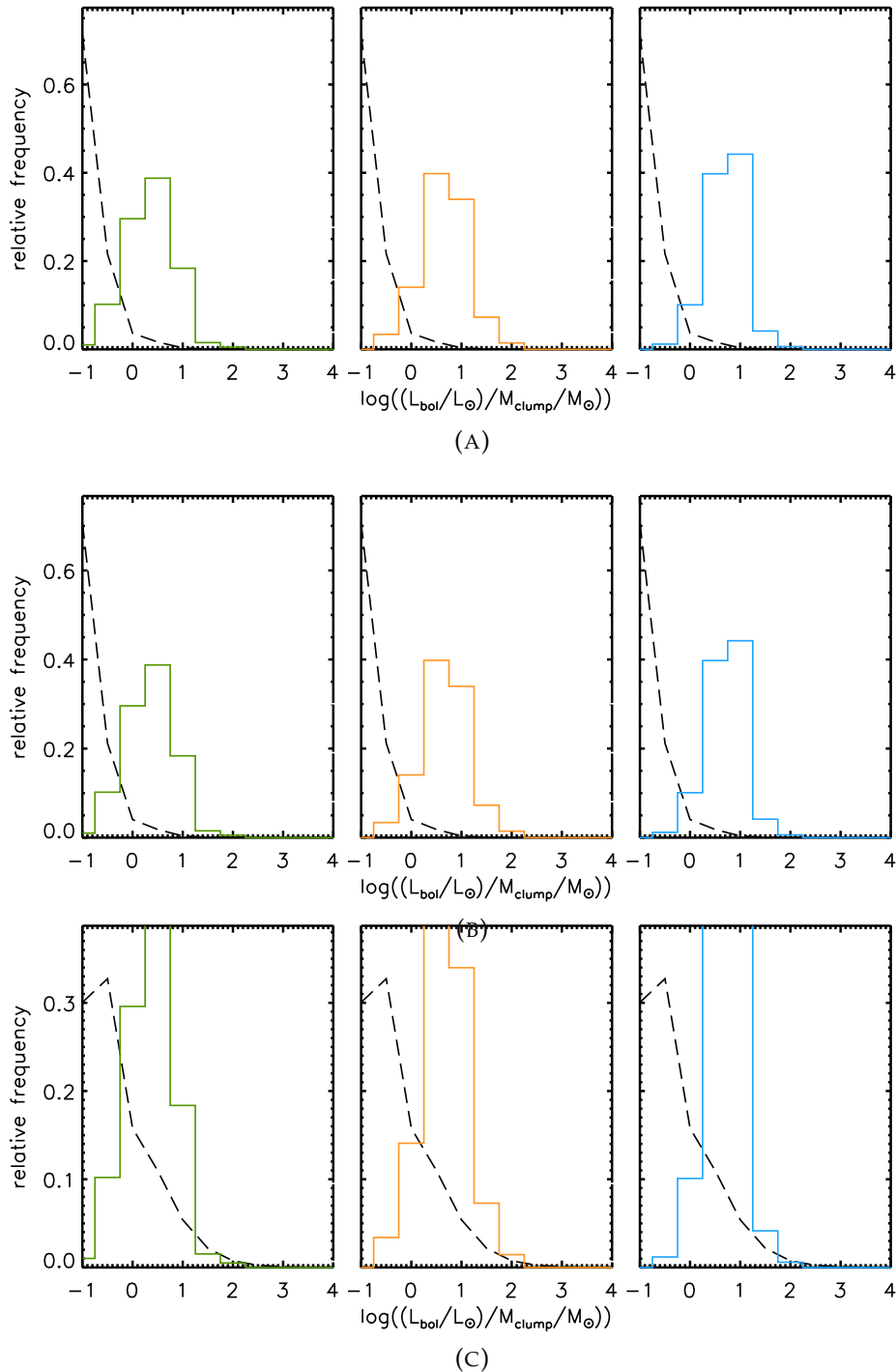
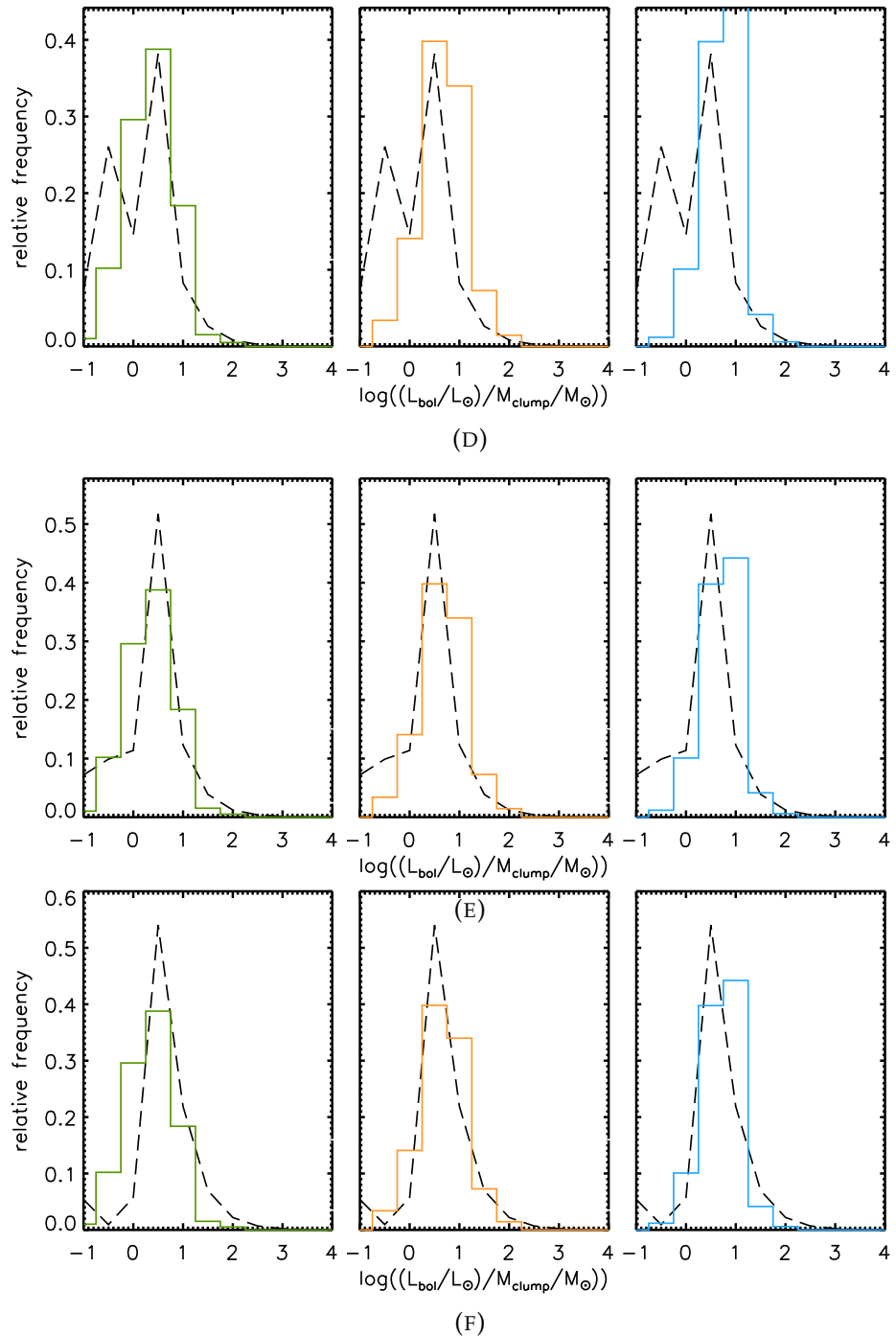


FIGURE 4.51: The ATLASGAL distributions for MMB YSO and HII object types for the left, central and right column respectively. The dashed lines on plots A,B,C,D,E,F,G,H represent star of final masses $1, 2, 4, 5, 6, 8, 10$ and $15 M_{\odot}$ respectively, using the accelerated accretion method including episodic bursts.

Exponential

FIGURE 4.52: All Exponential Burst Distribution Results





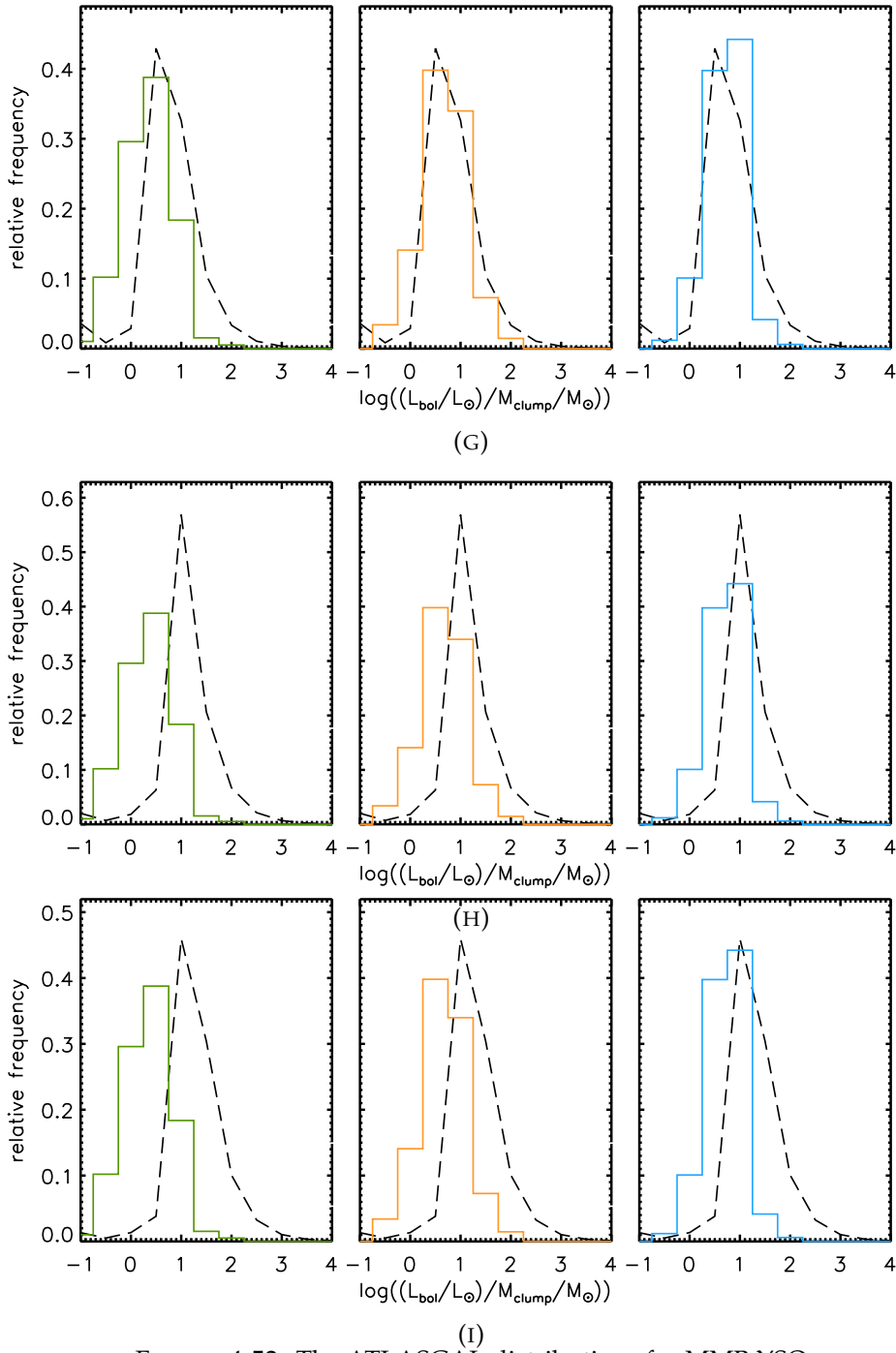
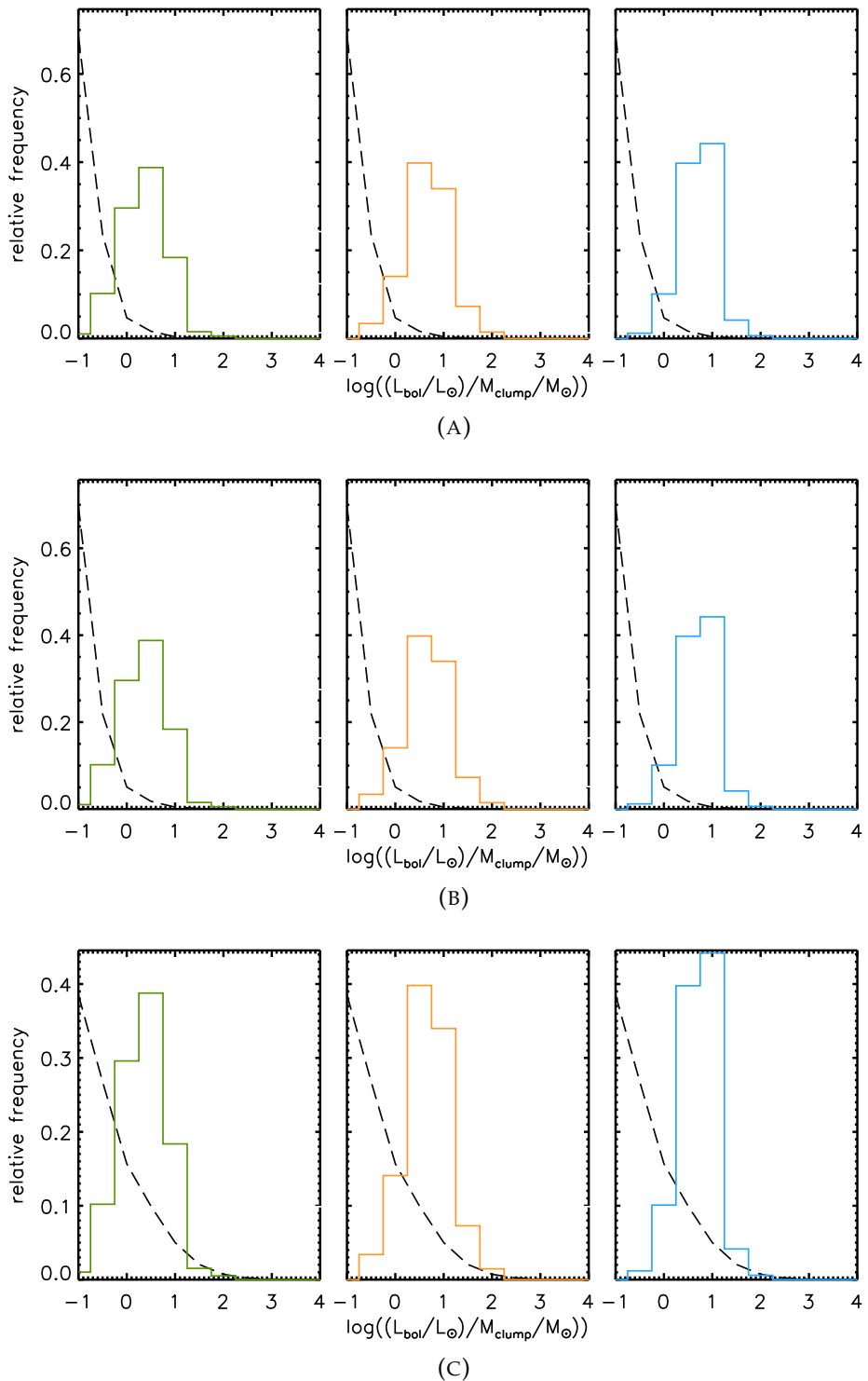
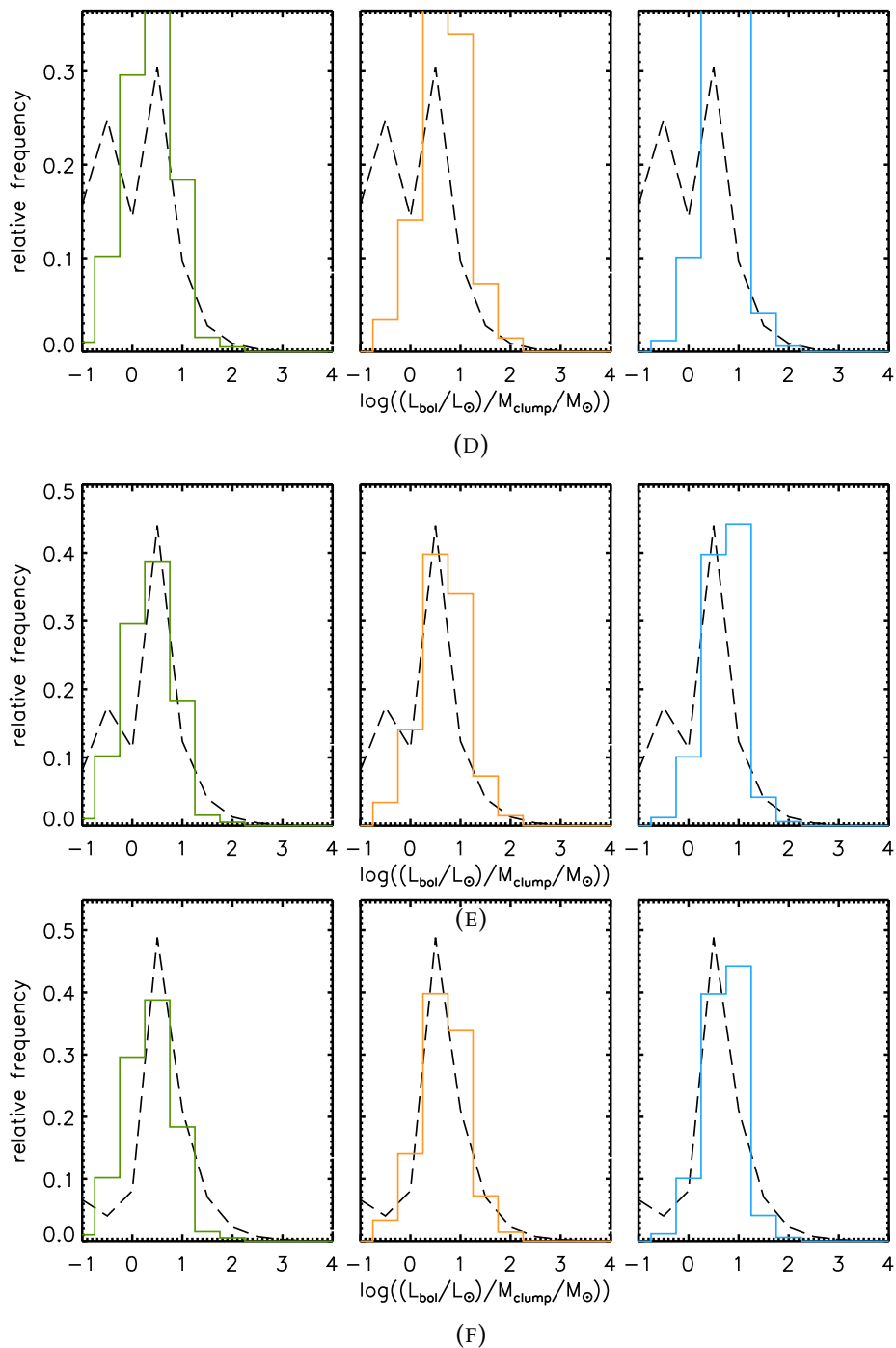


FIGURE 4.52: The ATLASGAL distributions for MMB YSO and HII object types for the left, central and right column respectively. The dashed lines on plots A,B,C,D,E,F,G,H,I represent star of final masses 1, 2, 4, 5, 6, 8, 10, 15 and, $20M_{\odot}$ respectively, using the exponential accretion method including episodic bursts.

Power Law

FIGURE 4.53: All Power law distribution results





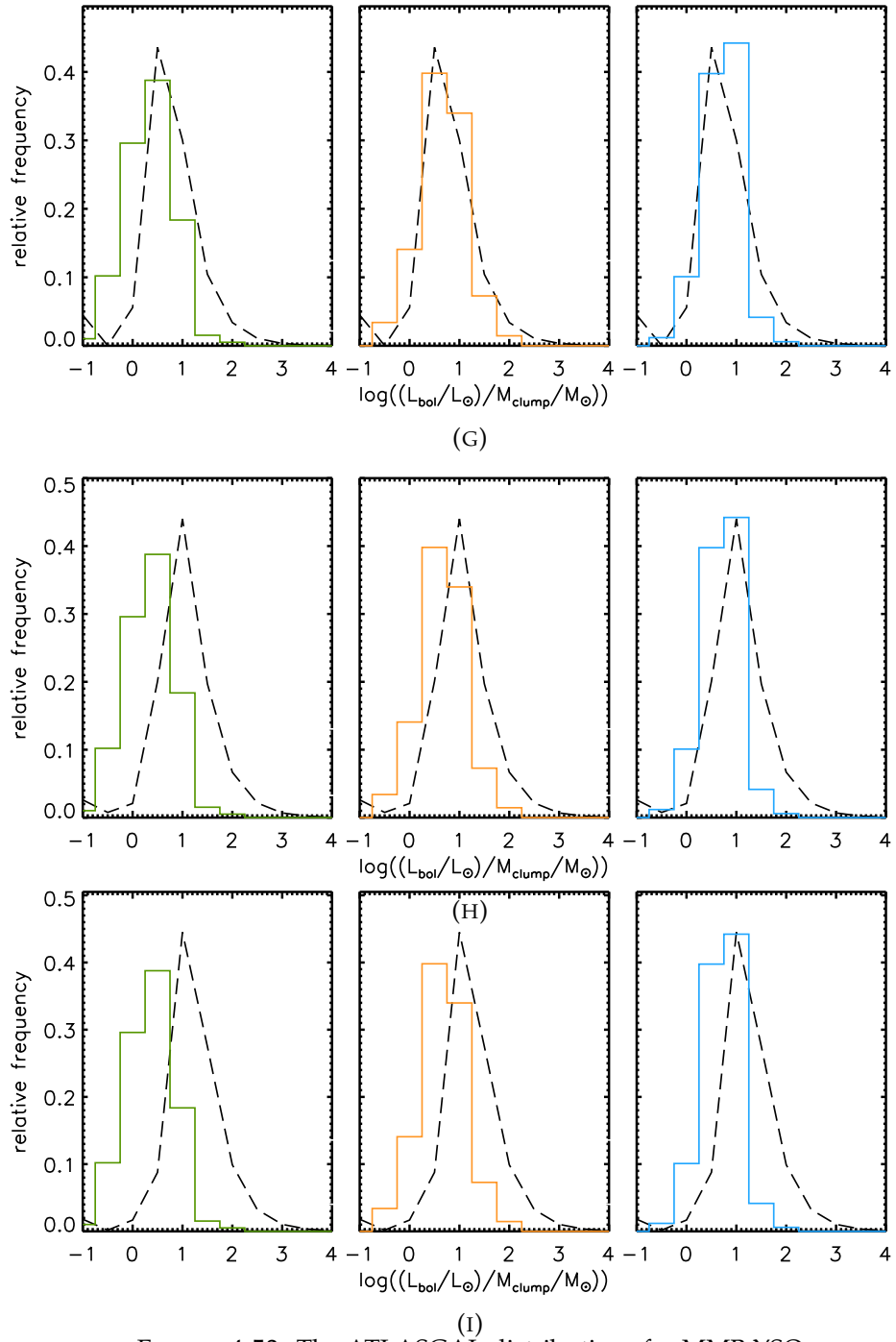


FIGURE 4.53: The ATLASGAL distributions for MMB YSO and HII object types for the left, central and right column respectively. The dashed lines on plots A,B,C,D,E,F,G,H,I represent star of final masses 1, 2, 4, 5, 6, 8, 10, 15 and, $20M_{\odot}$ respectively, using the power law accretion method including episodic bursts.

Chapter 5

Discussion

Which accretion model is most consistent with observational data? This question is hard to answer because of the differences between reality and the isolated single star scenario in this thesis. However, we can still try to find significant data points, such as the model that has a greatest swelling radius and/or greatest peak luminosity. By mapping these as reference points we can determine if there is correlation with observation.

We recognise that protostellar accretion can collapse, or end, at any stage if the mass supply is cut off. As such we must posit the question of the effects of rapid shutoff during a key phase of the evolution. Does the result of cutoff during the swelling or contraction phase lead to significant differences in tracks or other indicators such as spectral signature.

Whilst the model we use is more advanced than the likes of classic isothermal collapse, it is not fully inclusive of new research into star forming environments. More recent findings have shown giant molecular clouds tend to have long reaching, roughly cylindrical, arms that mass will flow along, with protostars and their clump flowing too. As such the filaments feed the clumps and the clumps feed the protostar, this dynamic process will significantly change the gravity, density and opacity of the protostellar clump. As such a higher mass star at an instantaneous point in time would be forming from a lower mass clump than our model suggests. So we must address the issue, is static spherical modelling a good enough representation of star formation?

Does a single base accretion rate apply throughout the entire protostellar evolution phase? Do protostars accrete mass using just one method, for all stages of evolution? We understand that stars form in dynamic regions,

where the current state of the protostar will give varying effects on its surroundings through the use of radiative feedback and jets, then we must also question if these effects can have a large enough impact on the envelope as to change the accretion rate. Is the space-time grid in our model large enough to encapsulate the extent of protostellar feedback?.

5.1 Hydrodynamic code

Before discussing the different observations and results of our model, we must first discuss what is feasible to be within the code and its limits. The STELLAR code was found to be fairly fragile, often failing at the intersections of accretions rates. The cause being the large changes of internal structure that occur with a change in energy input. If the number of Henyey iterations allowed within the code was increased and the minimum internal time step increment decreased, it is likely that the code would find convergence and continue without failing. This was not pursued as it would largely increase total program run time, especially when using the burst model, as such did not fit in the time frame of this thesis.

As briefly mentioned earlier; the older Fortran 77 code is limited in its functionality, for instance evaluating complex integrals is not easily possible, such as solving the gamma function involved with the power law model. An update to a modern version of Fortran (90, 95, 2003 etc) would allow access to a wider range of libraries and improved functionality, which in turn could simplify the whole process of experimental testing. The added ability to include complex functions would also be useful and could help achieve more accurate results. Whilst conversion would be a cumbersome task the added benefit is likely to be worth making the change.

STELLAR is a spherically symmetric hydrodynamic code, in which it models a quartered section of the stellar space and then uses the axial symmetry to give a complete image. This may remove potential interactions of UV feedback (Hosokawa et al., 2016) and nonaxisymmetric clouds (Vorobyov et al., 2013). An approach such as that found in Hosokawa et al. (2016), whereby using the STELLAR code alongside a three dimensional hydrodynamic radiation model is a logical step to maximising effectiveness of this

code.

5.2 General

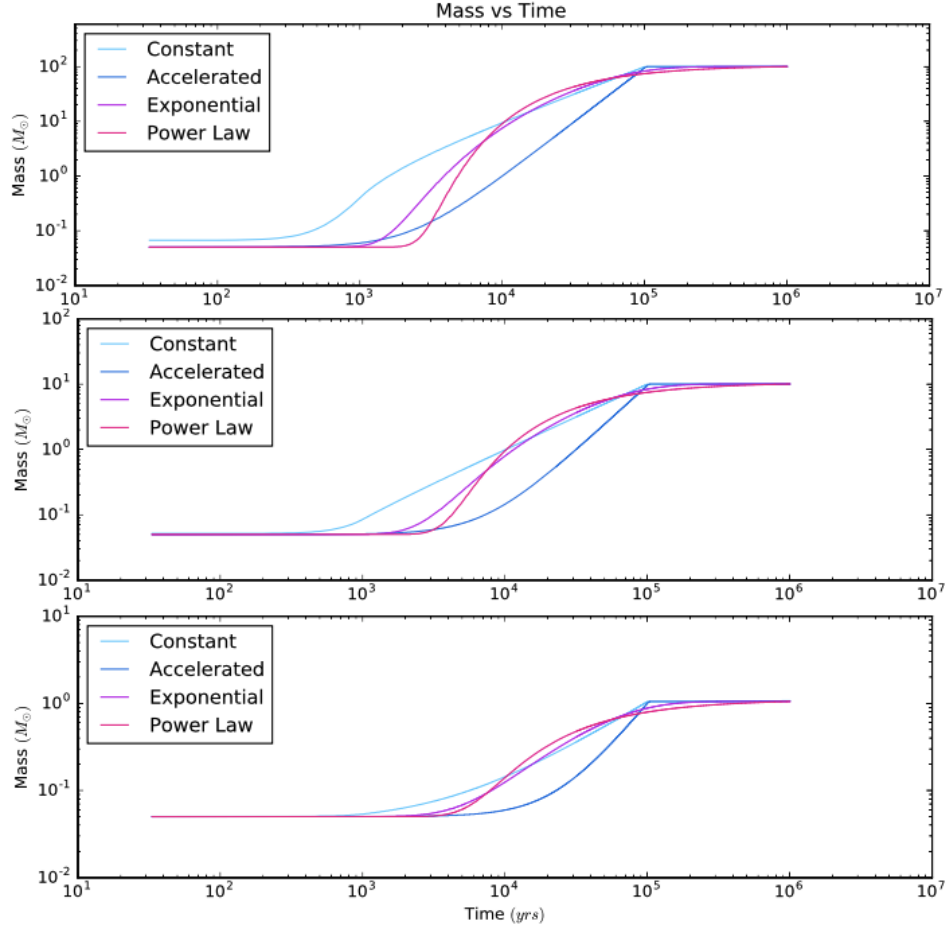


FIGURE 5.1: The four different models and the accumulated mass as a function of time. From top to bottom, the plots show the results of stars of final masses $100M_{\odot}$, $10M_{\odot}$ and, $1M_{\odot}$ respectively

Figure 5.1 displays the mass accumulation as a function of time and shows important characteristic differences between the models. The accelerated model in particular has a much lower value of stellar mass for the majority of the accretion time compared to the other three models, where the other three models accumulate most of the mass earlier in the accretion phase. This is likely the contributing factor to the differences in tracks found between the accelerated model and the others.

5.3 The Mass Radius tracks

Figures 4.1 through to 4.8 show the progressive changes in radius with the change in final mass. First noting that all models spend a large portion of the track on very similar paths, from the points of $\text{Log}(M/M_{\odot}) = -0.2$ to 0.6. Through this range, the models would be indistinguishable from each other. One exception we find is the accelerated $100M_{\odot}$ model in Figure 4.1, as previously noted this is likely to be because of the accelerated models mass accumulation being weighted toward the later stages of accretion compared to the others, as such the early stage has a much lower radius. Secondly, we note that the swelling phase begins to occur in the Exponential and Power law models around the $5 - 6M_{\odot}$ final mass (Figures 4.5 and 4.6), and the Accelerated and Constant models occurring around $6 - 8M_{\odot}$ final mass (Figure 4.4), this is due to the greater accretion rates of the exponential and power law models earlier in the evolution. It can also be seen from the same figures, that even though the accelerated models swelling phase occurs at greater masses, the peak radius is greater than the other three models for mid-range masses. These two points indicate that the swelling phase during evolution has a form of dependency upon the energy input rate, and not just the protostellar core's accumulated mass.

The $100M_{\odot}$ results (Figure 4.1), show the exponential model reaching greater peak radius than the accelerated model. If the model's greatest accretion rate and thus energy input, coincides with the beginning of the swelling phase, the result is a greater radius.

Lastly, we must note that the $100M_{\odot}$ mass stars, Figure 4.1, continue to accrete after the Kelvin Helmholtz contraction phase. With between 50 – 60% of mass being gained after the contraction stage, the track is significantly different to the lower mass models, showing evidence that, for massive stars, there is a stage between the PMS contraction and ZAMS.

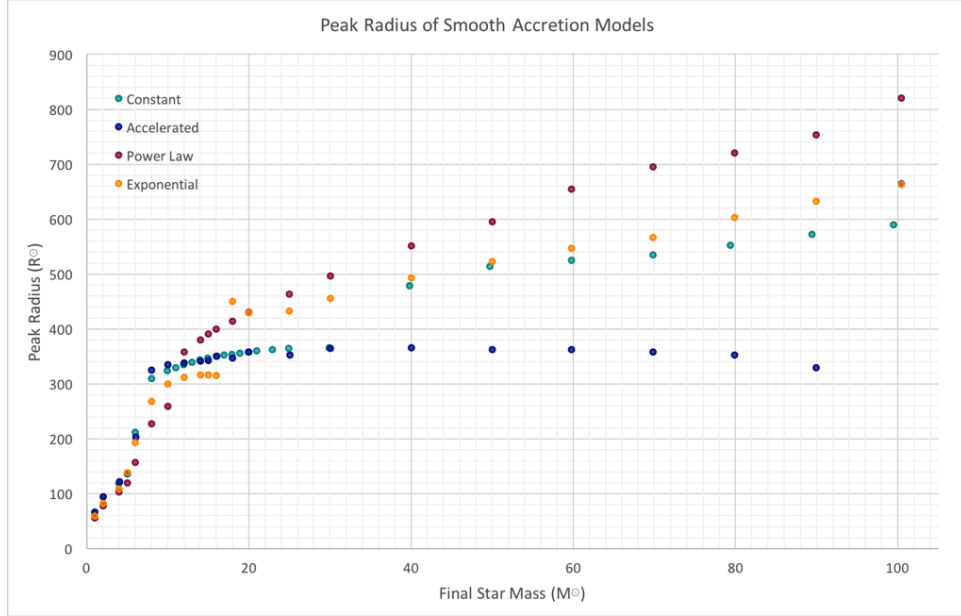


FIGURE 5.2: The maximum peak radius achieved for each of the smooth accretion models at each modelled mass. Note the accelerated model $100M_{\odot}$ result is obscured by the constant accretion data point.

Figure 5.2 shows the variation in peak radii achieved across the complete modelled range of masses. The models show similarity in peak radius at low masses, with distinction between the models becoming apparent once the swelling phase is fully established around the $8M_{\odot}$ mass point. The constant and exponential models share similar peak radii for masses $\geq 40M_{\odot}$, whereas the power law model is much greater and accelerated model is much less from the same point. The power law peak radii being much greater aligns with the idea that the stellar evolution has a time dependent factor, where energy and mass input to the protostellar core will have a large affect on the tracks of the star. Leading from this we can assume the power law reaches peak accretion around the time swelling occurs thus increasing the radius reached.

If an approach of observing the radii distributions for massive protostars as a function of their mass were possible, then each model would become apparent at certain boundaries. The power law model, for instance, would have a distribution shifted toward a greater radius-to-mass ratio compared to the others, and the accelerated model would be shifted lower.

An interesting point is the two large jumps in peak radius for all the models, but occurring at different masses. The first jump coincides with the

swelling phase, as expected, and can be seen by the difference in clusters between the $2M_{\odot}$ and $10M_{\odot}$ points. The second occurs at different points for each model; the constant model displays a jump between 30 and $40M_{\odot}$, the accelerated between 90 and $100M_{\odot}$. In the power law model it is harder to notice, but it occurs close after the establishment of a swelling phase, the 8 and $10M_{\odot}$ results are similar but the $12M_{\odot}$ result jumps from $\approx 250R_{\odot}$ to $360R_{\odot}$. The exponential jump occurs between the 16 and $18M_{\odot}$ with an increase of $130R_{\odot}$, noticing the small plateau between 10 and $15M_{\odot}$ points. Noting that these points occur relative to when the accretion models reach their peak rate, exponential and power law having peak rates early and the accelerated model at the end. However as the constant rate is always at its peak, there must be other factors involved. Thus, we suggest that the total internal energy and the high accretion rate input energy are the cause. These findings are similar to Hosokawa et al. (2010) showing stars of $\geq 30M_{\odot}$ can reach radii of $\approx 400R_{\odot}$.

5.4 Hertzsprung Russell Tracks

In Figures 4.9 to 4.20 and 4.38 to 4.45, we plot the bolometric luminosity against the star temperature to give an effective HR track. We must note that the star temperature would not be an observable quantity due to obscuration from the cloud. Aspects of these tracks conform with expectation, we see the maximum luminosity reached by each star increasing as a function of mass, also the temperature shows a general increase with time as to be expected with stellar evolution (Palla & Stahler, 1993). We note that the difference between solid line (star) and dashed line (accretion) luminosities show that the accretion luminosity is far more significant in the early stages of the evolution. The arrows on our temperature - luminosity figures display the accretion time at fixed intervals, with the tracks showing a tendency for the majority of track movement occurring early in the evolution, and a stagnation once accretion ends. We can attribute this quiet phase to the stellar interior evolution of before reaching main sequence. This remains relatively constant after accretion has stopped until main sequence is reached, this is a slow and long process which is not within the 10^6 yr time

frame of most of our models. However, the $100M_{\odot}$ star models (Figures 4.9, 4.12, 4.15 & 4.18) have an increase in luminosity from approximately $\log(L_{bol}/L_{\odot}) = 5.4$ to 6.3 over the final 9×10^5 years, which could be a signifying point of reaching main sequence.

Future use of similar tracks, finding the bolometric luminosity as function bolometric temperature rather than star temperature, may be more beneficial. We can observe bolometric temperature directly, whereas calculating the embedded star temperature will result in inaccuracies.

The theoretical HR tracks show the complexity of the time dependent relationship between luminosity and temperature for protostellar evolution. We observe general trends across all models; the tracks will all move upward to greater luminosities with increase in mass and time. The temperature tends to move toward higher temperatures with the amplitude of movement being mass dependent. This is comparable to the Henyey-Hayashi condition (Henyey et al., 1955) of establishing star type. We can see that the $1M_{\odot}$ results (Figures 4.11, 4.14, 4.17, 4.20, 4.39, 4.41, 4.43 & 4.45) show a decrease in luminosity at the end of the tracks, whereas the $100M_{\odot}$ (Figures 4.9, 4.12, 4.15 & 4.18) results show a move up by approximately half an order of magnitude. The $10M_{\odot}$ results show little movement in luminosity at the end of the track. The episodic burst models add fluctuations to luminosities and temperature throughout the track, with the final temperature and luminosity being almost identical to the smooth accretion tracks. The $10M_{\odot}$ power law bursts show a large time spent around $\log(T) = 3.6K$ before moving rapidly to higher temperatures. This is likely to be linked to how the bursts coincide with the swelling and contraction phases. The decreases in temperature toward the end of the tracks, in particular for the lower mass stars, occurs with the contraction phase where we know the clump is dissipated allowing for radiation to escape and thus reducing internal energy.

The HR diagrams offer insight to how a protostar behaves and is a useful addition to use alongside the other theoretical model outputs to check conformity to the. However, evaluating temperature for observed protostellar cores is hard due to the diffuse nature of the core itself and surrounding molecular clump. Another potential constraint on observation

is the radio continuum emission which is extremely bright for luminous objects. Temperature is easiest to observe once the surrounding cloud has dissipated.

5.5 Clump Luminosity Mass Relation

We must consider the limitations of the comparisons of the observational data in the clump luminosity as function of clump mass graphs made in this thesis. Our modelled data has not included the luminosity from the stars surrounding cloud. It is assumed that for the majority of the lifetime the stellar and accretion luminosity are much greater than the surrounding cloud. Early in the modelled evolution the luminosity of the cloud and the protostellar core may be of a similar order of magnitude, however the core will quickly increase its luminosity and the contribution of the clump to the total luminosity will be a negligible factor. The clump luminosity is found using the total kinetic energy of the clump assuming a turbulent velocity of 1 km s^{-1} (Heyer & Brunt, 2004) and the energy is released uniformly over the life of the evolution.

$$L_{\text{clump}} = \frac{\frac{1}{2} M_{\text{clump}} v_{\text{turb}}^2}{t_{\text{total}} 10^{-7}} \quad (5.1)$$

Where v_{turb} is the turbulent velocity, the mass of the clump is M_{clump} . The factor of 10^{-7} is the conversion from joules to ergs.

Tables 5.1 and 5.2 show data from smooth and burst models respectively. Both tables show that the median luminosity of each model exceeds the ambient clump luminosity by between four and six orders of magnitude. Thus, the data and figures created are exclusive of the clump luminosity due to the minor contribution throughout the long-term evolution.

Whilst ATLASGAL is one of the most comprehensive studies of the Milky Way, notably for masses above $10^4 M_{\odot}$, it still holds a level of selection bias due to the fixed bandwidth of a telescope and also due to where, and what, was observed. This is immediately obvious by the larger quantity of observed HII objects than the other two object types. This is explained by the nature of HII objects being brighter and therefore easier to observe. We normalise the data for each object type, so the distributions of each can

TABLE 5.1: Table of clump masses and calculated fixed luminosities from the associated smooth accretion star models.

Model Type	Final Star Mass (M_{\odot})	Clump Mass (M_{\odot})	Clump Luminosity (L_{\odot})	Median Luminosity (L_{\odot})
Accelerated	100.05	6559.61	5.40E-01	1.47E+06
	Constant	6512.89	5.36E-01	1.46E+06
	Exponential	6559.61	5.40E-01	1.47E+06
	Power Law	6559.61	5.40E-01	1.37E+06
Constant	25.09	917.35	7.56E-02	8.19E+04
	Exponential	909.49	7.49E-02	8.09E+04
	Power Law	914.73	7.53E-02	8.14E+04
	Power Law	914.73	7.53E-02	7.30E+04
Exponential	10.06	248.24	2.04E-02	5.74E+03
	Constant	246.47	2.03E-02	5.64E+03
	Power Law	248.24	2.04E-02	5.71E+03
	Power Law	248.24	2.04E-02	5.17E+03
Power Law	5.08	92.96	7.66E-03	5.48E+02
	Constant	91.64	7.55E-03	5.43E+02
	Exponential	91.64	7.55E-03	5.43E+02
	Power Law	91.64	7.55E-03	3.57E+02
Power Law	1.07	9.57	7.88E-04	3.91E+00
	Constant	9.64	7.94E-04	4.12E+00
	Exponential	9.37	7.72E-04	3.91E+00
	Power Law	9.37	7.72E-04	4.83E+00

be compared with greater confidence. Massive YSO's have been shown to have K-H timescales in the order of 0.5 to 4×10^5 years (Mottram et al., 2011) across the 10^4 to $10^5 L_{\odot}$ range, comparable to main sequence timescales and thus missing from the ATLASGAL survey meaning YSO object data may be bias toward lower luminosities. Whereas H_{II} have flat lifetimes of $\approx 3 \times 10^5$ years, across the same luminosity range. The naturally dimmer objects found in the infrared range are much harder to observe. A case where smaller protostars are greatly unaccounted for is plausible, in which the distributions of the YSO and MMB data could be far different. Further notes on the completeness of the ATLASGAL data are found in Urquhart et al. (2014), however the selection bias of the L/M ratio is undefined and would require further work to understand.

We used Urquhart's ATLASGAL data (Urquhart et al. (2014)) in the

TABLE 5.2: Table of clump masses and calculated fixed luminosities from the associated burst accretion star models.

Model Type	Final Star Mass (M_{\odot})	Clump Mass (M_{\odot})	Clump Luminosity (L_{\odot})	Median Luminosity (L_{\odot})
Constant	20.36	681.09	5.609E-02	5.17E+04
Exponential	20.36	681.09	5.609E-02	4.67E+04
Power Law	20.61	693.13	5.709E-02	4.36E+04
Accelerated	9.90	242.92	2.001E-02	5.40E+03
Constant	10.21	253.60	2.089E-02	5.97E+03
Exponential	10.21	253.60	2.089E-02	5.97E+03
Power Law	10.31	257.19	2.118E-02	5.64E+03
Accelerated	5.01	91.24	7.515E-03	5.30E+02
Constant	5.13	94.29	7.766E-03	5.74E+02
Exponential	5.13	94.29	7.766E-03	5.71E+02
Power Law	5.18	95.63	7.876E-03	4.67E+02
Accelerated	1.01	8.78	7.231E-04	3.37E+00
Constant	1.07	9.64	7.936E-04	3.99E+00
Exponential	1.07	9.57	7.881E-04	4.10E+00
Power Law	1.08	9.70	7.991E-04	5.11E+00

clump-luminosity-to-clump-mass tracks as comparison. As such we evaluate the observed data to find correlation between the two variables.

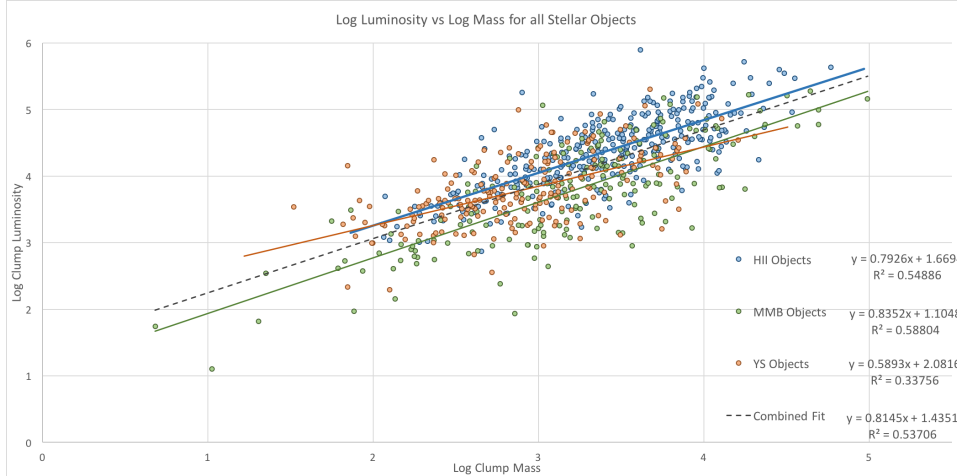


FIGURE 5.3: Urquhart et al. (2014) ATLASGAL observational data. Luminosity and mass are given in solar units.

We find linear least square regression for each data type and for the combined data set, shown in Figure 5.3. The YSO data shows the weakest correlation of the individual object types with an R squared value of 0.338.

We can attribute some of the variation from the line of best fit by the difficulty in observing the dimmer objects. The HII and MMB data shows a greater correlation both holding R squared values of ≈ 0.56 , meaning the line of best fit is a fairly good representation of the data. The R squared value for the combined data shows the YSO data has little effect on the regression as it is ≈ 0.55 , similar to the HII and MMB data. The YSO has a small effect due to the lower mass data being above the combined line of fit, and the higher mass being below, with the transition at almost exactly half way in the data seen at the Log Mass point of 3. In general, there is clear evidence of a positive linear correlation between the two variables, with an approximate ratio of $\approx 0.8L_{\odot} : 1M_{\odot}$. The other general observation is that HII data tends to be in the higher clump masses, the other two data sets are found distributed across the whole range.

We used Urquhart's ATLASGAL data (Urquhart et al., 2014) as reference in the clump mass - clump luminosity relation. To help understand how our model holds up in comparison, we evaluate the data in histogram form to see how well it compares to a normal distribution function. Dividing the clump luminosity by the clump mass to give the ratio for each data point and then taking the log of the ratio. The ratios are binned in 0.5 intervals from negative one, to positive 2. Figure 5.4 shows the difference in numbers

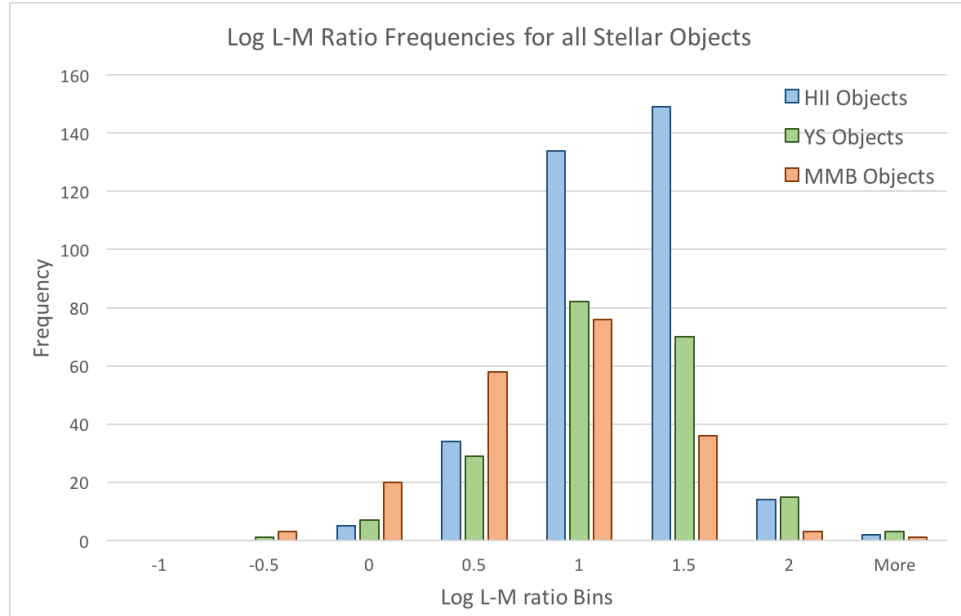


FIGURE 5.4: Frequency distribution of luminosity mass ratios from Urquhart et al. (2014) ATLASGAL data. L-M ratio is in solar units.

of each object type observed. As mentioned previously, the HII objects are naturally brighter and therefore easier to observe, thus why there is a 50% greater count compared to the YSOs and MMBs. This figure demonstrates the difficulty for a dedicated telescope in finding dimmer objects. As a result of this, the data cannot be truly evaluated as a distribution function until normalised. Figure 5.5 shows clearly that MMB data are more prev-

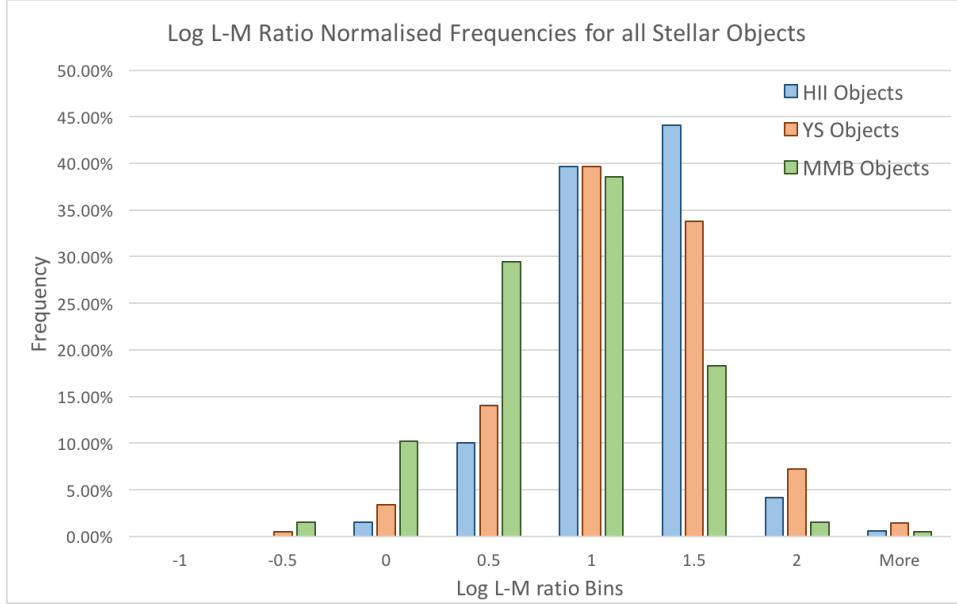


FIGURE 5.5: Normalised frequency distribution of L/M ratios from Urquhart et al. (2014) ATLASGAL data. Each object type was normalised against itself only.

elant at the lower luminosity to mass ratio with a larger decline in relative number from the 1 to 1.5 bin. The YSOs show a similar agreement to this except with a lesser decline in the 1.5 bin. The HII objects show an increase in count rather than decline in the 1.5 bin, as to be expected with hotter objects with greater luminosity for same equivalent mass. Figure 5.5 shows there is a level of normal distribution function to the number of objects across the range, we attempt to quantify this using a Kolmogorov-Smirnov single sample test on each object type. The single sample test compares the given data against a normal distribution curve with the result being a measure of similarity.

From Table 5.4 we can see that the standard deviation for each object type has a fair closeness to the mean, as we expect with a normal distribution. The HII data holds a smaller deviation which would correspond to the

TABLE 5.3: Part one of tabled ATLASGAL observation data and key values found and used with the Kolmogorov Smirnov test.

Object Type	Data Points	Mean Ratio	Median Ratio	Mean Squared
HII	338	0.9556	0.9958	0.9132
MMB	197	0.5926	0.6344	0.3512
YSO	207	0.9022	0.9176	0.8139

TABLE 5.4: Part two of tabled evaluated ATLASGAL data. The K-S test on this data is found with an α value of 0.05. A positive K-S score indicates that the difference between the data bins and a binned normal distribution function is less than the D_{crit} value, indicating a good fit.

Object Type	Variance	Std. Deviation	K-S Score
HII	0.1631	0.4038	0.0325
MMB	0.2583	0.5082	0.0801
YSO	0.2474	0.4974	0.0639

sharper peak observed in Figure 5.5. The tabulated data shows positive K-S scores for each object type which is found by subtracting the distribution function of the data away from the critical distribution function. A positive value is a good indication that the sampled frequency data follows a normal distribution curve.

From the distribution comparisons between model and ATLASGAL data, we can see the models obey similar normal distribution curves with the distribution being shifted dependent on mass. Generally, the lower mass models of $1 - 4M_{\odot}$ spend the majority of time in the lower L/M ratio bins of -1 and below. With increased mass the distributions move into greater luminosity mass ratios.

The low mass models can attribute the majority of luminosity to the accretion, whereas high mass attribute it to the stellar core. The model star of mass $100M_{\odot}$, spends the majority of time at $\text{LOG}(L/M) \geq 1.5$. An interesting feature to note is the $5M_{\odot}$, and some $6M_{\odot}$, models are bimodal distributions. The distributions show two distinct peaks in relative frequency an order of magnitude apart, from 0.5-1.5, with a large drop in between. This is likely to be due to these mid-range mass stars having similar timescales for the adiabatic accretion phase to the swelling and contraction phases.

The drop in luminosity between the peaks could be a result of the swollen cloud blocking the accretion and stellar luminosities. The stellar luminosity will increase, but still be contained within the swollen cloud and then over a short time the KH contraction will occur, causing the jump in L-M ratio rather than a steady progression between the two.

We applied a two sample Kolmogorov Smirnov test to compare the ATLASGAL distributions against each model distribution (Figures 4.25 to 4.29 and Figures 4.50 to 4.53). The data are tabulated in the appendix A.1 through A.6. The low and high mass KS tests show there is significant differences between the distributions meaning, the two cannot be reliably compared, indicated by a value of one in the respective field. We can clearly see this in the distribution figures, where the high and low mass curves are at extreme ends of the scale, whereas observational data distributions are centralised. From this, we see some of the mid range masses show that there is statistically no significant difference between the two distributions. The YSO data found good matches at final stellar mass $10M_{\odot}$ for all but the constant accretion models, and the MMB data had good matches at $6M_{\odot}$ for all but the power law model. The HII object data was found to have no matching model distribution, this however can be explained by our samples of higher masses being more sparse. More model data points are needed between $10M_{\odot}$ and $15M_{\odot}$ masses to find the statistical match of distribution curves. Whilst these data on their own may not be of significant use as the models are of individual stars and the observational data are for all masses, the result of finding matching masses to the overall distributions could hold potential for IMF analysis. Our results show that MMB data has an equivalent L-M distribution of a $6M_{\odot}$ mass star. As such, by counting the easily observable high mass stars within a cluster and finding the resultant L/M distribution, then the more obscured and embedded low mass stars can be effectively counted by using the model $6M_{\odot}$ distribution result as a weighting function to the observed high mass distribution. The same process can be applied for each individual, or a combination, of object types.

5.5.1 Smooth - Burst Comparison

There are some notable differences between the smooth clump L/M ratio results (Figures 4.25 to 4.28, and the burst data (Figures 4.50 to 4.53). All models, except the accelerated burst, show a bimodal distribution at the $5M_{\odot}$ and/or $6M_{\odot}$ masses (Sub Figures, C and D respectively in the range stated previously). All the bimodal burst models show a greater frequency in the peak corresponding to higher L/M ratio, than their smooth accretion equivalents. The episodic bursts will input a large amount of energy and drastically increase the luminosity. The larger second peaks can be attributed to the fact that there is a gradual decline in luminosity after the burst phase, thus there is an overall tendency for higher L/M ratios than the smooth accretion models.

At masses greater than $6M_{\odot}$ where the bimodal distributions disappear, the results for smooth and burst models become very similar with only minor variations in frequencies at the same L/M bins. As mentioned previously the bimodal nature is likely due to similar timescales for adiabatic and swelling phases. Thus we can make the assumption that the swelling and contraction timescales far exceed the adiabatic accretion timescale for when the bimodal features disappear. By the fact that the results between the burst and smooth model are so similar, we can state that the swollen star suppresses the rapid and large increases in luminosity. The method of doing so may be similar to the UV feedback mechanism shown in Hosokawa et al. (2016).

The $6M_{\odot}$ burst constant results show a much great second peak in the bimodal data than the smooth data (Figure 4.25, 4.50). This is the same for the $6M_{\odot}$ power law and exponential results. The smooth accelerated model only has a bimodal distribution for the $5M_{\odot}$ results, whilst the burst model does not have any bimodal distribution results.

5.5.2 Clusters, Multiplicity and SFE

The model used in this thesis tracks the evolution of a single star using a single star formation efficiency rate. The back end equations for; clump mass, it's dispersal rate and the star formation efficiency (Equation 4.1), are

taken from Molinari et al. (2008). The dispersal in clump mass can be seen in the L/M plots and is defined by equation six in Molinari et al. (2008). The clump mass is calculated as if it hosts a complete cluster of stars, with the modelled star being the dominant source of energy. More massive stars tend to have a shorter evolution timescales, thus we can assume that the other less massive stars in the cluster do not provide significant luminosity or temperature over the same period of time. A limitation of our method is that it assumes only a dominant single star, but up to thirty three percent of star systems are binary or greater multiplicity (Lada, 2006). Given our model tracks the dominant star, we can assume that if it were part of binary system then it is of equal or greater mass than the other star and thus it is at most a factor of two off (three for tertiary etc.). A potential solution would be to statistically evaluate the mass ratios of multiple star systems, then to use this ratio to model a parent star and its daughter. Combining the result will provide a better track of the bolometric luminosity of the clump. This does come with complications, such as the effect on clump dispersal rate and the overall evolution of stars when in close proximity.

Another consideration that was maintained as constant throughout this thesis was the SFE, $\approx 21\%$ as shown in Molinari et al. (2008). However, variations (Frank et al. (2014) has SFE at thirty percent) in the SFE will have an impact upon the general evolution in particular the outflow rate, protostellar temperature and luminosity. Modelling for different efficiencies is a potential avenue for further work, simply modifying the Molinari equations used in this paper to represent other SFEs.

5.5.3 IMF Adjusted Clump Luminosity

We take the frequencies of Clump L/M ratios and adjust them according to the initial mass function of Kroupa (2001). Firstly, we calculate the expected population using the final mass of the dominant star in the clump.

$$\zeta(m) = m^{-2.3} \quad (5.2)$$

Where m is star mass and $\zeta(m)$ is the population ratio at that mass. We find $\zeta(m)$ for the stellar masses 1, 2, 4, 5, 6, 8, 10, 15, 20, 25 and $100 M_{\odot}$, and then

multiply this factor by the clump L/M frequencies for the respective star. We then total the frequencies and normalise the result to between 0 and 1. To compare to the ATLASGAL data we multiply by a factor of ≈ 41 to get the same number of data points and normalise to be between 0 and 1.

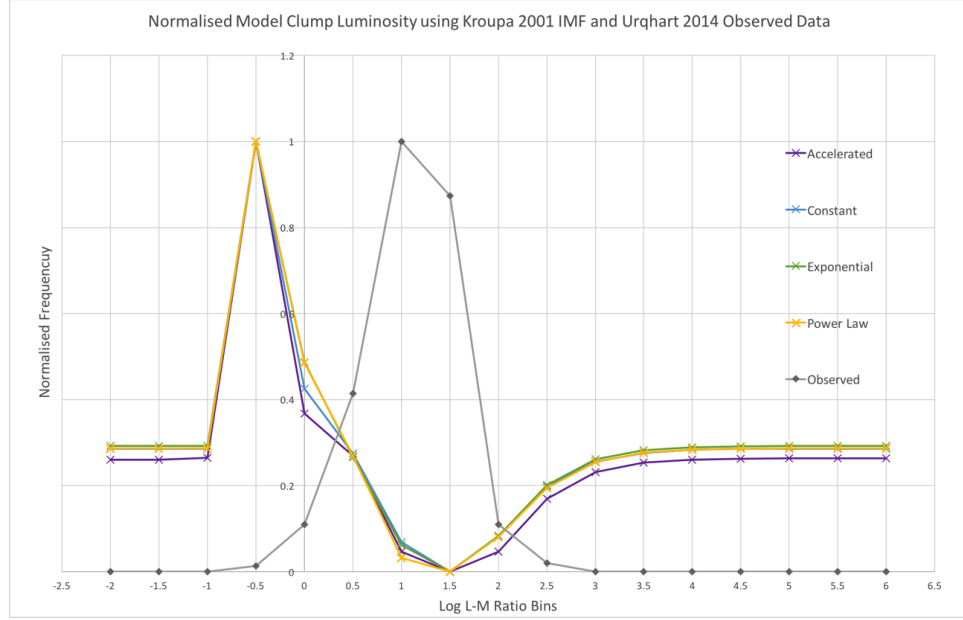


FIGURE 5.6: The four smooth accretion models binned clump luminosity - clump mass data has been adjusted using the initial mass function from Kroupa (2001). The grey solid line is the binned ATLASGAL data Urquhart et al. (2014). Both sets of data are normalised.

Figure 5.6 shows a clear distinction between the data sets where the ATLASGAL data tends towards higher L/M ratios. There are several factors that are not quantified in this data and thus result in the large discrepancy. Firstly, as mentioned previously, the ATLASGAL data is assumed complete for 10^4 clump masses and above, thus the data should be shifted toward higher L/M ratios. Secondly, the ATLASGAL data has no data points in the low (< -1.0) and high (> 2.0) L/M ratios. Therefore when normalising the data, the ATLASGAL data has multiple points where the frequency is zero, whereas the model data has only the minimum frequency as the zero point. Combining ATLASGAL with other surveys could help get a wider spread of data with fewer zero data points. Lastly, the model data only includes star masses down to $1M_{\odot}$, whereas a complete IMF holds a large proportion of stars in a cluster at $< 1M_{\odot}$. This last factor may have minimal

effect as per the first point. This is an imperfect method of analysis however, it makes new steps toward comparisons between observational and model data. As mentioned previously, the IMF holds a fundamental role in the formation of stars and further work to use the modelled results with an IMF to match to real data will be critical in producing a complete evolution of molecular clouds and star formation.

5.6 Episodic Bursts

In Table 4.4, it is shown that the STELLAR code would not work for masses greater than $15M_{\odot}$ for the accelerated accretion model, and $25M_{\odot}$ for the other models. The burst models in their 'high' accretion phases reach rates 9.099 times greater (Equation. 3.11) than the 'smooth' model equivalents. We did not pursue the issue further as we had obtained results for all the low and intermediate mass stars and most of the high masses. However, the failure is likely to be due to the extreme quantities of mass moving and the Henyey method not finding convergence.

The burst accretion method has shown the protostellar peak radii achieved are much larger than the smooth accretion equivalents. Again showing evidence for the swelling phases occurring due to energy input rate and less so on the current mass. Another note to this is that if observational evidence does not conform to the peak radii achieved then it is likely the 90% – 10% ratio of mass accumulated in the high and low accretion states is incorrect. Further testing with our accretion model with different ratios could lead to a relationship between this ratio and the maximum radius and luminosity achieved.

As shown in Figure 5.7, it is unlikely to be that episodic accretion that is perfectly modulated as used in our model is what occurs in reality. It is more likely to be that the bursts peak but then followed shortly by a power law decrease in rate as radiation feedback would begin to slow it. An interesting extension to this model would be to establish a multiplicative factor to the accretion rate that combines a series of sinusoidal functions to provide a nearly random accretion rate. In its simplest form an initial main sinusoidal function would establish the change between high and low

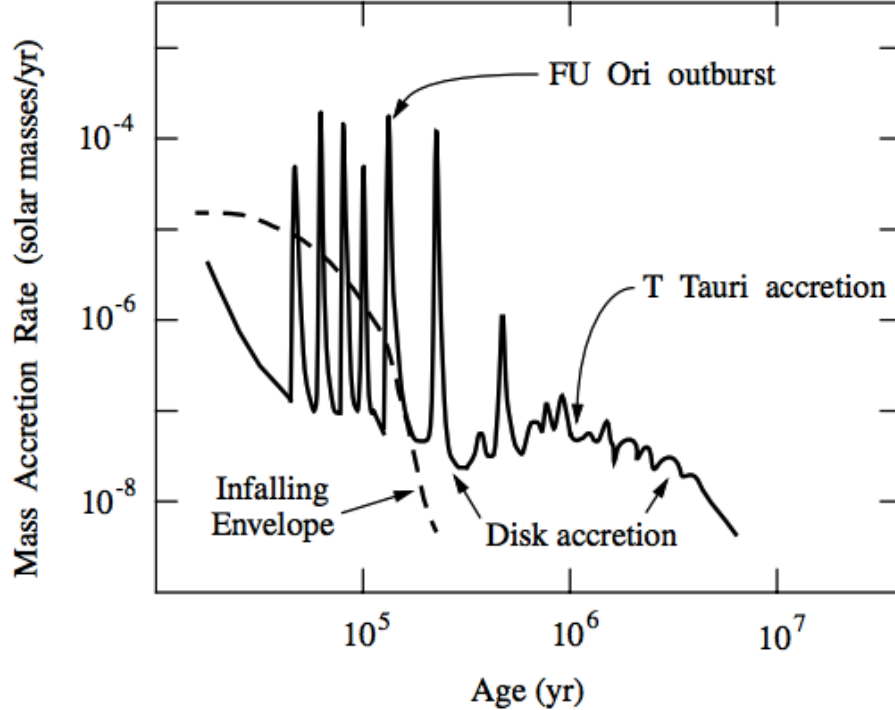


FIGURE 5.7: This figure is taken from Calvet et al. (2000). The accretion versus time graph displays potential ideas on the evolution of disk accretion and the different phases that occur. Early infall burst accretion, moving to a more irregular ‘noisy’ disk accretion.

accretion states, with further sine functions providing a ‘noise’ factor to the accretion as would be expected in reality. This would also require a more diverse final mass calculation.

In concurrence we modelled short accretion burst followed by a relatively long quiescent phase (Smith et al. (2012)). Recent findings however, have shown that the time frame of these bursts can vary from a few decades (Audard et al. (2014)) to several hundred years (Vorobyov et al. (2013)). Modelling both short cycle and long cycle bursts would be beneficial.

5.7 Early Accretion Cut Off

Previously we posed the question of accretion cut off during swelling or contraction phases and its effect. Seen in the mass radius tracks for $6-10M_{\odot}$ masses, the accretion cuts off during these stages as seen by the sharp decline in radius. Looking at the episodic $8M_{\odot}$ mass radius tracks, the change to low accretion phase causes a very similar drop in radius from the peak.

The accretion cut off has little effect on the end result, in which the primary factor of final radius and luminosity, is the mass. This may change with a hot accretion method where internal energy would be greater. The $100M_{\odot}$ mass radius tracks show a more gradual decline in radius, with eventual growth again as the mass is still increasing. How much influence of this effect is due to the continued accretion, or just a consequence of being a massive star, is hard to determine.

5.8 Molecular cloud influence

Here we define an accretion scenario within cylindrical filaments as a primary property of GMCs with star formation occurring within these filaments. Figure 5.8 shows a simplified view of the growth of a protostellar

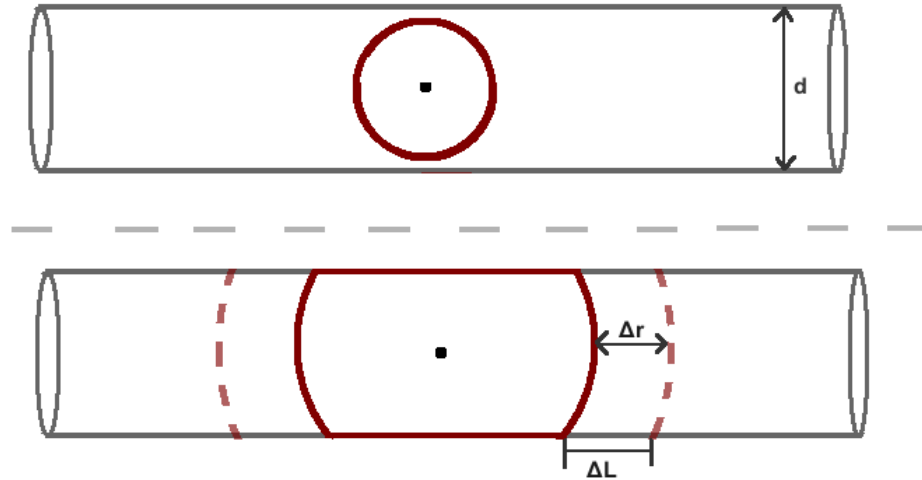


FIGURE 5.8: An ideal scenario depicting the growth of a sphere of influence by a protostellar core in a cylindrical filament. The black dot serves as a central point for a protostar. The red lines represent the sphere of influence, with dashed line as sphere at a future time. d is the diameter of cylinder, Δr is the change in radius, ΔL is the change in length.

clouds sphere of influence. Initially, in the upper figure section, the growth of the sphere is unaffected by cloud shape and so the mass encapsulated by the SOI grows proportionally to the volume of the sphere. Once the SOI diameter exceeds the diameter of the filament, the mass encapsulated will no longer be proportional to sphere volume but to the volume of a cylinder, as shown in the lower section of the figure. Protostellar SOIs would have

a very large radius of curvature, so the curve of the SOI could be approximated as a flat disc growing along the length of the cylinder. The result being mass encapsulated grows proportional to $\pi(\frac{d}{2})^2$ when $r > (\frac{d}{2})$, and the SOI grows at a rate proportional to the speed of sound in the molecular cloud. Including the collapse across the width of the filament would result in a time dependent differential equation that requires further analysis. The scale of this gas envelope is much greater than the size of an accretion disk which would be around the central protostellar core. We know that the envelope mass slowly feeds onto the accretion disk, which in turn feeds the protostellar core, Kenyon & Hartmann (1995). There are questions that remain. How does the envelope feeding the accretion disk affect the accretion rate onto the core from the disk? What orientation does the accretion disk take, relative to the filament? Can this be incorporated into the model we used?

5.9 Other comparative works

Hosokawa et al. (2016) has shown relatively slow accretion of $< 50M_{\odot}$ stars in the primordial era, where stars stop accreting at the Kelvin-Helmholtz contraction phase due to UV feedback. This does not seem to be the case for our findings, as the high mass star models continue to contract and even continue accretion after the KH phase. However we do notice massive increases in radius for the episodic burst accretion, and we question if this is indicative of accretion slowing as energy cannot be radiated away quick enough. If our code is correct, then the slowing of $< 100M_{\odot}$ primordial stars shows the importance of establishing the correct chemical composition of protostars, as the differences are significant. Thus when trying to model protostellar evolution as an aid in observation, the stars local molecular cloud composition must be evaluated.

Episodic bursts have been shown to contribute to a significant drop in the UV feedback corresponding to when a burst has occurred (Hosokawa et al., 2016) but there is an increase in bipolar outflow rate. Thus, it is suggested to research the UV feedback mechanism in this model.

Our findings have shown a clear distinction between two types of protostellar evolution; the lower masses where swelling does not occur, and higher masses where swelling does occur. We have also shown that the mass range at which this swelling occurs is not dependent on mass but upon multiple factors, notably energy input in the form of accretion rate and, at what stage the majority of mass is accumulated. This becomes problematic with comparing to observational data of protostars where the swelling radii overlap if compared at different ages. Multiple examples can be seen in the figures produced, notably Figures 4.1 and 4.2 the $100M_{\odot}$ stars have a peak radius greater than the $50M_{\odot}$ stars, but both occur around the same $10M_{\odot}$ mass point.

Another limitation of this research has been the fixed scale of accretion time, observation has shown that massive stars could accrete in much less than the 10^5 yr scale we defined, and the smaller masses over much longer scales (Mottram et al., 2011). If the accretion time is mass dependent, then this could further alter the protostellar masses where swelling occurs.

Our model runs using the cold accretion mechanism, being the slow infall from the disk where energy is lost through radiative feedback. Further work using our model but implementing a hot accretion method would help establish differences and provide evidence for, and against, each concept.

Chapter 6

Conclusion

Our research has shown the validity and value of computational modelling. The results build upon previous stellar evolutionary codes by showing more detailed paths taken in each type of evolutionary track studied, achieved through smaller time steps and convergence modelling of a complete stellar structure.

The research has made initial steps toward finding valid methods of comparing theoretical and observational data and to try make conclusions from them. In doing so we show the importance of simulations and the extent of how much useful data can be extracted and analysed to provide useful information.

The updates made to the code will reduce the total time requirement when running the program in future. The updates also provide a good groundwork for running similar accretion methods, or building upon them, as the equations have already been successfully incorporated into the main code. The smooth accretion models serve as a good baseline for understanding stellar evolution. Using the smooth model as a baseline result, the effect the burst models have can be observed clearly.

6.1 Summary of Findings

Our models clearly demonstrate the similarities in the evolutionary tracks taken between accretion models, in particular in the early stages of stellar growth. This similarity potentially holds key information as to why all the accretion models in this research have observational support. The accelerated model shows the greatest differences to the others for early stages of

evolution, or at mid to high masses, and therefore holds a greater potential to be identified in observation.

We must note the second surge in peak radii achieved by each model as shown in Figure 5.2. The cause is indeterminate but clearly occurs at different mass points for each accretion model and as such holds potential as a signatory feature.

The episodic burst tests have shown a blurring effect in the mass radius evolutionary track. The switching between high and low accretion rates causes large fluctuations in the radius of the protostar, an observed star with the same accretion properties could appear to be a large star in a low accretion phase or a small star in high accretion phase. The use of $L_{clump} - M_{clump}$ distributions were better for comparing to observation (Figures 4.25-4.28 and 4.50-4.53). The results produced good distributions, closely matching the observed equivalents. The episodic bursts compared to the smooth accretion distributions show the lower luminosity mass ratios are shifted up, but the overall distribution is still very similar for models of the same final mass. As such mapping clump luminosity as a function of clump mass has shown to be a powerful, relevant tool and is suggested for use in others research of a similar nature.

We add minor additions to literature versions of the luminosity - temperature tracks, with the addition of episodic bursts showing again a blurring effect between the high or low state. We notice that early in the evolution, the bursts only have a minor effect on the temperature, indicating the protostar temperature is more dependent upon the long term evolution, and not the short term accretion changes.

6.2 Future work

The work completed in this project has shown how diverse the STELLAR code can be. With many variables unchanged, a lot is left to explore. We

know that the composition of GMCs vary, especially when comparing modern and early universe examples. The fractions of hydrogen, helium and heavier elements could easily be adjusted to observe changes in tracks.

This project exclusively worked using a cold accretion model, whereby the material in accretion disk accrued onto protostellar core via steady infall. The code contains an energy parameter which can be adjusted to easily switch to a hot accretion model. Both methods are still debated upon and the insight given by this code could be beneficial.

Further inclusion of other observational data of clump luminosities and masses appended to the distributions and tracks we produced would be beneficial. A focus on finding, and including, low mass objects would be beneficial as the ATLASGAL data used in this project lacks information in this region. As mentioned before, with more observational data and improving upon our models, it could prove useful for IMF research.

To produce a more realistic model, we should look to model a secondary function that simulates accretion disk growth from infalling envelope mass. Currently the model is an enclosed system where total mass remains constant, modelling the steady input of more mass into the system to simulate envelope accretion could produce interesting results that better align with other works.

As previously mentioned, the episodic bursts we simulated were an ideal scenario between two clearly defined states. A more realistic model using shorter and/or variable time scales between states would be a good step to make. Developing the code to include a secondary function, which works with the bursts code but add small fluctuations to the total accretion rate would also be a good addition to the base code used in this research..

6.3 End

The research conducted in this project has shown the worth of hydrodynamic modelling and how, with effective data analysis methods, results can be used alongside or compared to real observational data. The evolutionary tracks we produced show evidence for complexities that are not found in literature due to the instantaneous nature of observations.

Hopefully the data presented here will prove useful for other works and fields of research, which will ultimately help in understanding our local cluster, galaxy, Solar system and our place in the universe.

Appendix A

Appendix

Included in the appendix is all the individual Kolmogorov Smirnov test results. The significant difference row is a choice result, a value of one shows there is a significant difference between distributions and a value of zero shows there is no significant difference in distributions. If the D-crit value is greater than D-stat value then a zero is given when the p-value is greater than 0.05. A value of one is given if D-crit is less than D-stat or the p-value is less than 0.05.

Accretion Method	Statistic	Final Mass (M_{\odot})			
		4	5	6	8
Accelerated	D-stat	0.800345968	0.795782064	0.543682064	0.239448731
	p-value	0.005280863	0.00502412	3.76724E-05	2.37261E-10
	D-crit	0.096198483	0.096198472	0.096198472	0.096198472
	Significant Difference	1	1	1	1
Constant	D-stat	0.815415398	0.806348731	0.551948731	0.234948731
	p-value	0.006190602	0.00563175	4.93296E-05	5.55643E-10
	D-crit	0.096198472	0.096198472	0.096198472	0.096198472
	Significant Difference	1	1	1	1
Exponential	D-stat	0.835848731	0.829548731	0.565648731	0.263515398
	p-value	0.007580818	0.007132576	7.51861E-05	1.90425E-12
	D-crit	0.096198472	0.096198472	0.096198472	0.096198472
	Significant Difference	1	1	1	1
Power Law	D-stat	0.821548731	0.819382064	0.588048731	0.334815398
	p-value	0.006588672	0.006446186	0.000140854	1.42077E-11
	D-crit	0.096198472	0.096198472	0.096198472	0.096198472
	Significant Difference	1	1	1	1

TABLE A.1: Two Sample KS test results of MMB data. Tested using ATLASGAL MMB object data against final mass stars of 1, 2, 4, 5, 6 and 8 M_{\odot} .

Accretion Method	Statistic	Final Mass (M_{\odot})					
		10	15	20	25	100	
Accelerated	D-stat	0.320734179	0.713287648	0.713287648	0.719320981	0.896028765	
	p-value	1.66345E-12	0.001733691	0.001733691	0.001896734	0.012777905	
	D-crit	0.096198472	0.096198472	0.096198472	0.096198472	0.096198472	
	Significant Difference	1	1	1	1	1	
Constant	D-stat	0.326834179	0.716287648	0.729720981	0.738254315	0.906928765	
	p-value	4.35973E-12	0.001813426	0.002203525	0.002480726	0.013900515	
	D-crit	0.096198472	0.096198472	0.096198472	0.096198472	0.096198472	
	Significant Difference	1	1	1	1	1	
Exponential	D-stat	0.302167513	0.6551187648	0.733887648	0.743854315	0.895528765	
	p-value	6.15064E-14	0.000643173	0.002335935	0.002675653	0.012727757	
	D-crit	0.096198472	0.096198472	0.096198472	0.096198472	0.096198472	
	Significant Difference	1	1	1	1	1	
Power Law	D-stat	0.277400846	0.510420981	0.647587648	0.709320981	0.863728765	
	p-value	9.57012E-14	1.11404E-05	0.000554063	0.00163224	0.009779861	
	D-crit	0.096198472	0.096198472	0.096198472	0.096198472	0.096198472	
	Significant Difference	1	1	1	1	1	

TABLE A.2: Two Sample KS test results of MMB data. Tested using ATLASGAL MMB object data against final mass stars of 10, 15, 20, 25 and 100 M_{\odot} .

Accretion Method	Statistic	Final Mass (M_{\odot})			
		4	5	6	8
Accelerated	D-stat	0.878449894	0.87388599	0.662556039	0.354922705
	p-value	0.013191705	0.012718279	0.000993046	5.39672E-10
	D-crit	0.093883519	0.093883508	0.093883508	6.66411E-12
	Significant Difference	1	1	1	0.093883508
Constant	D-stat	0.893519324	0.884452657	0.663956039	0.348422705
	p-value	0.014828425	0.013830161	0.001018066	2.52102E-10
	D-crit	0.093883508	0.093883508	0.093883508	6.43419E-12
	Significant Difference	1	1	1	0.093883508
Exponential	D-stat	0.913952657	0.907652657	0.655389372	0.348622705
	p-value	0.017227808	0.016465967	0.000872162	2.58241E-10
	D-crit	0.093883508	0.093883508	0.093883508	7.77356E-12
	Significant Difference	1	1	1	0.093883508
Power Law	D-stat	0.899652657	0.89748599	0.672322705	0.415822705
	p-value	0.015526881	0.01527801	0.001177614	1.29255E-07
	D-crit	0.093883508	0.093883508	0.093883508	5.87475E-12
	Significant Difference	1	1	1	0.093883508

TABLE A.3: Two Sample KS test results of YSO data. Tested using ATLASGAL YSO object data against final mass stars of 1, 2, 4, 5, 6 and 8 M_{\odot} .

Accretion Method	Statistic	Final Mass (M_{\odot})				100
		10	15	20	25	
Accelerated	D-stat	0.088310628	0.49121256	0.49121256	0.497245894	0.829376812
	p-value	0.076471887	8.32517E-06	8.32517E-06	1.07374E-05	0.008639057
	D-crit	0.093883508	0.093883508	0.093883508	0.093883508	0.093883508
	Significant Difference	0	1	1	1	1
Constant	D-stat	0.094410628	0.49421256	0.507645894	0.516179227	0.840276812
	p-value	0.047965664	9.45892E-06	1.63045E-05	2.25492E-05	0.009548583
	D-crit	0.093883508	0.093883508	0.093883508	0.093883508	0.093883508
	Significant Difference	1	1	1	1	1
Exponential	D-stat	0.069743961	0.43311256	0.51181256	0.521779227	0.828876812
	p-value	0.260580134	4.07984E-07	1.91398E-05	2.76606E-05	0.008598707
	D-crit	0.093883508	0.093883508	0.093883508	0.093883508	0.093883508
	Significant Difference	0	1	1	1	1
Power Law	D-stat	0.059843478	0.288345894	0.42551256	0.487245894	0.797076812
	p-value	0.441811708	1.75415E-14	2.50438E-07	7.00671E-06	0.006274616
	D-crit	0.093883508	0.093883508	0.093883508	0.093883508	0.093883508
	Significant Difference	0	1	1	1	1

TABLE A.4: Two Sample KS test results of YSO data. Tested using ATLASGAL YSO object data against final mass stars of 10, 15, 20, 25 and 100 M_{\odot} .

Accretion Method	Statistic	Final Mass (M_{\odot})					
		4	5	6	7	8	
Accelerated	D-stat	0.902304337	0.897740434	0.725915385	0.418282051	0.314332347	0.17426568
	p-value	0.05819239	0.056922644	0.018451046	3.98825E-05	3.94953E-08	2.30524E-09
	D-crit	0.073777274	0.07377726	0.07377726	0.07377726	0.07377726	0.07377726
	Significant Difference	1	1	1	1	1	1
Constant	D-stat	0.917373767	0.908307101	0.727315385	0.411782051	0.314499014	0.180132347
	p-value	0.062456834	0.059878135	0.018678632	2.99452E-05	4.01654E-08	5.63336E-10
	D-crit	0.07377726	0.07377726	0.07377726	0.07377726	0.07377726	0.07377726
	Significant Difference	1	1	1	1	1	1
Exponential	D-stat	0.937807101	0.931507101	0.718748718	0.411982051	0.313599014	0.177199014
	p-value	0.068404551	0.066551373	0.017310478	3.02165E-05	3.66652E-08	1.14624E-09
	D-crit	0.07377726	0.07377726	0.07377726	0.07377726	0.07377726	0.07377726
	Significant Difference	1	1	1	1	1	1
Power Law	D-stat	0.923507101	0.921340434	0.735682051	0.479182051	0.313599014	0.188932347
	p-value	0.064222781	0.063596996	0.020071129	0.00034315	3.66652E-08	6.23532E-11
	D-crit	0.07377726	0.07377726	0.07377726	0.07377726	0.07377726	0.07377726
	Significant Difference	1	1	1	1	1	1

TABLE A.5: Two Sample KS test results of HII data. Tested using ATLASGAL HII object data against final mass stars of 1, 2, 4, 5, 6 and $8 M_{\odot}$.

Accretion Method	Statistic	Final Mass (M_{\odot})					
		10	15	20	25	100	
Accelerated	D-stat	0.102829389	0.428167653	0.428167653	0.527796055	0.868996055	
	p-value	0.001544678	0.000060182	0.000060182	0.001163824	0.049173924	
	D-crit	0.07377726	0.07377726	0.07377726	0.07377726	0.07377726	
	Significant Difference	1	1	1	1	1	
Constant	D-stat	0.101862722	0.431167653	0.444600986	0.523896055	0.879896055	
	p-value	0.001766348	6.78134E-05	0.000112455	0.001067946	0.052060187	
	D-crit	0.07377726	0.07377726	0.07377726	0.07377726	0.07377726	
	Significant Difference	1	1	1	1	1	
Exponential	D-stat	0.102162722	0.428167653	0.448767653	0.428167653	0.868496055	
	p-value	0.001694577	0.000060182	0.00013038	0.000060182	0.049043112	
	D-crit	0.07377726	0.07377726	0.07377726	0.07377726	0.07377726	
	Significant Difference	1	1	1	1	1	
Power Law	D-stat	0.099462722	0.236862722	0.362796055	0.470362722	0.836696055	
	p-value	0.0024507	2.15161E-13	2.0691E-06	0.000264103	0.041025033	
	D-crit	0.07377726	0.07377726	0.07377726	0.07377726	0.07377726	
	Significant Difference	1	1	1	1	1	

TABLE A.6: Two Sample KS test results of HII data. Tested using ATLASGAL HII object data against final mass stars of 10, 15, 20, 25 and $100 M_{\odot}$.

Bibliography

- Aston, F. W. 1920, Nature, 105, 617
- Audard, M., Ábrahám, P., Dunham, M. M., et al. 2014, arXiv:1401.3368
- Bodenheimer, P., Laughlin, G. P., Rozyczka, M., et al. 2006, Numerical Methods in Astrophysics: An Introduction (Series in Astronomy and Astrophysics) (CRC Press)
- Calvet, N., Hartmann, L., & Strom, S. E. 1999, Evolution of Disk Accretion, arXiv:astro-ph/9902335
- Calvet, N., Hartmann, L., & Strom, S. E. 2000, Protostars and Planets IV, 377
- Carroll, B. W., & Ostlie, D. A. 2006, An Introduction to Modern Astrophysics (2nd Edition) (Pearson)
- Carroll B.W., O. D. 1996, An introduction to modern astrophysics, 1st edn.
- Chandrasekhar, S. 1931, ApJ, 74, 81
- Davies, B., Hoare, M. G., Lumsden, S. L., et al. 2011, Monthly Notices of the Royal Astronomical Society, 416, 972
- Eddington, A. S. 1920, The Observatory, 43, 341
- Frank, A., Ray, T. P., Cabrit, S., et al. 2014, in Protostars and Planets VI (University of Arizona Press)
- Girichidis, P., Federrath, C., Banerjee, R., & Klessen, R. S. 2011, Monthly Notices of the Royal Astronomical Society, 420, 613
- Hansen, C. J., Kawaler, S. D., & Trimble, V. 2004, Stellar Interiors (Springer New York), doi:10.1007/978-1-4419-9110-2
- Hartmann, L., & Kenyon, S. J. 1996, Annual Review of Astronomy and Astrophysics, 34, 207

- Helmholtz, H. 1856, Philosophical Magazine Series 4, 11, 489
- Henyey, L. G., Lelevier, R., & Levée, R. D. 1955, Publications of the Astronomical Society of the Pacific, 67, 154
- Heyer, M. H., & Brunt, C. M. 2004, ApJ Letters, 615, L45
- Hosokawa, T., Hirano, S., Kuiper, R., et al. 2016, ApJ, 824, 119
- Hosokawa, T., Yorke, H. W., & Omukai, K. 2010, The Astrophysical Journal, 721, 478
- Jean-Luc Beuzit, et al. Grenoble Observatory, European Southern Observatory. 2016
- Jeans, J. H. 1902, Philosophical Transactions of the Royal Society A: Mathematical, Physical and Engineering Sciences, 199, 1
- Kenyon, S. J., & Hartmann, L. 1995, The Astrophysical Journal Supplement Series, 101, 117
- Klassen, M., Pudritz, R. E., Kuiper, R., Peters, T., & Banerjee, R. 2016, The Astrophysical Journal, 823, 28
- Kroupa, P. 2001, Monthly Notices of the Royal Astronomical Society, 322, 231
- Krumholz, M. R. 2014, 43
- Krumholz, M. R., Klein, R. I., McKee, C. F., Offner, S. S. R., & Cunningham, A. J. 2009, Science, 323, 754
- Krumholz, M. R., Matzner, C. D., & McKee, C. F. 2006, The Astrophysical Journal, 653, 361
- Kuiper, R., Klahr, H., Beuther, H., & Henning, T. 2011, ApJ, 732, 20
- Kuiper, R., & Yorke, H. W. 2013, ApJ, 772, 61
- Lada, C. J. 2006, The Astrophysical Journal, 640, L63
- Lane, H. J. 1870, American Journal of Science, s2-50, 57
- McKee, C. F., & Tan, J. C. 2003, ApJ, 585, 850

- Molinari, S., Pezzuto, S., Cesaroni, R., et al. 2008, *Astronomy and Astrophysics*, 481, 345
- Mottram, J. C., Hoare, M. G., Davies, B., et al. 2011, *The Astrophysical Journal*, 730, L33
- Myers, P. C., Adams, F. C., Chen, H., & Schaff, E. 1998, *The Astrophysical Journal*, 492, 703
- NASA, ESA, J. Hester and A. Loll (Arizona State University). 2016, *Hubble Mosaic of the Crab Nebula*, <http://hubblesite.org/newscenter/archive/releases/2005/37/image/a/>, online; accessed 7 September 2016
- NASA/CXC/SAO/F.Seward et al. 2016, *Crab Nebula: Fingers, Loops and Bays in The Crab Nebula*, <http://chandra.harvard.edu/photo/2008/crab/>, online; accessed 7 September 2016
- NASA/DOE/Fermi LAT/R. Buehler. 2016, *NASA's Fermi Spots 'Super-flares' in the Crab Nebula*, <http://chandra.harvard.edu/photo/2008/crab/>, online; accessed 7 September 2016
- NASA/JPL-Caltech/R. Gehrz (University of Minnesota). 2016, *Crab Nebula*, http://www.nasa.gov/multimedia/imagegallery/image_feature_567.html, online; accessed 7 September 2016
- NASA/Swift/E. Hoversten, PSU. 2016, *An Image Gallery Gift from NASA's Swift*, http://www.nasa.gov/mission_pages/swift/bursts/swift-images.html, [Online; accessed 7 September 2016]
- NRAO. 2016a, *Crab Nebula M1*, <http://images.nrao.edu/34>, online; accessed 7 September 2016
- . 2016b, *Radio Image of Crab Nebula*, online; <http://images.nrao.edu/393>, accessed 7 September 2016
- Offner, S. S. R., & McKee, C. F. 2011, *ApJ*, 736, 53
- Palla, F., & Stahler, S. W. 1993, *The Astrophysical Journal*, 418, 414
- Schwartzchild, M. 1962, *Structure and Evolution of Stars* (Dover Publications)

- Shu, F., Najita, J., Ostriker, E., et al. 1994, *ApJ*, 429, 781
- Shu, F. H. 1977, *ApJ*, 214, 488
- Smith, M., Mac Low, M.-M., & Heitsch, F. 2000, *Astronomy and Astrophysics*, 362, 333, cited By 19
- Smith, M. D. 2014, *Monthly Notices of the Royal Astronomical Society*, 438, 1051
- Smith, R. J., Hosokawa, T., Omukai, K., Glover, S. C. O., & Klessen, R. S. 2012, *Monthly Notices of the Royal Astronomical Society*, 424, 457
- Stamatellos, D., Hubber, D., & Whitworth, A. 2011, Episodic accretion, radiative feedback, and their role in low-mass star formation, arXiv:1109.2100
- Sun.org. 2016, Heat Transfer of Stars, http://www.sun.org/uploads/images/Heat_Transfer_in_Stars.png, online; accessed 7 September 2016
- Urquhart, J. S., Csengeri, T., Wyrowski, F., et al. 2014, *Astronomy & Astrophysics*, 568, A41
- Vorobyov, E. I., Baraffe, I., Harries, T., & Chabrier, G. 2013, *Astronomy & Astrophysics*, 557, A35